CHARLES UNIVERSITY
Faculty of Science

Study programme: Chemistry
Study branch: Physical chemistry

Roman Staňo

Effect of acid-base equilibria on the association behaviour of polyelectrolytes

Vliv acidobazických rovnováh na asociační chování polyelektrolytovů

Type of thesis
DIPLOMA THESIS

Supervisor: RNDr. Peter Košovan, Ph.D.

Prague, 2020

I declare that I carried out this master thesis independently, and only with the cited sources, literature and other professional sources.

I understand that my work relates to the rights and obligations under the Act No. 121/2000 Sb., the Copyright Act, as amended, in particular the fact that the Charles University has the right to conclude a license agreement on the use of this work as a school work pursuant to Section 60 subsection 1 of the Copyright Act.

In ..... date ..... signature of the author

In the first place, I would like to thank my supervisor Peter Košovan for allowing me to work under his mentorship during my master's and bachelor's studies. His guidance helped me to develop many qualities important for a scientist. I also express my gratitiude to other members of the Soft Matter Research Group at Charles University, especially Lucie Nová, Filip Uhlík and Pascal Hebbeker for their perspectives, helpful discussions and useful tips. Next, I appreciate Andrea Tagliabue from University in Como, who contributed a lot to Section 4.4 by providing me with some of his tools for analysis. Finally, I wish to thank Christian Holm, who enabled me to spent two months in his group at Institute for Computational Physics at University of Stuttgart as a visiting student.

Title: Effect of acid-base equilibria on the association behaviour of polyelectrolytes

Author: Roman Staňo

Department: Department of physical and macromolecular chemistry

Supervisor: RNDr. Peter Košovan, Ph.D., Department of physical and macromolecular chemistry

Abstract: Macromolecules bearing charged monomeric units are omnipresent in the nature. Living systems utilize complex mechanisms to regulate the charge on biomacromolecules, hence controlling their structure or activity. Recently, there has been a surge in the preparation of bioinspired macromolecular materials, such as drug delivery systems or self-healing hydrogels, possessing a high degree of responsivity to the external stimuli, such as pH. However, the fundamental understanding of pH-based charge regulation in both natural and synthetic systems seems to be lacking, presumably because of the deficiency of suitable theoretical models and computational methods. Herein, we used coarse-grained simulations to shed light on the underyling physical principles of the relation between the pH, ionization, multivalency and structure of macromolecules. We presented a novel model of complex coacervates, and used it to describe phase equilibria and ion partitioning in such systems. Next, we explored the effects of multivalent ions and charged oligomers on the ionization of linear and branched macromolecules. We compared potentials of mean force between ions of various valencies to demonstrate the presence of strong charge-charge correlation between charged macromolecules, and multivalent ions or oligomers. Finally, we described a charge-driven assembly of oppositelly charged macromolecules, and showed how pH can be used to control the formation of electrostatically cross-linked reversible gels. The above collection of case studies shows that in spite of differences between the studies systems, phase equilibria and acid-base equilibria in macromolecular systems can be described by a small number of universal principles.

Keywords: Computer simulation, reaction ensemble, polyelectrolyte, interpolyelectrolyte complex, ionization equilibrium

Název práce: Vliv acidobazických rovnováh na asociační chování polyelektrolytů

Autor: Roman Staňo

Katedra: Katedra fyzikální a makromolekulární chemie

Školitel: RNDr. Peter Košovan, Ph.D., Katedra fyzikální a makromolekulární chemie

Abstrakt: Makromolekuly jejichž monomérní jednotky nesou náboj, jsou v přírodě rozšířenými stavebními bloky. Struktura a aktivita těchto makromolekul je ovlivněna množstvím náboje na polymerním řetězci, které může být regulováno například prostředníctvím pH. Makromolekulární materiály schopné reagovat na změny pH okolí jsou velice perspektivní pro aplikace jako nosiče pro cílené uvolňování léčiv, nebo jako reverzibilní hydrogely. Fundamentální principy regulace náboje prostřednictvím pH však stále nejsou dostatečně objasněny, a to jak v přírodních, tak syntetických systémech. Důvodem může být nedostatek vhodných teoretických modelů a výpočetních metod. V této práci jsme použili zrhubené modely a molekulové simulace, abychom porozuměli fyzikálním principům acidobazických rovnováh v makromolekulárních systémech ve vztahu k multivalenci a struktuře makromolekul. Představili jsme nový model komplexních koacervátů a použili jej k popisu fázové a rozdělovací rovnováhy v těchto systémech. Prozkoumali jsme vliv multivalentních iontů a nabitých oligomerů na ionizaci lineárních a větvených makromolekul. Srovnali jsme potenciály střední síly mezi ionty různých valencí k prokázání silných korelací mezi nabitými segmenty makromolekul a multivalentními ionty nebo oligomery. Nakonec jsme popsali samoorganizaci opačně nabitých makromolekul, která v závislosti na pH vedla ke vzniku solu nebo elektrostaticky zesíťovaného reverzibilního gelu. Tato diplomová práce představuje kolekci studií acidobazických a fázových rovnováh v různých makromolekulárních systémech, které se navzdory strukturním rozdílům, dají popsat několika málo univerzálními principy.

Klíčová slova: Počítačová simulace, reakční soubor, polyelektrolyt, interpolyelektrolytový komplex, ionizační rovnováha

Contents

Motivation

Weak polyelectrolytes are macromolecules whose monomeric units bear weakly acidic or weakly basic groups. External stimuli, such as pH, regulate the charge on such polymers, and hence their properties. The latter foreshadows weak polyelectrolytes as prospective candidates for the preparation of self-healing materials [HFL$^+$11, LSV$^+$10] or responsive sensors [JG10, FTTO14]. Additionally, the prevalence of polyelectrolytes as building blocks in living systems, such as nucleic acids or polypeptides, inspired the development of tissue scaffolds [Man08, NBP$^+$02] or drug delivery systems [JBLK97, KACD13]. However, the use of polyelectrolytes in such delicate arrangements naturally requires a precise control over their behaviour.

In spite of their widespread applications, the fundamental understanding of polyelectrolytes is still rather poor from both theoretical and experimental perspectives. Theoretical descriptions are complicated by the long-range nature of electrostatic interactions, and the existence of strong correlations due to polymer topology and the presence of charges. From the experimental standpoint, phenomena of polyelectrolyte systems depend on a large number of non-linearly coupled variables. In spite of the deficiency in fundamental understanding, recent years have brought a plethora of impressive experimental results, for example in the field of complex coacervates [SP20]. Mixing of polyanions and polycations leads to a formation of interpolyelectrolyte complex, which can under specific conditions phase separate into a liquid phase called a complex coacervate. A handful of studies were able to utilize complex coacervates as selective biocompatible scavengers able to encapsulate a specific protein from the protein mixtures [DDHS14, vLCL19]. In some cases, the encapsulated protein could be released upon the change of pH, while preserving its secondary structure [BPP$^+$14, ZZ18]. However, the fundamental mechanisms governing the selective and pH-regulated uptake are not clear, further hindering the predictive design of end-use materials.

Moreover, the principles of partitioning of solutes between the phase of coacervate and the co-existing solution is not completely understood not even for small salt ions [ZSAW18, PS15], not to mention complex proteins, or additional effects of the pH [PLP$^+$14]. Judiciously, one of the reasons for the lack of fundamental understanding resides in the fact, that up to this day, a lot of experiments are interpreted in the framework of proto-theories developed decades ago. Specifically for the complex coacervates, the widely used Voorn-Overbeek theory seemingly describes the phase behaviour and salt partitioning in such systems [OV57]. However, its success is based on fortuitous cancellation of errors, yielding a qualitatively correct picture for some features of coacervate behaviour, while completely failing for others [Sin17]. Furthermore, the Voorn-Overbeek theory neglects effects, that have been proven to be important, such as chain connectivity, making a meaningful comparison between the theory and experiment almost impossible [LSA$^+$18].

A similar problem arises also in the question of pH-regulated control of polyelectrolyte behaviour. Experimental determination of the key quantities, such as degree of ionization or charge density, is often only indirect. Analytical theory for such complicated systems is difficult to develop, and often provides only a quali-

tative explanation for the observed phenomena [Mut17]. Nevertheless, a partial remedy for the feeble link between the underlying theory and experiment can be provided by means of computer modelling [LNR$^+$19]. Molecular simulations have proven to be an immensely strong tool connecting the theory and experiments, for example allowing a bottom-up design of sequence-defined polyelectrolyte assemblies [PS20, CLR$^+$17]. Similarly, simulation protocols recently developed in our group came in useful in elucidating the effect of pH on the ionization of ampholytic oligopeptides in dilute solutions [LMH$^+$, LHR$^+$20]. In the last years, a substantial progress has been made in computer simulations of polyelectrolytes, however, different models captured various aspects of polyelectrolytes by different mutually-excluding assumptions. In order to render a predictive material design possible, various features of different models have to be systematically unified.

In this thesis, we used coarse-grained simulations to understand the fundamental physical principles of ionization and ion partitioning in various polyelectrolyte systems, differing in the structure, yet governed by the competition of the same effects. We presented a novel model of complex coacervate to describe the phase behaviour and ion partitioning in such systems. In contrast to experiments, whose results are juxtaposed by an interplay of specific and generic effects, our coarse-grained model allows to decouple the two, and to gain insights into the underlying role of valency of partitioned ions, effects of inter-particle interactions and the Donnan effect. We explored the effect of multivalent ions on ionization of weak polyelectrolytes, and challenged the commonly used analytical mean-field theories, by quantifying the role of inter-particle correlations. Finally, we made use of the derived principles to predict some aspects of a reversible assembly of oppositely charged polyelectrolytes driven by pH.

The thesis is structured as follows. In the first chapter, we commence with a brief overview of theory of polyelectrolyte solutions, gels and complexes. In the second chapter, we outline the core ideas of molecular simulations, focusing on specific Monte Carlo methods used in this thesis. After a brief introduction to coarse-grained models in the third chapter, we present our novel results in chapter four, and conclude the thesis in chapter five.

1. Polyelectrolytes

Look around, and list all items made of polymers. You will very soon realize that polymers play an indispensable part of our daily lives. Bulk materials like plastic, rubber, fabric or fiberglass, functional surfaces, but also solutions of polymers used as glues, paints or hygiene products are just a few examples to give.

Along with synthetic materials, polymers are also nature's prevalent building blocks. DNA, RNA, proteins, polysaccharides or lignin are polymers produced and utilized by living organisms for a broad range of functions.

Interestingly, foundations of macromolecular theory were established only one hundred years ago by Hermann Staudinger. He argued that polymers consist of large molecules composed of a high number of bonded elementary units, as opposed to then theories stating that polymers are big clusters of small molecules [Voh86]. In spite of initial resistance, a macromolecular theory gradually become accepted, and gave birth to polymer science – a vibrant and still active scientific field combining approaches of physics and chemistry to investigate macromolecules.

The opening chapter of this thesis is dedicated to basic description of macromolecules, and especially their specific subclass – polyelectrolytes. Furthermore, we summarize characteristic features of polyelectrolyte solutions and gels. Finally, we review the current knowledge of interpolyelectrolyte complexes, and identify some open questions.

1.1 A brief introduction to macromolecules

This section lists some of differences between macromolecules and molecules of low molecular weight. The theory of ideal chain is introduced to illustrate the fractal-like nature of macromolecules.

Keywords: macromolecule, conformation, polymer, fractal, ideal chain

Macromolecules are molecules composed of a high number of covalently bonded repeating monomeric units. The defining property of a macromolecule is that its physical and chemical properties change only negligibly by removing or adding one more monomeric unit [Voh86, IUP97]. Formally, $\Omega(N) \approx \Omega(N+1)$, where Ω is a physical or chemical property and $N \gg 1$ is the number of monomeric units. In practice, the number of monomeric units usually ranges from 10^2 to 10^5, and molecular weights of macromolecules from 10^4 g/mol to 10^7 g/mol respectively [RC03].

Although a macromolecule is a single molecule, its behaviour is significantly different from that of molecules with small molecular weight. For example, while small molecules usually have one or several equilibrium conformations, typical synthetic macromolecules are more flexible, and attain a vast number of different conformations. Consequently, different conformations contribute to average properties and thus, a description of macromolecules inherently requires statistical approaches.

A typical feature of macromolecules is a hierarchy of characteristic length scales, and associated relaxation time scales [vdM08]. Furthermore, macromolecules behave as fractals, and exhibit self-similarity [Str07, RC03]. On a finite

range of length scales, subsections of a macromolecular chain obey the same statistics as the whole chain, as we illustrate in the next paragraph.

One of the simplest statistical approaches to a description of macromolecules stems from the idea that there is a unique mapping between a conformation of a macromolecule and a random walk, as depicted in Figure 1.1. By construction, this theory neglects correlations between monomeric units separated by a high number of bonds, and therefore is referred to as a theory of the ideal chain. It can be derived [RC03] that the average distance between the ends of a linear macromolecule, R_{ee}, is related to the number of monomeric units as

$$\langle \vec{R_{ee}} \cdot \vec{R_{ee}} \rangle \sim bN^{1/2}, \tag{1.1}$$

where the symbol $\sim$ denotes proportionality, neglecting constant prefactors, and b is the effective size of a monomer. Furthermore, it can be shown that a subsection of a chain composed of $n \gg 1$ monomeric units and its length r_{ee} on average obeys the same power law as the whole chain

$$\langle \vec{r_{ee}} \cdot \vec{r_{ee}} \rangle \sim bn^{1/2}, \tag{1.2}$$

which is a manifestation of the mentioned fractal-like behaviour.

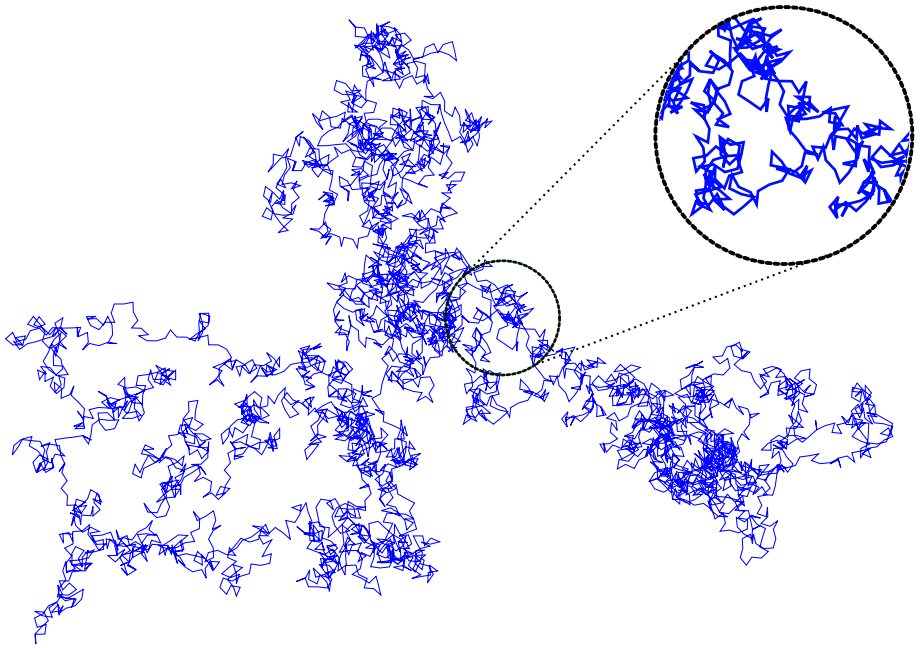

Figure 1.1: Random walk in a plane as a simple model of a macromolecular conformation captures fractal-like nature of a macromolecule. Data were generated by a simulation.

Finally, it is instructive to consider how macromolecules are usually prepared. The most common approach utilizes sequential polymerization reactions such as radical polymerization or polyaddition. This approach usually yields an ensemble of macromolecules of different chain lengths, yet many common properties, as expected from the definition of a macromolecule. A substance composed of macromolecules is a polymer. Experimental techniques such as size exclusion

chromatography combined with mass spectrometry or light scattering allow us to identify the distribution of chain lengths of polymer samples. From the probability distribution it is possible to calculate dispersity – a quantity characterizing the variance of chain lengths in the sample [Mun92]. Lastly, the existence of dispersity gives a motivation for the scaling approach used in (1.1) and for the rest of this thesis. The power law is universal for all chains in the polymer sample, as opposed to an exact equality, in which the specific value of prefactor depends on the chain length.

1.2 Peculiarities of polyelectrolytes

Behaviour of macromolecules becomes significantly more complex by considering charged monomeric units. In this section we describe striking features of charged macromolecules – polyelectrolytes.

Keywords: polyelectrolyte, counterion, Bjerrum length, electrostatic blob

Polyelectrolyte is a macromolecule whose monomeric units bear ionizable groups of the same charge. Typical examples include DNA, RNA, or synthetic polymers such as polyacrylic acid. Ionizable groups of a polyelectrolyte undergo dissociation reaction in aqueous solutions, leaving charge on the chain, and simultaneously releasing oppositely charged ions to the solution. These small ions are called counterions, while small ions with a charge of the same sign as the polyelectrolyte are called co-ions. In addition to polyanions and polycations, we distinguish also polyampholytes as macromolecules which bear both positively and negatively charged monomeric units on the same polymer chain.

The specific features of polyelectrolytes are immanent to the presence of charges, and to long-range nature of Coulomb interaction, as opposed to excluded-volume interactions constituting the main contribution to the Hamiltonian of neutral polymers. As a consequence of electrostatic repulsion between like-charged monomeric units, new characteristic length scales emerge and change the properties of self-similarity, as we show in the next paragraphs [DR05, Dob08, vdM08].

Firstly, we define the Bjerrum length, l_B, as the distance at which Coulomb interaction between two elementary charges is equal to the thermal energy

$$l_\mathrm{B} = \frac{e^2}{4\pi\varepsilon_0\varepsilon_r k_\mathrm{B}T} \qquad \Longrightarrow \qquad U_\mathrm{el.}(r) = \frac{z_1 z_2 e^2}{4\pi\varepsilon_0\varepsilon_r r} \equiv k_\mathrm{B}T\frac{z_1 z_2 l_\mathrm{B}}{r}. \tag{1.3}$$

The physical meaning of the Bjerrum length implies the separation of length scales – for two charges in the distance $r \ll l_\mathrm{B}$, electrostatic interaction overcomes the thermal fluctuations, while for two charges in the distance $r \gg l_\mathrm{B}$, thermal fluctuations become stronger than electrostatic interaction between the charges [HKDL01].

Secondly, we define the electrostatic blob, ξ_e, as the length scale at which the electrostatic energy of a sub-chain is equal to the energy of thermal fluctuations, and we denote the number of monomers contained in one electrostatic blob as g_e [BJ96, DR05]. The blob theory can be generalized for a macromolecule, which is composed of both charged and neutral monomeric units – we denote the number of charged monomers as M, as opposed to the total number of monomers, N,

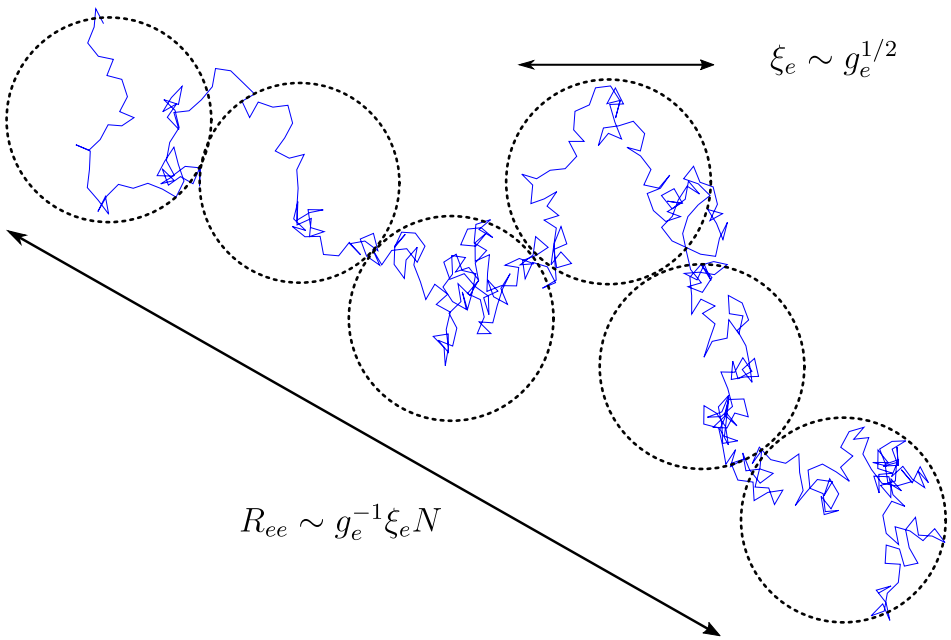

Figure 1.2: Polyelectrolyte as a rod-like chain of electrostatic blob as simple model capturing the essential separation of length scales of a polyelectrolyte. Picture is only schematic.

while $N \geq M \gg 1$. Finally, we get

$$k_{\mathrm{B}}T \frac{l_{\mathrm{B}}(\alpha g_e)^2}{\xi_e} \sim k_{\mathrm{B}}T, \tag{1.4}$$

where $\alpha = M/N$ is the fraction of the charged monomers on the polyelectrolyte – the degree of ionization.

The idea behind the definition of electrostatic blobs is to separate different length scales – polyelectrolyte sub-chain of a length $r \gg \xi_e$ contains electrostatic energy higher than the energy of thermal fluctuations and thus, dominates the behaviour, and stretches the chain to the rod-like array of electrostatic blobs with a size

$$R \sim \xi_e \frac{N}{g_e} \sim (u\alpha)^{1/3}\, bN, \tag{1.5}$$

where $u = l_{\mathrm{B}}/b$ is the electrostatic coupling. On the other hand, polyelectrolyte sub-chain of a length $r \ll \xi_e$ is dominated by thermal fluctuations, and obeys the ideal statistics as

$$\xi_e \sim b g_e^{1/2}. \tag{1.6}$$

Finally, in Figure 1.2 we summarize the power laws emerging from the theory of electrostatic blob.

We see that the average distance between the ends of a polyelectrolyte scales as N, as opposed to the ideal chain which scales as $N^{1/2}$. Therefore, polyelectrolytes are on average more extended than neutral polymers, which is exhibited for example by an increase in the viscosity of solutions of polyelectrolytes as compared to solutions of neutral polymers [Dob08]. The above mentioned theory of electrostatic blob gives by no means a full description. It assumes additivity

of electrostatic energies of blobs, disregards influence of counterions, or quality of the solvent [KKK48, Dob08]. However, it still provides a simple argument, demonstrating distinctive features of polyelectrolytes in comparison with neutral chains.

So far, we have neglected the presence of counterions, that also play a role in the solutions of polyelectolytes. For example, counterions dominate the osmotic pressure, Π, of polyelectrolyte solutions which is significantly higher than osmotic pressures of solutions of neutral polymers as follows from the virial expansion

$$\frac{\Pi}{k_{\mathrm{B}}T} = \left[\frac{c_{\mathrm{mon}}}{N} + \frac{\alpha N c_{\mathrm{mon}}}{N} + \frac{v c_{\mathrm{mon}}^2}{2} + w c_{\mathrm{mon}}^3 + \dots\right] \approx \alpha c_{\mathrm{mon}} \gg \frac{c_{\mathrm{mon}}}{N}, \tag{1.7}$$

where v is excluded-volume, w three-body interaction virial coefficient, and c_{mon} molar concentration of monomeric units. Additionally, at sufficiently high charge densities, counterions strongly interact with polyelectrolyte chain, as we show in the following section.

1.3 The role of counterions

Here we review some principles governing the distribution of counterions around polyelectrolytes and introduce the phenomenon of counterion condensation.

Keywords: Manning theory, condensation threshold, electrostatic coupling

In solutions, charges concentrated on polyelectrolyte chains create strong electric fields. Naturally, counterions with the opposite charge tend to distribute themselves preferentially around the chain, thereby lowering the interaction energy. However, by close localization in the vicinity of polyelectrolytes, the translational entropy of counterions is lowered as well. Localization and distribution of counterions is driven by a fine interplay of the above mentioned entropic and enthalpic effects. If the translational entropy dominates the free energy, counterions are scattered in the whole solution. On the other hand, if attractive interactions dominate the free energy, counterions accumulate in the close proximity to the chain, and we observe the phenomenon of counterion condensation [Man69, Oos57, FKL51, NN06, DHM00].

To give a simple physical description, let us assume an infinitely long rigid rod-like polyelectrolyte with a linear charge density Γ surrounded by monovalent counterions. According to the Gauss theorem, electrostatic potential, $\psi(r)$, in the field of the rigid rod in the distance r is

$$\psi(r) = \frac{\Gamma}{2\pi\varepsilon_0\varepsilon_r}\ln(r). \tag{1.8}$$

Now we assume that the small ions obey the Boltzmann distribution, and electrostatics is the only component of the interaction energy. Then, the density of monovalent counterions, $c(r)$, in the distance r is

$$c(r) = c(r\to\infty)\exp\left(-\frac{e\psi(r)}{k_{\mathrm{B}}T}\right) = r^{-2l_{\mathrm{B}}\Gamma}. \tag{1.9}$$

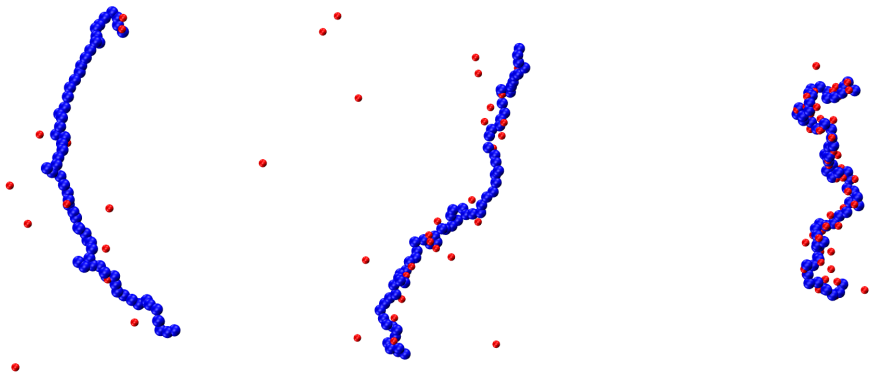

(a) $u = 1$ (b) $u = 2$ (c) $u = 6$

Figure 1.3: Simulation snapshots of strong polyelectrolyte of length $N = 64$ with monovalent counterions in a salt-free solution for various values of the electrostatic coupling.

Finally, we calculate the total number of counterions in the distance from the chain smaller than r as an integral of density profiles

$$\mathcal{N}(r) = \int_0^r \mathrm{d}x \; 2\pi x \; c(x) = \int_0^r \mathrm{d}x \; 2\pi c_0 \; x^{1-2l_\mathrm{B}\Gamma}, \tag{1.10}$$

We see that, if $l_\mathrm{B}\Gamma > 1$ integral (1.10) diverges at its lower bound, which indicates counterion condensation [BJ96] – very strong localization of counterions in the vicinity of the polyelectrolyte. Condensed counterions suppress the electric field of the chain, and renormalize the effective charge density on the polymer to $\Gamma = 1/l_\mathrm{B}$. To make a link to the scaling theory mentioned before, condensation threshold can be in the blob approach reformulated as follows: if $(u\alpha)^{1/3} < 1$, translational entropy dominates the free energy, and we observe no condensation. If $(u\alpha)^{1/3} > 1$, fraction η of counterions is free, and $1 - \eta$ of all counterions condense on the chain, and thus renormalize the charge density to the effective charge density $u^2\alpha\eta = 1/l_\mathrm{B}$. We illustrate the condensation by comparing computer simulation snapshots in Figure 1.3 at different values of electrostatic coupling. For $u = 1$ in Figure 1.3a, the average linear charge density on the chain is $1/l_\mathrm{B}$, which is the condensation threshold for a rigid rod. The polymer in the simulation is flexible, but qualitative picture remains the same as for the rigid rod – we do not observe significant condensation, and the chain is rather extended. Condensation becomes noticeable at $u = 2$ and $u = 6$. In the latter case, a higher fraction of counterions is condensed, and the chain is more collapsed, as compared to the former case, where a smaller amount of counterions is needed to renormalize the charge density.

The presented arguments by no means present a complete theory, but rather a simple example of a strong coupling between the polyelectrolyte and counterions. More sophisticated theories [HJK$^+$04, BJ96, NN06] based on Poisson-Boltzmann equation are able to incorporate for example conformational changes connected to the condensation.

Counterion condensation is a phase transition of the second order. Experimental approaches to follow the condensation are often based on measuring the

osmotic pressure or conductivity of polyelectrolyte solutions. Condensation leads to a decrease in the magnitude of the quantities mentioned above, since they are both dominated by free counterions [RdCL00]. Furthermore, condensation decreases also the electrophoretic mobility of the polyelectrolyte chain by lowering its effective charge [BJ96].

1.4 Polyelectrolyte charge regulation

So far we have discussed only so called strong polyelectrolytes which bear quenched (permanent) charges. In contrast, weak polyelectrolytes are composed of monomeric units with variable ionization which depends on factors such as pH or salt concentration. Therefore, external stimuli can regulate the charge fraction on the polymer, and thus its properties. In this section, we introduce theoretical principles of thermodynamics of ionization of simple acids, and extend them to polyelectrolytes. Furthermore, we illustrate some specific elements of weak polyelectrolyte behaviour.

Keywords: ionization, weak polyelectrolyte, titration, polyelectrolyte effect

Weak (annealed) polyelectrolytes are composed of monomeric units whose ionizable groups are weakly acidic or weakly basic. The most prominent example is poly(acrylic) acid (PAA) whose weakly acidic groups participate in acid-base reactions

$$\mathrm{R{-}COOH} \rightleftharpoons \mathrm{R{-}COO^- + H^+}. \tag{1.11}$$

The key quantity to describe the average ionization state of monomeric units is the degree of ionization, defined for the specific case of PAA as

$$\alpha = \frac{c_{\mathrm{R-COO^-}}}{c_{\mathrm{R-COO^-}} + c_{\mathrm{R-COOH}}}, \tag{1.12}$$

where c is the concentration. The condition of thermodynamic equilibrium involving chemical reactions is formulated as

$$0 = \mathrm{d}\mathcal{G} = V\mathrm{d}p - \mathcal{S}\mathrm{d}T + \sum_i \left(\frac{\partial \mathcal{G}}{\partial N_i}\right) \mathrm{d}N_i, \tag{1.13}$$

where N_i is the number of species, $\mathcal{G}$ is Gibbs free energy, V is volume and $\mathcal{S}$ is entropy. Furthermore, if we impose a fixed temperature, T, and pressure, p, the condition (1.13) simplifies to

$$0 = \sum_i \left(\frac{\partial \mathcal{G}}{\partial N_i}\right) \mathrm{d}N_i = \sum_i \nu_i \mu_i \tag{1.14}$$

where μ_i is the chemical potential and ν_i is the stoichiometric coefficient of species i. The chemical potential is usually decomposed into three additive parts

$$0 = \sum_i \nu_i \mu_i = \sum_i \nu_i (\mu_i^{\ominus} + \mu_i^{\mathrm{id.}} + \mu_i^{\mathrm{ex.}}), \tag{1.15}$$

where $\mu_i^{\ominus}$ is the standard chemical potential which is an arbitrary reference state, $\mu_i^{\mathrm{id.}}$ is the ideal chemical potential and $\mu_i^{\mathrm{ex.}}$ is the excess chemical potential.

For the specific case of ionization reaction [LNR$^+$19], we can combine the standard chemical potentials into the acidity constant, K_A, and define the pH [ELO$^+$94] as

$$K_\mathrm{A} = -\frac{1}{k_\mathrm{B}T}\sum_i \nu_i \mu_i^\ominus, \qquad \mathrm{pH} = \frac{\mu_{\mathrm{H}^+}^\ominus - \mu_{\mathrm{H}^+}}{k_\mathrm{B}T\ln(10)}. \tag{1.16}$$

It can be shown [McQ73] that the ideal chemical potential attains the form

$$\mu_i^{\mathrm{id.}} = -k_\mathrm{B}T\ln\left(\frac{c_i}{c_i^\ominus}\right), \tag{1.17}$$

where c_i is concentration and $c_i^\ominus$ is the reference concentration corresponding to the chemical potential of the reference state.

Now, let us assume non-interacting ideal gas which means that $\forall i:\ \mu_i^{\mathrm{ex.}} = 0$, and thus we obtain the common approximation for pH

$$\mathrm{pH} \overset{\mathrm{ideal}}{=} -\log\left(\frac{c_{\mathrm{H}^+}}{c^\ominus}\right). \tag{1.18}$$

Finally, we rearrange the condition of chemical equilibrium (1.14) using (1.16) to obtain the Henderson-Hasselbalch equation:

$$\frac{1}{\alpha} \overset{\mathrm{ideal}}{=} 1 + 10^{-(\mathrm{pH}-\mathrm{p}K_\mathrm{A})}. \tag{1.19}$$

Behaviour of monoprotic acids in dilute aqueous solutions at ionic strengths $I \lesssim 10$ mM is well approximated by the Henderson-Hasselbalch equation. The assumption of zero excess chemical potential breaks down at higher concentrations of species, where interactions become important. Similarly, titration curves of multiprotic acids deviate from the ideal one because of strong intramolecular interactions between ionizable groups [Arn57, KS47]. A polyelectrolyte chain bearing $M \gg 1$ ionizable groups can attain $\sim 2^M$ ionization states which leads to smooth titration curves, as opposed to stepwise curves of diprotic acids. Furthermore, due to mutual proximity of a big number of charges, weak polyelectrolytes present highly non-ideal systems even at high dilutions [LNR$^+$19, NUK17].

To include the contribution of interactions, we rewrite the condition of equilibrium (1.14) [MKJ$^+$18, LNR$^+$19]

$$\mathrm{pH} - \mathrm{p}K_\mathrm{A} = \log\left(\frac{\alpha}{1-\alpha}\right) + \frac{1}{k_\mathrm{B}T\ln(10)}\sum_{i\neq\mathrm{H}^+}\nu_i\mu_i^{\mathrm{ex.}} = \log\left(\frac{\alpha}{1-\alpha}\right) + \Delta. \tag{1.20}$$

This allows us to rewrite Henderson-Hasselbalch equation in three equivalent forms

$$\mathrm{pH} - \mathrm{p}K_\mathrm{A} - \Delta = \mathrm{pH} - \mathrm{p}K_{\mathrm{eff.}} = \mathrm{pH}_{\mathrm{eff.}} - \mathrm{p}K_\mathrm{A} = \log\left(\frac{\alpha}{1-\alpha}\right), \tag{1.21}$$

where we have introduced two new quantities: effective pK_A and effective pH – both often used in experiments to characterize the polyelectrolyte ionization.

Now we outline the original theory [KG49] that provides a link between the average ionization of a weak polyelectrolyte and pH. Following Ref. [KG49], assuming a homogeneous charge distribution on the chain, the Debye-Hückel approximation for interactions between charges, and neglecting inter-particle correlations with counterions, one can derive

$$\Delta = \mathrm{pH} - \mathrm{p}K_{\mathrm{eff.}} \sim \alpha^{1/3} u^{2/3}. \tag{1.22}$$

Equation (1.22) suggests that $\mathrm{p}K_{\mathrm{eff.}}$ is an increasing function of α and thus, as the polyelectrolyte gets more charged, its ionization gradually costs more free energy. Electrostatic repulsion between accumulating charges on the chain therefore suppresses the ionization of a polyelectrolyte with respect to the ideal case. Figure 1.4 shows that titration curve of a free monomer follows the ideal curve, but with increasing chain length, a polyelectrolyte is less ionized than the free monomer at the same pH. Furthermore, the shift of the titration curve firstly increases with the chain length, but is diminished for a sufficiently long chain, suggesting that these deviations are mainly a local effect of the nearest groups.

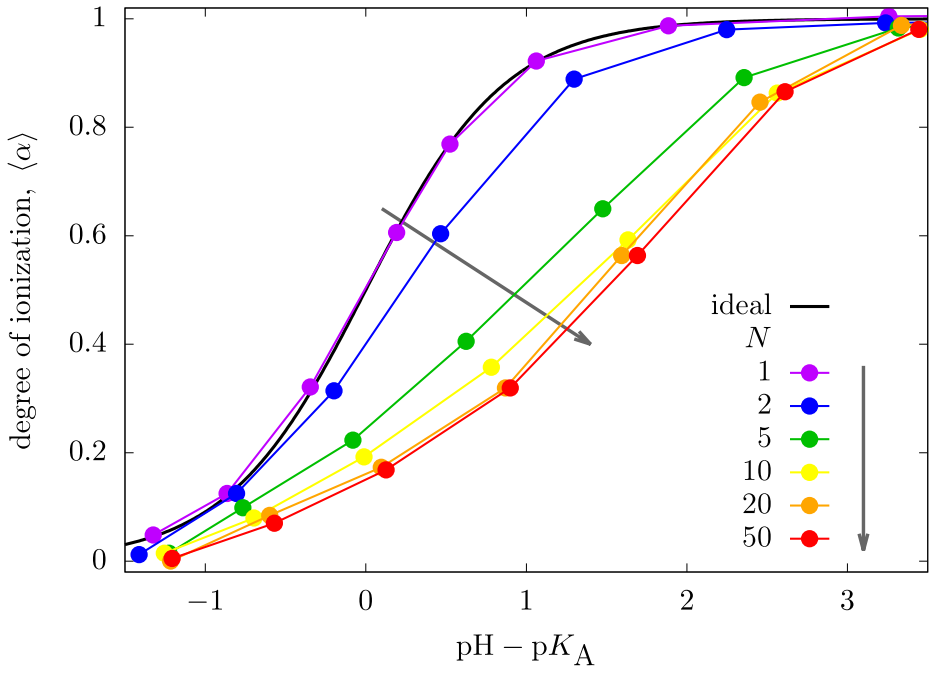

Figure 1.4: Degree of ionization of a linear weak polyelectrolyte as a function of $\mathrm{pH} - \mathrm{p}K_{\mathrm{A}}$ for chains of various lengths. The data are from Ref. [NUK17] and were digitalized and replotted with the author's permission.

Another factor affecting the shift and deformation of titration curves is the polymer concentration. Figure 1.5 shows that diluting a polyelectrolyte in a salt-free solution leads to a greater deviation from the ideal titration curve, as opposed to monoprotic acids whose behaviour approaches the ideal one upon dilution. This difference can be attributed to electrostatic screening. Higher concentration of polyelectrolyte leads to a higher concentration of released counterions, and stronger screening effects which suppress repulsions between the like charges of the chain, and thus promote the ionization [NUK17].

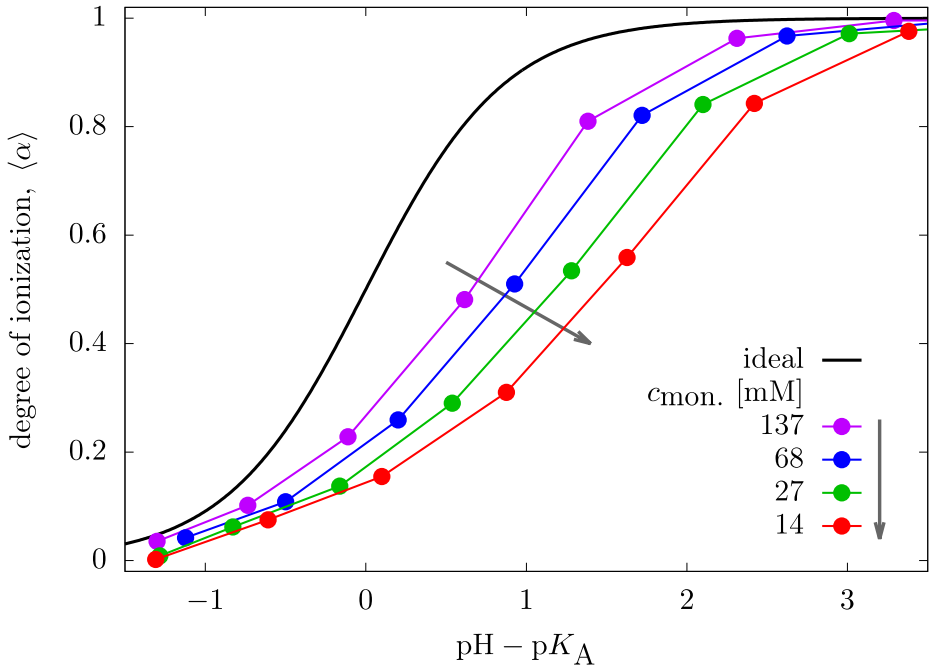

Figure 1.5: Degree of ionization of a linear weak polyelectrolyte of length $N = 100$ as a function of pH − pK_A for different concentrations of monomeric units. The data are from Ref. [NUK17] and were digitalized and replotted with the author's permission.

Finally, we consider the conformational response of the ionization of a polyelectrolyte. Typically, the polymer expands with increasing ionization, and charge density accumulates at the ends, where the number of charges within the Bjerrum length is minimized. However, if the charge density exceeds the condensation threshold, counterions condense on the polyelectrolyte, which leads to a partial collapse of the chain. Ionization together with conformation and counterion distribution form a complex feedback loop.

In spite of the widespread applications of weak polyelectrolytes as pH-responsive materials [JG10, JK09, PD04, QP01], their behaviour is still not completely understood. The role of inter-particle interactions and correlations, the complex interplay of ionization and conformation, the presence of a nano-heterogeneity and a multitude of characteristic length scales all drastically complicate the development of reliable and universal analytical descriptions [BZL$^+$11]. However, some of the mentioned effects can be included by approximative means into numerical mean-field calculations [UKL$^+$14]. In contrast to the mean-field models, molecular simulations account for the above mentioned effects implicitly, and thus present a very strong tool in the contemporary research into weak polyelectrolytes [LNR$^+$19].

1.5 Polyelectrolyte gels

Previously, we have discussed only polyelectrolytes in dilute aqueous solutions. However, polyelectrolytes exist in a broad range of concentration regimes, and are endowed with a rich phase behaviour. This section is devoted to polyelectrolyte

hydrogels important for a broad range of practical applications such as superabsorbents [HKDL01], nanoreactors [DDKK11], or desalination devices [HKW10].

Keywords: gelation, network, percolation, swelling, Donnan effect

Introduction of inter-chain cross-links into a solution of polymer chains results in a sol – a polydisperse solution of branched polymers. Cross-links can be created by formation of covalent bonds but also by hydrogen bonds, or electrostatic attractions between monomeric units. As the amount of cross-links in the sol increases, branched polymers constitute progressively bigger molecules. At some point, only one big molecule spans the whole system. Such a continuous percolating network of connected polymer chains is called a gel. Because of its cross-linked structure, submerging a gel into a solvent does not dissolve it. Instead, a two-phase system of a swollen gel and a reservoir is created [Pou08, RC03].

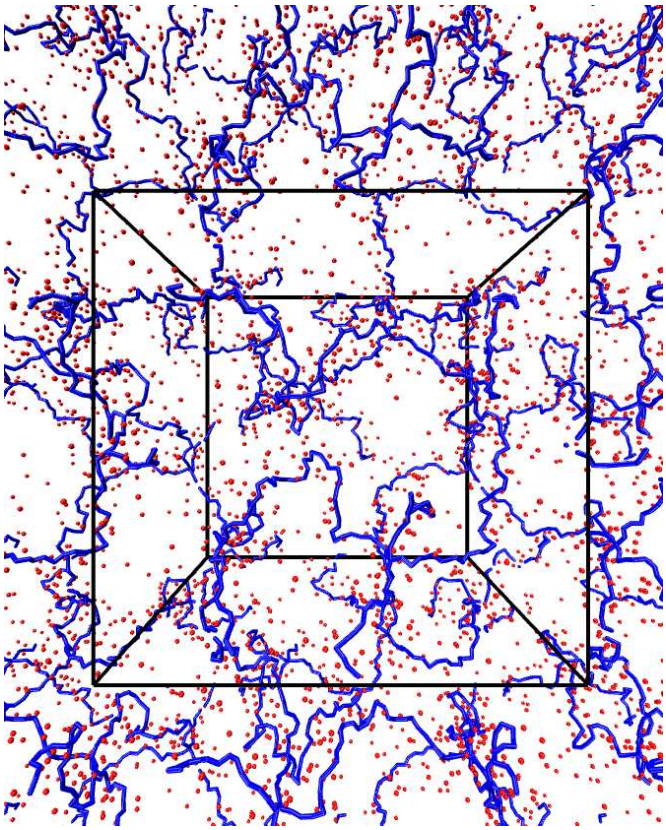

Figure 1.6: Simulation snapshot of a periodic strong polyelectrolyte gel with counterions. The black box depicts one cell of the gel, surrounded by its periodic images.

If the solvent is water, the gel is called a hydrogel [MKH06, MHK05]. A macroscopic phase of a polyelectrolyte hydrogel can not bear a net charge [SS89], and the gel thus contains counterions neutralizing the backbone charges, as depicted in Figure 1.6. Polyelectrolyte hydrogels coupled to a reservoir of water swell significantly stronger in comparison with neutral gels. On one hand, the swelling is promoted by electrostatic repulsion between like charges, stretching the chains. In addition, the swelling is promoted also by osmotic pressure of the counterions [LNR$^+$19]. The presence of counterions in the gel lowers the chemi-

cal potential of water within, and causes an accumulation of solvent in the gel, which results in swelling. However, chain entropy acts against the swelling and an intricate interplay of the mentioned effects results in the state of free-swelling equilibrium, commonly described by the swelling ratio $Q = V_{\mathrm{gel}}/V_{\mathrm{dry}}$, where V is volume. The key idea of theoretical description of hydrogels is that free-swelling equilibrium is a result of mechanical and chemical equilibrium between the gel and the reservoir.

The former can be written in a form of equation of state of the gel as

$$\mathcal{P}^{\mathrm{res}} = -\frac{\partial \mathcal{F}^{\mathrm{gel}}}{\partial V_{\mathrm{gel}}} = \mathcal{P}^{\mathrm{gel}}, \tag{1.23}$$

where $\mathcal{P}$ is the pressure.

The latter is defined by the equality of the chemical potentials of those species which can be exchanged between the gel and the reservoir – small ions. An important starting point theory describing such a two-phase equilibrium is the Donnan theory [Don24]. Consider an ionic gel of monomeric units A^- neutralized by Na^+ counterions coupled to a reservoir of NaCl, neglecting H^+ and OH^-. Polymer segments A^- are present only in the gel, while other ions can be exchanged between the phases. In chemical equilibrium, the chemical potential of exchangeable ionic pairs in both phases has to be equal, therefore:

$$\mu^{\mathrm{gel}}_{\mathrm{Na^+Cl^-}} = \mu^{\mathrm{res}}_{\mathrm{Na^+Cl^-}} \Longrightarrow \mu^{\mathrm{gel}}_{\mathrm{Na^+}} + \mu^{\mathrm{gel}}_{\mathrm{Cl^-}} = \mu^{\mathrm{res}}_{\mathrm{Na^+}} + \mu^{\mathrm{res}}_{\mathrm{Cl^-}}. \tag{1.24}$$

If we assume ideal behaviour, we can rewrite (1.24) using (1.17) as:

$$c^{\mathrm{gel}}_{\mathrm{Na^+}} c^{\mathrm{gel}}_{\mathrm{Cl^-}} = c^{\mathrm{res}}_{\mathrm{Na^+}} c^{\mathrm{res}}_{\mathrm{Cl^-}} \Longrightarrow \Xi_+ = \frac{c^{\mathrm{gel}}_{\mathrm{Na^+}}}{c^{\mathrm{res}}_{\mathrm{Na^+}}} = \frac{1}{\Xi_-} = \frac{c^{\mathrm{res}}_{\mathrm{Cl^-}}}{c^{\mathrm{gel}}_{\mathrm{Cl^-}}}, \tag{1.25}$$

where we defined the partition coefficients between reservoir and gel, Ξ_+ and Ξ_- for Na^+ and Cl^- respectively. Finally, we take into account electroneutrality of each of the phases as

$$c^{\mathrm{gel}}_{\mathrm{A^-}} + c^{\mathrm{gel}}_{\mathrm{Cl^-}} = c^{\mathrm{gel}}_{\mathrm{Na^+}} \qquad \text{and} \qquad c^{\mathrm{res}}_{\mathrm{Na^+}} = c^{\mathrm{res}}_{\mathrm{Cl^-}}. \tag{1.26}$$

Plugging (1.26) into (1.25), we see that

$$\Xi_+ = \frac{c^{\mathrm{gel}}_{\mathrm{A^-}}}{2I^{\mathrm{res}}} + \sqrt{\left(\frac{c^{\mathrm{gel}}_{\mathrm{A^-}}}{2I^{\mathrm{res}}}\right)^2 + 1}, \tag{1.27}$$

where $2I^{\mathrm{res}} = (c^{\mathrm{res}}_{\mathrm{Na^+}} + c^{\mathrm{res}}_{\mathrm{Cl^-}})$. Equation (1.27) shows that concentration of counterions in the gel is higher than their concentration in the reservoir. Conversely, concentration of co-ions in the gel is lower, as compared to their concentration in the reservoir. Such an unequal partition of different ions is called the Donnan effect, and is controlled by the parameter $c^{\mathrm{gel}}_{\mathrm{A^-}}/2I^{\mathrm{res}}$. We see that unequal partitioning of counterions and co-ions is prevailing if $I^{\mathrm{res}} \ll c^{\mathrm{gel}}_{\mathrm{A^-}}$. On the other hand, if $I^{\mathrm{res}} \gg c^{\mathrm{gel}}_{\mathrm{A^-}}$, then $\Xi_+ \approx \Xi_- \approx 1$, suppressing the Donnan effect. The Donnan theory may be extended by including H^+ and OH^-, which gives rise to an important observation: $\mathrm{pH}^{\mathrm{gel}} \neq \mathrm{pH}^{\mathrm{res}}$, that is a consequence of unequal partitioning of H^+ ions. This is important when dealing with weak polyelectrolyte gels [LOdlCS11], where charge fraction in the gel is coupled to ionic concentrations.

Coupling of ionic partitioning to chain swelling forms a feedback loop, further complicated by high non-ideality of polyelectrolyte gels. Different theoretical approaches [KM55, FR43, RRB$^+$17, Lan20, LSK$^+$19] are usually based on decomposition of $\mathcal{F}^{\text{gel}}$ in (1.23) into various contributions, assumed to be additive and mutually independent, such as free energy of stretching, free energy of electrostatic interactions, ... and evaluating them self-consistently in numerical calculations.

1.6 Complex coacervates

We bring this chapter to an end by presenting complex coacervates – a class of liquid materials defined by electrostatically-driven association of polycations and polyanions. Complex coacervates have been used in food industry [ST11] or hygiene products [Was10] for decades. There has been recently a renaissance in the understanding of coacervates [SP20], and a plethora of new biophysical applications emerged – selective protein encapsulation [vLCL19, BPP$^+$14], gene therapy or highly-tunable self-assembly [CLR$^+$17, LCM$^+$19, PS20] are just a few examples to mention. Herein, we list a few characteristics of the behaviour of complex coacervates, and outline theoretical approaches to their description.

Keywords: complex coacervate, liquid-liquid phase separation, Voorn-Overbeek

Mixing of solutions of polyanions and polycations results in the formation of interpolyelectrolyte complexes [vdGSLCS11, YDF$^+$14]. Depending on the conditions, these complexes can be soluble, but they can also phase separate into a solid precipitate or a liquid phase, co-existing with the solvent. If the latter is the case, we observe the phenomenon of complex coacervation. The dense liquid phase with a high content of polyanion-polycation complexes is then called a complex coacervate [VdKCS09, SP20].

Naturally, polycations and polyanions exhibit strong electrostatic attractions, however the formation of the complex is driven entropically by the counterion release [OM06, SYDW19, FS16]. In a solution of very dilute polyelectrolytes a fraction of counterions is condensed on the chains, renormalizing the charge density to one elementary charge per Bjerrum length (see Section 1.3). However, by the formation of a complex, polycations and polyanions effectively mutually neutralize each other, resulting in a release of the condensed counterions into the solution. The free energy gain is of the order $\sim k_{\text{B}}T$ per one released counterion. Considering a typical length of polyelectrolytes, the driving force is so strong, that it is possible to prepare also non-stoichiometric coacervates with excess of either polycation or polyanion respectively [ZAWW18, vLCL19]. Intuitively, the formation and properties of complex coacervates depend on various conditions such as salt concentration and valency, solvent quality or architecture of polymers [SP20]. Stability of coacervates with respect to such conditions is usually described in the form of phase diagrams.

Figure 1.7 shows a typical salt content-vs.-polymer content phase diagram of a complex coacervate. The phase of a complex coacervate is often referred to as the polymer-rich phase, and it often contains the polyelectrolyte in $\sim 0.1\text{M} - 8\text{M}$ monomer concentrations, which translates to roughly $10\% - 30\%$ volume fraction

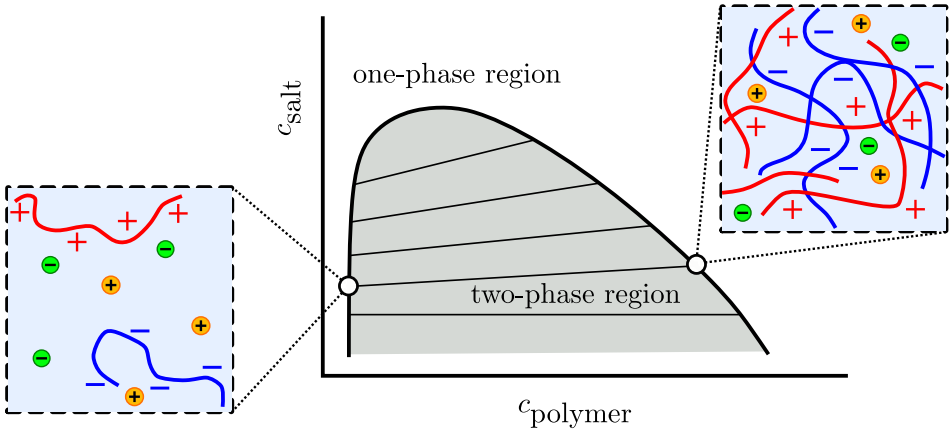

Figure 1.7: Scheme of a phase diagram of a complex coacervate in salt content-polymer content plane. Tie-lines within the two phase region connect the states which co-exist in equilibrium. Boxes with dashed borders illustrate the polymer-poor phase (left) and the co-existing polymer-rich phase (right).

of the polymer [Sin17]. The polymer-poor phase co-existing with the coacervate contains mainly solvent and salt, while the polymer content is typically very low [LSA+18], as illustrated by steep slope of the binodal at low c_{polymer} in Figure 1.7. It is important to notice that tie-lines connecting the simultaneously co-existing states in Figure 1.7 are not parallel to the c_{polymer} axis, indicating unequal partitioning of salt between the phases, measured in a number of studies [LSA+18, SWB+10, ZSAW18]. Additionally, if the salt concentration in the system is sufficiently high, the phase separation is not observed, and interpolyelectrolyte complexes are dissolved in a single phase, as exhibited by the maximum on the binodal in Figure 1.7, which indicates the critical point [PLP+14].

The first successful theory of complex coacervation was presented by Voorn and Overbeek [OV57, MOV57]. The Voorn-Overbeek theory considers that the complex coacervate is composed of five components – negatively and positively charged polymer segments, negatively and positively charged salt ions, and the solvent. The theory estimates the free energy of mixing the polyelectrolytes as [Sin17]

$$\frac{a^3 \Delta \bar{\mathcal{F}}_{\text{mix.}}}{V k_{\text{B}} T} = \sum_i \frac{\phi_i}{N_i} \ln(\phi_i) - \frac{2}{3}\sqrt{\pi}\left(\frac{l_{\text{B}}}{a}\sum_i \sigma_i \phi_i\right)^{3/2} + \sum_i \sum_{j>i} \chi_{ij} \phi_i \phi_j, \qquad (1.28)$$

where each component i has the charge density σ_i and the volume fraction ϕ_i, a is the size of a monomer, V the volume of the system, and χ_{ij} the Flory-Huggins χ-parameter [RC03] between components i and j. The first term in (1.28) accounts for translational entropy in the complex, in analogy with Florry-Huggins lattice theory [RC03]. The second term is the contribution of electrostatic interactions, and emerges by employing the Debye-Hückel approximation. The third term partially accounts for excluded-volume interactions such as hydrophobicity of polymers. This term was not considered in the original theory, however its inclusion brings more flexibility to the theory with respect to interpretation of experiments. The Voorn-Overbeek theory predicts formation of the complex

coacervate, and has been widely used to fit experimental phase diagrams [SP20]. Nevertheless, the theory is based on many simplifications, and its success is based on cancellation of errors: first, the theory assumes the limit of weak charge correlations and neglects polymer connectivity – both promote the formation of the complex; second, the theory does not fully treat steric repulsions, which decrease the stability of the complex.

In recent years, a lot of progress has been made in development of more sophisticated theories describing complex coacervates [Mut17, Sin17]. Random phase approximation [CJ01], liquid state integral equations [PS15] or Transfer matrix formalism [LS17] are just few examples to give. Each of these approaches has only limited range of applicability [Lyt19], and connection to experiments is often non-trivial. A common motif of these theories is that they often fail at the high charge densities and at long length scales. Unfortunately, precisely this regime has a great potential for bio-applications, and therefore the need for a universal coacervate theory still remains present.

2. Molecular simulations

For centuries, the philosophy of science distinguished theory and experiment. However, with the advancement of computers in the 1950s a new scientific approach emerged. Computer simulations stand between theory and experiment with which they assemble the holy trinity of science. Simulations allow to carry out virtual experiments and therefore develop and test theoretical models. Furthermore, with a proper model, one could in principle use simulations to predict or interpret real-life experiments.

In principle, simulations provide numerically exact results for a given model. Therefore, the limiting factors of computer simulations are mainly quality of a model, and complexity of the involved calculations. Indeed, more sophisticated models tend to give more accurate results, but a more sophisticated model usually means also a more expensive simulation. It is believed that the most accurate description of nature is given by the principles of quantum mechanics. Simulations employing these schemes which require only fundamental constants of the universe are called ab-initio simulations. However, it is possible to employ ab-inito calculations only for systems composed of few hundreds of atoms. In polymer science, we usually use molecular modelling based on principles of statistical thermodynamics, classical mechanics and numerical mathematics.

This chapter describes how molecular simulations are usually carried out, and what is their main goal. Afterwards, we introduce some specific methods used in this thesis.

2.1 Bridging the micro and the macro scales

Classical thermodynamics provides a powerful framework for a description of a state of matter using measurable macroscopic properties, such as pressure or temperature. However, the theory fails to incorporate chemical details in other way than just by introducing material constants which need to be measured experimentally. Statistical thermodynamics goes beyond the principles of classical thermodynamics, and provides a direct relation between the macroscopic properties and the microscopic properties, such as molecular geometry or intermolecular interaction potentials. This section introduces the basic principles of statistical thermodynamics – a discipline linking physics and chemistry via statistics.

Keywords: statistical thermodynamics, canonical ensemble, partition function

In classical thermodynamics, a sample of a matter in equilibrium is completely defined by a small set of independent macroscopic thermodynamic quantities, such as pressure, volume or temperature. We refer to such a state of a sample as the macrostate. The idea of statistical thermodynamics is that each macrostate can be realized by a vast number of microstates consistent with the small set of macroscopic quantities. The motivation stems from the fact that during any measurement, the sample undergoes microscopic changes, and any experimentally measured macroscopic quantity is actually an average over different states of the observed system.

Classical statistical thermodynamics assumes that a microstate is completely defined by specifying the momentum, $\mathbf{p}$, and the position, $\mathbf{q}$, of all particles in the system [McQ73, NKK02]. For an N-particle system, we will denote such a set of values as

$$\{\mathbf{p}_1, \ \dots \ , \mathbf{p}_N\}, \{\mathbf{q}_1, \ \dots \ , \mathbf{q}_N\} \equiv (\mathbf{p}^N, \mathbf{q}^N). \tag{2.1}$$

Each microstate can be realized with a specific probability which gives rise to a certain probability distribution of possible microstates for a given macrostate. Let us assume a collection of all such microstates, where each microstate is represented with a frequency proportional to the probability of its realization. Such a virtual collection is called a statistical ensemble. To give an example, we assume a system in a rigid impermeable container submerged in a heat bath. By construction, the system has a constant number of particles, constant volume, constant temperature, and is called canonical ensemble which we denote as $[N, V, T]$. It can be shown that probability of realization of a given microstate, $P_{[N,V,T]}(\mathbf{p}^N, \mathbf{q}^N)$, obeys the Boltzmann distribution

$$P_{[N,V,T]} \sim \exp(-\beta \mathcal{E}(\mathbf{p}^N, \mathbf{q}^N)), \tag{2.2}$$

where $\beta = 1/k_\mathrm{B}T$ and $\mathcal{E}$ is the energy of the system [McQ73, Tuc10].

The central object of the interest in statistical mechanics is the partition function, $Q_{[N,V,T]}$, defined as

$$Q_{[N,V,T]} = \int \mathrm{d}\mathbf{p}^N \int \mathrm{d}\mathbf{q}^N \exp(-\beta \mathcal{E}(\mathbf{p}^N, \mathbf{q}^N)), \tag{2.3}$$

where we are integrating over momenta, $\mathbf{p}$, and coordinates, $\mathbf{q}$, of each of N particles in the system. It can be shown that the macroscopic quantities follow as functionals of the partition function. Therefore, knowing the partition function means obtaining a direct connection between microscopic properties of molecules like intermolecular potentials or geometries and macroscopic properties like pressure or free energy.

Furthermore, we assume that the total energy can be decomposed to two orthogonal components – the kinetic energy, $\mathcal{K}$, and the potential energy, $\mathcal{U}$, as

$$\mathcal{E}(\mathbf{p}^N, \mathbf{q}^N) = \mathcal{K}(\mathbf{p}^N) + \mathcal{U}(\mathbf{q}^N). \tag{2.4}$$

By using the classical prescription for kinetic energy, and by plugging the assumption (2.4) to the definition (2.3) we can partially solve the partition function as

$$Q = \int \mathrm{d}\mathbf{p}^N \exp(-\beta \mathcal{K}(\mathbf{p}^N)) \int \mathrm{d}\mathbf{q}^N \exp(-\beta \mathcal{U}(\mathbf{q}^N)), \tag{2.5}$$

$$Q = \left(\frac{2\pi m k_\mathrm{B} T}{h^2}\right)^{3N/2} \int \mathrm{d}\mathbf{q}^N \exp(-\beta \mathcal{U}(\mathbf{q}^N)), \tag{2.6}$$

$$Q = \left(\frac{2\pi m k_\mathrm{B} T}{h^2}\right)^{3N/2} Z_N, \tag{2.7}$$

where h is the Planck constant, m is the mass of a particle, and Z_N is the configuration integral. Ensemble average of a quantity $\mathcal{A}$ which is a function of positions only is then

$$\langle \mathcal{A} \rangle = \frac{1}{Z_N} \int \mathrm{d}\mathbf{q}^N \exp\left(-\beta \mathcal{U}(\mathbf{q}^N)\right) \mathcal{A}(\mathbf{q}^N). \tag{2.8}$$

But, the catch is that both partition function and configurational integral, or even integral (2.8) are in general analytically unsolvable. Direct numerical methods such as Gaussian quadrature are also unfeasible, since the integration needs to be carried out over high number of degrees of freedom. Nonetheless, it is still possible to estimate the values of the above integrals using various integral equations, perturbation theories, mean field models or the methods of molecular dynamics (MD) and Monte Carlo (MC) [Tuc10, FS02, NKK02, Lea01].

2.2 Molecular dynamics and Monte Carlo

This section introduces the fundamental principles of Molecular dynamics and Monte Carlo – methods whose primary goal is to provide an estimate for integrals such as (2.8)*. We focus primarily on the core ideas behind the methods rather than their practical aspects, which will be discussed in the next chapter.*

Keywords: Monte Carlo (MC), Molecular dynamics (MD), ergodicity, sampling

The ultimate goal of MD and MC is to sample the space of microstates of the system and select a representative subset of microstates. Ensemble averages are then estimated as a sum over the subset, and therefore MD and MC should select the subset in such a way that its probability distribution converges to the exact one. Both methods solve the same problem, but by distinctive approaches.

2.2.1 Monte Carlo

Monte Carlo selects the subset using a random number generator, as we show on a specific example for canonical ensemble. In the most straightforward approach, one randomly generates positions of all particles obtaining a configuration included in the subset. The ensemble average (2.8) is then approximated by a finite sum over the set of generated states, $\{i\}$, as

$$\langle \mathcal{A} \rangle = \frac{1}{Z_N} \int \mathrm{d}\mathbf{q}^N \exp\left(-\beta \mathcal{U}(\mathbf{q}^N)\right) \mathcal{A}(\mathbf{q}^N) \approx \frac{1}{N_\mathrm{s}} \sum_i \mathcal{A}(i) \exp\left(-\beta \mathcal{U}(i)\right), \quad (2.9)$$

where N_s is the number of samples in the set. The introduced example of simple sampling includes all microstates with the same *a priori* probabilities, and only then re-weighs them with Boltzmann factors. However, this approach is very inefficient in dense systems or for big molecules, because by generating positions at random, it is almost inevitable to create a configuration containing overlaps between particles, resulting in a very small Boltzmann factor. The bottleneck is usually tackled by biasing the sampling scheme to preferentially include configurations which have high Boltzmann factors and contribute to the ensemble averages most significantly. A textbook example of how a biased sampling can be carried out is the Metropolis algorithm [MRR+53].

In the Metropolis algorithm, prior to including a configuration in the subset, two procedures are carried out. Firstly, a new trial configuration is generated from the last configuration using a specific MC move. Typical moves comprise operations such as random displacement or exchange of identities of particles.

Secondly, the trial configuration is either accepted to the subset, or rejected from it with the probability

$$\min\Big\{1, \exp\left(-\beta\Delta\mathcal{U}_{\mathrm{n,o}}\right)\Big\}, \tag{2.10}$$

where $\Delta\mathcal{U}_{\mathrm{n,o}}$ is the change of potential energy between the original configuration and the new one. If the trial configuration is rejected, the original configuration is accepted instead. By definition, Metropolis MC constitutes a Markov chain. An example of a possible implementation of Metropolis MC is given in Algorithm 1.

Algorithm 1: General Metropolis Monte Carlo scheme

```
while simulation is running do
    Load the last accepted configuration;
    Add a random displacement to the positions of all particles;
    Calculate ΔU_{n,o};
    if ΔU_{n,o} < 0 then
        Accept the trial configuration to the subset;
    else
        Calculate exp(−βΔU_{n,o});
        Generate a random number ω from uniform distribution in the
         interval (0, 1);
        if ω < exp(−βΔU_{n,o}) then
            Accept the trial configuration to the subset;
        else
            Accept the original configuration to the subset;
        end
    end
    Use the accepted configuration for analysis;
end
```

The scheme is general, however, a proper choice of a suitable and efficient MC move poses a great challenge for MC users. Lastly, similar MC procedures can be devised by modifying the acceptance criterion (2.10) to sample also other ensembles.

2.2.2 Molecular dynamics

In opposition to randomness, the method of MD use a deterministic prescription to generate the subset of representative configurations. In MD, one solves the classical equations of motion with an external force, $\mathbf{F}_i$

$$m_i\ddot{\mathbf{q}}_i = -\nabla\sum_{j=1}^{N} U(||\mathbf{q}_i - \mathbf{q}_j||) + \mathbf{F}_i, \tag{2.11}$$

for each particle; $U(||\mathbf{q}_i - \mathbf{q}_j||)$ is a pair interaction potential dependent on the distance between particles i and j.

The theoretical basis for the MD formalism stems from the ergodic theorem. Ergodic system is a system, where each microstate can be accessed from any other microstate in a finite number of steps. In an ergodic system, ensemble averages of quantities are equal to time averages collected over the MD trajectory, if the

time τ is long enough so that

$$\lim_{\tau\to\infty}\left(\frac{1}{\tau}\int_0^\tau \mathrm{d}t\mathcal{A}(t)\right) = \langle\mathcal{A}\rangle. \tag{2.12}$$

It can be shown that if $\mathbf{F}_i = 0$, the set of equations (2.11) generates configurations consistent with the probability distribution of microcanonical ensemble $[N, V, E]$. Equations (2.11) are solved only approximately using numerical integrators based on finite differences. An example of such a widely used integrator is the Velocity Verlet in Algorithm 2, in which we propagate the system in time by finite time-steps Δt, and v and x denote velocities and positions of particles respectively.

Algorithm 2: General Velocity Verlet scheme for molecular dynamics

```
while simulation is running do
    Update velocities at half-step v(t + Δt/2) := v(t) + a(t)Δt/2;
    Update positions at full step x(t + Δt) := x(t) + v(t + Δt/2)Δt/2;
    Use x(t + Δt) to calculate forces and accelerations a(t + Δt);
    Update velocities at full step
      v(t + Δt) := v(t + Δt/2) + a(t + Δt)Δt/2;
    Use the resulting configuration for analysis;
    Reset velocities v(t) := v(t + Δt);
    Reset positions x(t) := x(t + Δt);
end
```

The above mentioned schemes are valid for simulations in the microcanonical ensemble. Nonetheless, it is possible to sample also canonical ensemble. One example how to carry this out, is to include artifical degrees of freedom representing the thermostat.

2.2.3 Which one is to be used?

Finally, we compare MD and MC. Both methods are complementary, and converge to the same results, since they are just different engines for the same principles. One can perceive MD as a limiting case of MC, where the acceptance rate is unity by construction or, in different words, as a deterministic random process. However, MD and MC differ in efficiency which heavily depends on the system.

The biggest advantage of MD is that it uses one universal scheme for all systems. Carrying out an MD simulation is usually very straightforward, and facilitated by a broad availability of highly efficient software. On the other hand, each MC problem requires a specific scheme. Most importantly, an efficient MC move has to be devised, and implemented in the simulation code. This usually leads to a set of variable parameters which need to be tuned to acquire the optimal sampling. If tuned properly, MC may in some cases provide a speed-up of multiple orders of magnitude with respect to MD [UKL+14]. However, if not tuned properly, MC can easily become inefficient.

The biggest advantage of MC is that the generator of trial configurations may follow a non-physical evolution, which can potentially improve the sampling. For example, one can exchange identities of different particles in a trial move, and thus enhance sampling of configurations of systems with slow dynamics. MD, on the other hand, relies on a simulation of realistic evolution, and thus fails for systems with slow intrinsic dynamics, such as glasses, solids or big macromolecules.

From the above, it is clear that neither of methods is ultimately superior. The choice of the method should be always made with respect to the specificity of the system and the research question.

2.3 Measuring the free energy

Free energy is a state function essential for description of phase behaviour of matter, or spontaneity of chemical processes. Unfortunately, it is not possible to measure the free energy in a simulation directly, since such a measurement requires a direct evaluation of the partition function (2.14)*. In this section, we describe two simulation methods, specifically developed for measuring free energy differences between states of matter.*

Keywords: free energy, thermodynamic integration, Widom insertion

An advantage of both MD and MC is that they can estimate ensemble averages without the knowledge of the partition function, which can not be evaluated in general as can be demonstrated [NKK02] by rewriting the configuration integral as

$$Z_N = \frac{\int \mathrm{d}\mathbf{q}^N e^{-\beta\mathcal{U}}}{1} \equiv \frac{\int \mathrm{d}\mathbf{q}^N e^{-\beta\mathcal{U}}}{V^{-N}\int \mathrm{d}\mathbf{q}^N e^{-\beta\mathcal{U}} e^{+\beta\mathcal{U}}} = \frac{V^N}{\left\langle e^{+\beta\mathcal{U}}\right\rangle}. \tag{2.13}$$

By construction, direct MC and MD methods sample the configuration space mainly in regions where $e^{-\beta\mathcal{U}}$ is high, and thus $e^{+\beta\mathcal{U}}$ low. The simulation only rarely encounters states with high $e^{+\beta\mathcal{U}}$, therefore the estimator in the denominator of (2.13) can not be properly sampled directly. However, the free energy in canonical ensemble, $\mathcal{F}$, is defined as

$$\mathcal{F} = -k_\mathrm{B}T\ln(Q), \tag{2.14}$$

implying that if the configuration integral can not be evaluated directly, neither the partition function, nor the free energy can. We present two special methods that allow to circumvent the limitation imposed by biased sampling of MD and MC – Widom insertion and thermodynamic integration.

2.3.1 Widom insertion

Widom method [Wid63] is widely used to measure the chemical potential. The key idea of the method is to probe the chemical potential in the system of N particles by temporarily adding a virtual particle into the system, and measuring the concomitant change of the energy. This energy difference between the systems with and without the virtual particle can be interpreted as the work done by transferring the virtual particle from the vacuum to the system, and can be related to the free energy difference via the Jarzynski equality [Tuc10].

The underlying mathematical description follows the definition (1.14). For $N \gg 1$, we can approximate the chemical potential as the difference of free energies of systems with $N+1$ and N particles respectively as

$$\mu_i = \left(\frac{\partial\mathcal{F}}{\partial N_i}\right)_{V,T} \overset{N_i\to\infty}{\approx} \frac{\mathcal{F}(N_i+1)-\mathcal{F}(N_i-1)}{(N_i+1)-N_i} = -k_\mathrm{B}T\ln\left(\frac{Q(N_i+1)}{Q(N_i)}\right). \tag{2.15}$$

Next, if we explicitly express the above partition functions, we get

$$\mu_i = -k_\mathrm{B}T \ln \left(\frac{\int \mathbf{q}^{N_i+1} \int \mathbf{p}^{N_i+1} \exp(-\beta \mathcal{E}(\mathbf{q}^{N_i+1}, \mathbf{q}^{N_i+1}))}{\int \mathrm{d}\mathbf{p}_i^N \int \mathrm{d}\mathbf{q}_i^N \exp(-\beta \mathcal{E}(\mathbf{p}_i^N, \mathbf{q}_i^N))} \right), \tag{2.16}$$

and after integrating over momenta we arrive at the final result

$$\mu_i = \mu_i^{\mathrm{id.}} + \mu_i^{\mathrm{ex.}} = \mu_i^{\mathrm{id.}} - k_\mathrm{B}T \int \mathbf{q}_{N_i+1} \Big\langle \exp\left(\beta(\mathcal{U}_{N_i+1} - \mathcal{U}_{N_i})\right) \Big\rangle_{N_i}, \tag{2.17}$$

where $\langle \cdot \rangle_{N_i}$ denotes the ensemble average of a quantity in the ensemble of N particles.

The integration in (2.17) is carried out over all possible positions of the $(N+1)$st particle, virtually added into the system of N particles. It is crucial to realize that the integrand in (2.17), as an ensemble average, is also an integral, but carried out over positions of all N particles in the system.

A possible implementation of numerical integration of the integral (2.17) can be carried out using Algorithm 3.

Algorithm 3: General Widom insertion scheme

```
while simulation is running do
    Perform multiple steps of [N, V, T] sampling;
    Calculate U_{N_i};
    for a number of attempts do
        Add a particle to a random position in the system;
        Calculate and store exp(β(U_{N_i+1} − U_{N_i}));
        Remove the added particle from the system;
    end
end
Calculate the mean of the set of stored exp(β(U_{N_i+1} − U_{N_i}))
```

Widom insertion method is very efficient for measuring the chemical potential of small molecules in dilute systems [FS02]. However, insertion of a large particle into a dense system at a random position almost necessarily creates overlaps and causes a huge change in the energy of the system, biasing the calculation of the chemical potential. Nevertheless, measurement of free energy differences in dense systems can be carried out by other methods, such as thermodynamic integration.

2.3.2 Thermodynamic integration

Free energy is a state property, hence a difference of the free energy between two states can be measured along any path connecting these states. The choice of the path is completely arbitrary and it does not even have to follow an experimentally realizable route. Thermodynamic integration fully takes advantage of the latter, and measures the adiabatic work done along a specifically constructed virtual path [Kir35]. Let us assume we want to measure a difference of free energy between a state A and state B. We parametrize the potential energy of the system with a coupling parameter λ as

$$\mathcal{U}_\lambda(\mathbf{q}^N) = f(\lambda)\mathcal{U}_\mathrm{A}(\mathbf{q}^N) - g(\lambda)\mathcal{U}_\mathrm{B}(\mathbf{q}^N), \tag{2.18}$$

where f and g are arbitrary switching functions such that $f(0) = 1 \ \wedge \ g(0) = 0$ and $f(1) = 0 \ \wedge \ g(1) = 1$. Notably, $\mathcal{U}_{\lambda=0}(\mathbf{q}^N) = \mathcal{U}_\mathrm{A}(\mathbf{q}^N)$ corresponds to a pure

state A. Similarly, $\mathcal{U}_{\lambda=1}(\mathbf{q}^N) = \mathcal{U}_{\mathrm{B}}(\mathbf{q}^N)$ corresponds to a pure state B. Now, let us differentiate equation (2.14) with respect to the coupling parameter, obtaining

$$\frac{\partial \mathcal{F}}{\partial \lambda} = -\frac{k_{\mathrm{B}}T}{Q}\frac{\partial Q}{\partial \lambda} = -\Big\langle \frac{\partial \mathcal{U}(\mathbf{q}^N)}{\partial \lambda} \Big\rangle. \tag{2.19}$$

Next, by integrating (2.19) we obtain the final prescription for the free energy difference

$$\mathcal{F}_{\mathrm{A}} - \mathcal{F}_{\mathrm{B}} = \Delta\mathcal{F} = \int_0^1 \mathrm{d}\lambda \Big\langle \frac{\partial \mathcal{U}_\lambda(\mathbf{q}^N)}{\partial \lambda} \Big\rangle_\lambda. \tag{2.20}$$

Finally, we will illustrate a possible employment of the method in a simple case. Assume that the state A is a fully coupled fluid, and the state B an ideal gas with the same number of particles as the state A. Accordingly, the free energy difference between the states is equivalent to the excess free energy of the state A. The integration (2.20) comprises only one degree of freedom, and can be carried out by conventional numerical methods, such as trapezoidal rule, as long as the integral does not diverge. A possible divergence ought to be avoided by a proper choice of functions f and g. For simplicity, let us assume that $f(\lambda) = \lambda^2 \ \wedge \ g(\lambda) = 1 - \lambda^2$ are suitable. Additionally, $\mathcal{U}(\mathbf{q}^N)_{\mathrm{B}} = 0$ since the state B is an ideal gas. Lastly, by explicit differentiation of (2.18) we obtain $\partial \mathcal{U}_\lambda(\mathbf{q}^N)/\partial\lambda = 2\lambda \mathcal{U}_\lambda(\mathbf{q}^N)_{\mathrm{A}}$.

Now we just need to carry out a set of independent simulation runs using fixed λ values covering the whole interval $[0, 1]$. In each of these runs, we measure the quantity $\partial \mathcal{U}_\lambda(\mathbf{q}^N)/\partial\lambda$ for which we know the analytical form. We average this value over the whole simulation, obtaining the integrand of (2.20) as a function of the coupling parameter λ.

Thermodynamic integration is considered to be a versatile and robust, but very expensive method. The main pitfall of the method lies in a proper choice of reference states A and B, and functions f and g, such that (2.20) does not diverge, and the integration estimates the free energy with a high enough precision [Tuc10].

2.4 Simulating the chemical reaction equilibrium

Reacting systems are omnipresent in polymer research, and a method able to describe chemical equilibria in such systems is highly desirable. In contrast to canonical ensemble, where the number of particles is fixed, in this section, we introduce the framework of various ensembles which account for fluctuations in the number of particles due to chemical reactions in the studied system. Then, we focus on Monte Carlo methods allowing to sample chemical equilibrium.

Keywords: Monte Carlo, Reaction ensemble, Constant-pH ensemble

The key idea of simulating chemical reaction equilibria in macromolecular systems is to combine [LNR+19]: 1.) sampling of the conformational space while keeping the composition fixed and 2.) sampling of different compositions while keeping the conformation fixed. The former might be carried out be conventional methods of MD or MC, as long as the whole algorithm maintains detailed balance. This section focuses on the second type of sampling, which can be achieved by numerous methods of Monte Carlo. We will introduce three of them (see Figure 2.1) using a specific case of acid-base ionization equilibria, and give examples of their implementation for a simple reaction describing deprotonation of a weak acid

$$\mathrm{HA} \rightleftharpoons \mathrm{A}^- + \mathrm{H}^+. \tag{2.21}$$

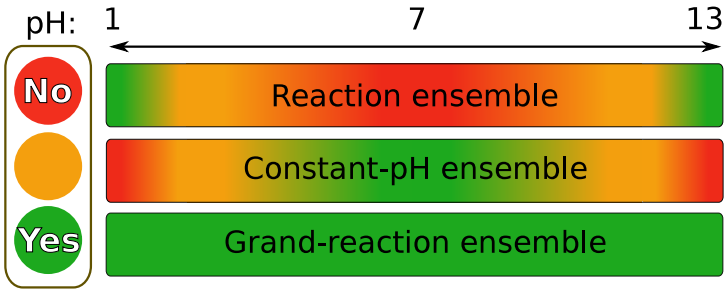

Figure 2.1: Schematic infographics of safe applicability of the introduced methods. The figure was considered for a graphical abstract for Ref. [LHR+20] but was not used finally. Author: Oleg Rud

2.4.1 Constant-pH ensemble

The framework of Constant-pH ensemble allows to impose a fixed pH value in the system, and sample ionization states consistent with this pH [RR92]. Theoretically, the method is equivalent to coupling the system to an infinite reservoir of H^+ and OH^- ions by a membrane penetrable only to these two ions. Experimental realization of Constant-pH simulation is the addition of a high-capacity buffer to the solution. Algorithm 4 summarizes the steps for a creation of a trial configuration in a Constant-pH simulation to be accepted or rejected with the acceptance criterion

$$P_{\mathrm{n,o}}^{\mathrm{cpH}} = \min\Big\{1, \exp(-\beta\Delta\mathcal{U}_{\mathrm{n,o}} + \xi(\mathrm{pH} - \mathrm{p}K_{\mathrm{A}})\ln(10)\Big\}, \tag{2.22}$$

where $\xi = \pm 1$ is the extent of the ionization reaction.

Algorithm 4: General scheme for MC in the Constant-pH ensemble

```
while simulation is running do
    Randomly choose to preform reaction or configuration move with a
     fixed probability;
    if configuration move then
        perform multiple steps of [N, V, T] sampling
    else
        Randomly choose either forward direction with probability
         proportional to the number of HA or backward direction with
         probability proportional to the number of A⁻;
        if forward direction then
            change the identity of a random HA to A⁻, and insert a H⁺ to
             a random position to generate a trial configuration
        else
            change the identity of a random A⁻ to HA, and remove a
             random H⁺ to generate a trial configuration
        end
        Accept or reject the trial configuration with the criterion (2.22)
    end
end
```

The input of the method is pH in the system and concentration of ionizable species with a given $\mathrm{p}K_\mathrm{A}$. The output is the degree of ionization and ensemble averages of observables at the given pH and system composition [LNR$^+$19].

It is important to realize that input pH enters the calculation only in the criterion (2.22), and thus is imposed only indirectly. Therefore, H^+ ions generated in the box by the ionization reaction are just a product of preserving the electroneutrality. Using (1.18), the pH value calculated from the average number of H^+ ions in the box does not necessarily correspond to the pH set as the input because the number of H^+ is limited by the number of reactive species. This could result in artifacts, especially, if the real concentration of H^+ corresponding to the input pH is higher than the one given by the number of ions. Lack of explicit H^+ ions at pH $\lesssim 3$ results in underestimation of electrostatic screening effects, except the cases where the ionic strength, I, is dominated by background salt. The latter claim can be generalized also for OH^-, implying the range of the safe applicability of Constant-pH method: solutions at $3 \lesssim \mathrm{pH} \lesssim 11$. If one wishes to simulate in the complementary range of pH, the number of ions to match the ionic strength at a given pH should be high enough so that $\mathrm{p}I \lesssim \min\{\mathrm{pH}, \mathrm{pOH}\}$ [LHS17, LNR$^+$19].

2.4.2 Reaction ensemble

The method of Reaction ensemble allows to sample equilibrium composition in a closed system in which a set of reactions occurs [ST94, JPG94, TBL$^+$08]. The inputs of the method are equilibrium constants of respective chemical reactions and initial composition of the reacting system. The output is the equilibrium composition of the system, in contrast to the Constant-pH method which is only applicable to dissociation reaction of a type $\mathrm{AB} \rightleftharpoons \mathrm{A} + \mathrm{B}$, and only yields

the equilibrium degree of dissociation of AB. Experimental realization of the Reaction ensemble method is to mix the reactive species in a closed container, and measure concentrations after the chemical equilibrium is reached. The Reaction ensemble protocol (see Algorithm 5) is very similar to the Constant-pH one (see Algorithm 4) and differs mainly in technicalities. The trial configuration is accepted using the following criterion

$$P_{\mathrm{n,o}}^{\mathrm{RxMC}} = \min\Big\{1, (V^{\bar{\nu}}\Gamma)^{\xi} \prod_i \Big[\frac{N_i^0!}{(N_i^0 + \nu_i\xi)!}\Big] \exp(-\beta\Delta\mathcal{U}_{\mathrm{n,o}})\Big\}, \tag{2.23}$$

where ν_i is the stoichiometric coefficient of product or reactant i with the initial number of species N_i^0, Γ is the equilibrium constant, and $\bar{\nu} = \sum_i \nu_i$, .

Algorithm 5: General scheme for MC in the Reaction ensemble

```
while simulation is running do
    Randomly choose to preform reaction or configuration move with a
     fixed probability;
    if configuration move then
        perform multiple steps of [N, V, T] sampling
    else
        Randomly choose a reaction from the set of occurring reactions
         with equal probabilities;
        Randomly choose a direction of the reaction with equal
         probabilities;
        if forward direction then
            change the identity of a random HA to A^-, and insert a H^+ to
             a random position to generate a trial configuration
        else
            change the identity of a random A^- to HA, and remove a
             random H^+ to generate a trial configuration
        end
        Accept or reject the trial configuration with the criterion (2.23)
    end
end
```

In the Reaction ensemble method, pH of the system is directly coupled to the number of H^+ species, and has to be calculated from the equilibrium composition, as opposed to the Constant-pH method where pH is the input. However, this brings complications in systems where the average number of H^+ or OH^- in the simulation is low – in practice it becomes particularly significant if the number is on the order of unity. This results in strong finite-size effects and uncertainity in the calculation of pH, which outlimits the range of safe applicability. The Reaction ensemble works well at pH $\lesssim$ 4 and pH $\gtrsim$ 10, which is almost complementary to the Constant-pH method.

We will conclude by underlining some differences between the two presented methods regarding dilution effects and titration curves. In the Constant-pH method, if one increases the volume of simulation cell, keeping the number of species constant, the imposed pH remains the same and thus this apparent dilution is in fact equivalent to the addition of extra buffer at the same pH. On the other hand, in the Reaction ensemble method, increasing the volume is equivalent to adding pure solvent [LHS17].

Next, if one wishes to construct titration curves $\alpha(\mathrm{pH})$ using the Constant-pH method, a series of independent simulations with varying input pH is carried out. Degree of ionization as a function of pH is the direct output. In the Reaction ensemble, one carries out multiple independent simulations with varying equilibrium constant Γ (acidity constant), and obtains the degree of ionization and pH as output. Variation of Γ might seem difficult to realize in experiments. However, it turns out the relevant parameter which determines the ionization is only the difference $\mathrm{pH} - \mathrm{p}K_\mathrm{A}$ as long as $\mathrm{p}I \lesssim \min\{\mathrm{pH}, \mathrm{pOH}\}$. Therefore, in most practical situations it does not matter whether the pH or the $\mathrm{p}K_\mathrm{A}$ is varied as input parameter [LNR+19].

2.4.3 Grand-reaction ensemble

The Constant-pH ensemble method and the Reaction ensemble method provide complementary tools to simulate the ionization equilibrium in a closed system. However, one often wishes to model a system which is open, and exchanges species with a reservoir – for example when dealing with polyelectrolyte gels or complex coacervates. In such cases, the partitioning of charged species is subjected to the Donnan equilibrium, which is coupled to ionization equilibrium in the system in a complex feedback loop. This is hardly captured by the Constant-pH method, since the pH of the system is fixed as input, and the link to the pH of the reservoir is not straightforward. In contrast, in the Reaction ensemble method it is possible to couple a reservoir to the system, but only in a limited range of pH because of small numbers of reactive species at intermediate values of pH. Presumably, the only method allowing to couple a system to a reservoir at arbitrary salt concentration and pH is the recently developed Grand-reaction method [LHR+20].

We will present the simulation protocol of Grand-reaction method using a specific example of a reservoir containing $\mathrm{Na}^+, \mathrm{Cl}^-, \mathrm{H}^+$ and OH^- ions coupled to the system containing the same ions and a polyelectrolyte HA/A^- which can not leave the system, but can undergo ionization reaction (2.21). The Grand-reaction method expands the Reaction ensemble method by a specific construction of the set of occurring reactions, and reformulation of the probability criterion (2.23) to

$$P_\mathrm{n,o}^\mathrm{GRxMC} = \min\left\{1, \left(\prod_i \left[\frac{N_i^0! V c^\ominus}{(N_i^0 + \nu_i\xi)!}\right]^{\nu_i\xi}\right) \exp\left(\beta\left[\xi\sum_i \nu_i(\mu_i - \mu_i^\ominus) - \Delta\mathcal{U}_\mathrm{n,o}\right]\right)\right\}, \tag{2.24}$$

where $c^\ominus = 1$ mol/L is the concentration of an ideal gas at the reference state.

First, the ion exchange with the reservoir in the system is emulated by virtual annihilation and creation reactions

$$\begin{aligned}
\emptyset &\rightleftharpoons \mathrm{Na}^+ + \mathrm{Cl}^-, && K_{\{\mathrm{Na}^+,\mathrm{Cl}^-\}},\\
\emptyset &\rightleftharpoons \mathrm{H}^+ + \mathrm{Cl}^-, && K_{\{\mathrm{H}^+,\mathrm{Cl}^-\}},\\
\emptyset &\rightleftharpoons \mathrm{Na}^+ + \mathrm{OH}^-, && K_{\{\mathrm{Na}^+,\mathrm{OH}^-\}},\\
\emptyset &\rightleftharpoons \mathrm{H}^+ + \mathrm{OH}^-, && K_{\{\mathrm{H}^+,\mathrm{OH}^-\}},
\end{aligned} \tag{2.25}$$

where $K_{\{i,j\}}$ is a formal equilibrium constant defined as $k_\mathrm{B}T\ln K_{\{i,j\}} = (\mu_i - \mu_i^\ominus) + (\mu_j - \mu_j^\ominus)$, following the notation of Section 1.4. We will treat constants

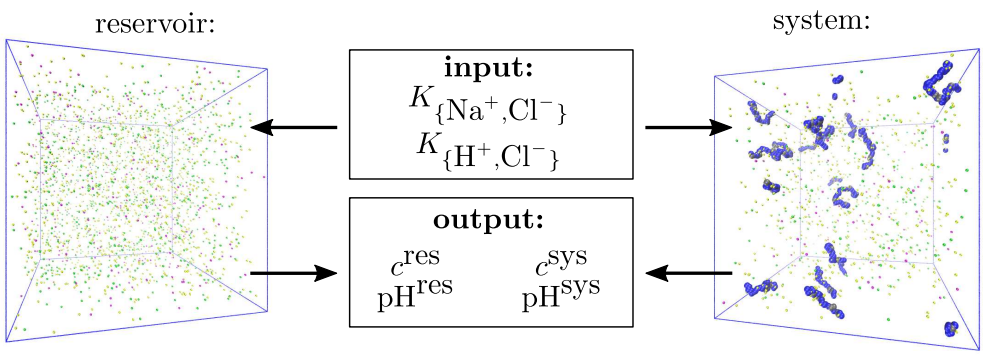

Figure 2.2: Schematic workflow of carrying out a Grand-reaction simulation of a system of weak polyacid chains with defined pK_A coupled to a reservoir composed of Na^+, Cl^-, H^+ and OH^-.

$K_{\{Na^+,Cl^-\}}$ and $K_{\{H^+,Cl^-\}}$ as the input. $K_{\{H^+,OH^-\}} \equiv K_w$ as the ionic product of water is a tabulated thermodynamic constant and

$$K_{\{Na^+,OH^-\}} = \frac{K_{\{Na^+,Cl^-\}} K_{\{H^+,OH^-\}}}{K_{\{H^+,Cl^-\}}}, \tag{2.26}$$

is ultimately defined by the three other equilibrium constants in (2.25). One can perceive this coupling to a reservoir as an alternative to grand-canonical ensemble, where instead of specifying absolute values of chemical potentials of species, we specify their linear combinations in forms of formal equilibrium constants.

Secondly, ionization equilibrium in the system is described by the equation (2.21), where the acidity constant K_A is the input, and is a tabulated thermodynamic constant for a given monomer chemical identity. The bottleneck of Reaction ensemble method resides in the fact that at $4 \lesssim pH \lesssim 10$, the number of reactive species H^+ and OH^- is very low. To avoid this limitation, we reformulate the ionization reaction (2.21) using the coupling to reservoir (2.25) as

$$\begin{aligned} HA + OH^- &\rightleftharpoons A^-, & K'_A, \\ HA &\rightleftharpoons A^- + Na^+, & K''_A, \\ HA + Cl^- &\rightleftharpoons A^-, & K'''_A, \end{aligned} \tag{2.27}$$

where the three constants are ultimately defined by $K_{\{Na^+,Cl^-\}}$ and $K_{\{Na^+,Cl^-\}}$ from (2.21) as

$$\begin{aligned} k_B T \ln K'_A &= -\mu^{\ominus}_{A^-} - \mu^{\ominus}_{H^+} + \mu^{\ominus}_{HA} - k_B T \ln K_w && = \frac{K_A}{K_w}, \\ k_B T \ln K''_A &= -\mu^{\ominus}_{A^-} + \mu^{\ominus}_{HA} + \mu_{Na^+} - \mu^{\ominus}_{Na^+} - \mu_{H^+} && = \frac{K_A K_{\{Na^+,Cl^-\}}}{K_{\{H^+,Cl^-\}}}, \\ k_B T \ln K'''_A &= -\mu^{\ominus}_{A^-} + \mu^{\ominus}_{HA} - \mu_{H^+} + \mu^{\ominus}_{Na^+} - \mu_{Cl^-} && = \frac{K_A}{K_{\{H^+,Cl^-\}}}. \end{aligned} \tag{2.28}$$

The reactions in (2.27) are a results of adding up the ionization reaction (2.21) with the reactions (2.25) respectively. Such a reformulation embodies the spirit

of Monte Carlo methods – reactions in (2.27) do not follow a physical evolution, however still correctly sample equilibrium.

Finally, we describe how simulations of a system coupled to a reservoir can be carried out using the Grand-reaction method. First, we choose $K_{\{Na^+,Cl^-\}}$ and $K_{\{H^+,Cl^-\}}$ and run a simulation of a reservoir using the Reaction ensemble Algorithm 5, but with criterion (2.24) and set of reactions (2.25). The result of such a simulation is the composition of the reservoir, and ensemble averages of observables such as osmotic pressure of the reservoir. Simulations of reservoir are in general inexpensive when compared to simulations of polyelectrolytes, and by carrying out a series of such simulations for different inputs, we can iteratively map the input equilibrium constants to a reservoir composition and pH.

Secondly, we carry out the simulations of the system using Algorithm 5 with the criterion (2.24), and set of reactions (2.25) and (2.27), while using the same input equilibrium constants $K_{\{Na^+,Cl^-\}}$ and $K_{\{H^+,Cl^-\}}$ as in the case of reservoir. The output of such a simulation is the composition of the system, and ensemble averages of observables at this composition. The scheme of the method is depicted in Figure 2.2.

3. Simulation models

Prior to employing a specific simulation method, a model of a system is needed. A model is a simplified depiction of the reality, which should capture the essence of the studied system. In the following chapter, we introduce standard models used when simulating polyelectrolytes.

3.1 Coarse-grained model of a polymer

In Chapter 2, we intentionally formulated most of the concepts in rather generic terms such as 'particle' which could stand for an atom, a group of atoms, or even a molecule. Here we clarify, what precisely we mean by 'particle' and so on, in the context of polymers. This section is committed mainly to representation of chemical species, and practical subtleties of methods emerging as a consequence of using a specific model.

Keywords: Langevin dynamics, Grest-Kremer chain, implicit solvent

Arguably, most popular simulation models among chemists are those with atomistic resolution. In such models, an atom is the smallest constituent of the system, and is represented by a point particle. Atoms interact through interaction potentials based on simple physical models such as harmonic spring to account for a chemical bond, or Coulombic interaction to account for charge-charge interactions. Chemical identities of modeled particles are attained by the proper choice of interaction constants and parameters such as partial charges. Such a choice is often based either on quantum-chemical calculations, or based on fitting a specific experiment. In either case, however, construction of the set of potentials and parameters is a non-trivial procedure, and presents one of the greatest contemporary challenges to molecular simulations.

Although atomistic models in general have a high accuracy, their employment is limited to rather small systems. In general, the computational cost of molecular simulations increases with the number of particles in the system. In contemporary practice, a typical system size ranges from 10^2 to 10^9 particles [NKK02] enclosed in a simulation box. To diminish the surface effects, the box is usually enveloped by its own periodic images on its boundaries. Additionally, modern computers allow to carry out up to 10^{12} integration steps or MC trials in a reasonable time. It might be feasible to carry out an atomistic simulation of a protein, which typically possesses a folded structure. In comparison to rather rigid proteins, flexible synthetic macromolecules occupy a much bigger proportion of the configurational space, which needs to be sampled accordingly. Additionally, synthetic macromolecules often evolve on a characteristic time scale on the order of miliseconds or seconds. The latter, in combination with the number of atoms in a typical macromolecular system, makes a direct application of atomistic MD to synthetic macromolecules unfeasible. In such cases, a simpler model with a smaller number of degrees of freedom should be used.

One possible way to reduce the number of degrees of freedom is to use coarse-grained models. As opposed to atomistic models, a particle in a coarse-grained model represents a whole molecule or a group of atoms such as one monomeric

unit of the polymer chain. Coarse-graining reduces the dimensionality of the configurational space, allowing to sample it properly. The price to be paid is the loss of resolution, and often also the chemical specificity. Nonetheless, coarse-grained models are still able to capture various physical aspects of studied systems. Additionally, a lot of effort has been recently invested in the development of systematic coarse-graining procedures starting from atomistic models, to make up for the loss of resolution [BD09].

Another possible way to reduce the number of particles is to use an implicit solvent. In dilute solutions, the solvent occupies majority of the volume of the studied systems, yet it often plays a role at which it can be approximated as a structureless continuum. For example, interactions and collisions of particles with solvent can be emulated by modifying the simulation methods. For instance, in Langevin dynamics in canonical ensemble, one solves equation (2.11) where the external force $\mathbf{F}_i$ is

$$\mathbf{F}_i = -\gamma \dot{\mathbf{q}}_i + \sqrt{2\gamma k_\mathrm{B} T} \cdot \mathcal{R}(t), \tag{3.1}$$

$$\langle \mathcal{R}(t) \cdot \mathcal{R}(t') \rangle = \delta(t - t'), \tag{3.2}$$

$$\langle \mathcal{R}(t) \rangle = 0, \tag{3.3}$$

where γ is the damping constant related to solvent viscosity, and δ is the Dirac delta function. The first term in (3.1) is a dissipative force and the second a random force obeying (3.2) and (3.3), representing collisions with the solvent. An important feature of the Langevin dynamics is that its use by construction provides a thermostat, and samples the canonical ensemble.

Finally, we combine both coarse-graining of a full polymer chain to a chain of monomers, and employment of Langevin equation in implicit solvent. Such a combination of the two simplification is a generalization of commonly used Grest-Kremer model [GK86], and is the model used in all of the simulation in this thesis.

3.2 Interaction potentials

An appropriate description of interactions between particles is essential to calculate thermodynamic properties of the system. Interaction potentials in coarse-grained modelling of polyelectrolytes are usually pairwise, and have a closed functional form, based on simple physical models. In this section, we list interaction potentials used in models in this thesis.

Keywords: Lennard-Jones, Ewald summation, $\mathrm{P^3M}$, FENE bond

Firstly, we introduce potentials representing non-bonding interactions between particles. Inherently, coarse-grained models are not able to fully capture the complex nature of Van der Waals interactions or induced polarization. Potentials of this type are often generic, possessing only qualitative features of Van der Waals interactions, such as repulsive character at short distances, and medium-range attraction. A popular generic model describing such interactions is the Lennard-Jones potential

$$U_\mathrm{LJ}(r) = 4\varepsilon \left(\left(\frac{\sigma}{r} \right)^{12} - \left(\frac{\sigma}{r} \right)^{6} \right), \tag{3.4}$$

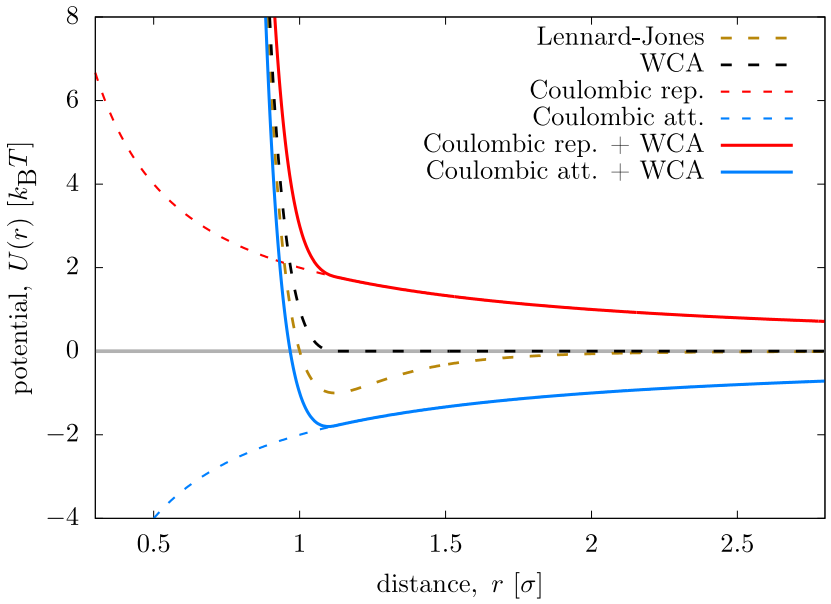

Figure 3.1: Selected non-bonding pairwise interaction potentials as a function of distance. Parameters used: Lennard-Jones: $\varepsilon = 1\ k_\mathrm{B}T, \sigma = 1, r_\mathrm{c} = 2.5\sigma$; WCA: $\varepsilon = 1\ k_\mathrm{B}T$; Coulomb repulsive: $l_\mathrm{B} = 2\sigma, z_i z_j = 1$; Coulomb attractive: $l_\mathrm{B} = 2\sigma, z_i z_j = -1$; Solid lines show total potentials between a pair of charged particles with excluded volume represented by WCA.

where ε is the depth of the potential well. For practical purposes, we often choose a cut-off distance r_c, and set the potential energy between two particles in the distance $r > r_\mathrm{c}$ to zero. However, setting the potential to zero in distances $r > r_\mathrm{c}$ causes a discontinuity in potential, and thus undefined force at $r = r_\mathrm{c}$. To circumvent this issue, potentials with cut-off are usually shifted with respect to the value at the cut-off distance to maintain continuity, resulting in the formula

$$U_\mathrm{LJ}(r) = \begin{cases} 4\varepsilon\left(\left(\frac{\sigma}{r}\right)^{12} - \left(\frac{\sigma}{r}\right)^{6} - \left(\frac{\sigma}{r_\mathrm{c}}\right)^{12} + \left(\frac{\sigma}{r_\mathrm{c}}\right)^{6}\right), & \text{if } 0 < r \leq r_\mathrm{c} \\ 0, & \text{if } r_\mathrm{c} < r < \infty. \end{cases} \tag{3.5}$$

Such a truncated and shifted version of Lennard-Jones potential is depicted in Figure 3.1.

One often wants to have a purely repulsive interaction between particles, for example when dealing with polymer chains in a good solvent. Common choice for such a potential is the Weeks-Chandler-Andersen (WCA) potential, equivalent to the Lennard-Jones potential with a cut-off $r_\mathrm{c} = 2^{1/6}\sigma \approx 1.12\sigma$ coinciding with the minimum of Lennard-Jones potential well. A shifted version of the WCA potential is also plotted in Figure 3.1 for a reference.

The Lennard-Jones and WCA potentials were originally designed to model noble gases, and the use of the potentials in coarse-grained simulations is mainly due to numerical convenience. However, interactions between coarse-grained particles, such as colloids or monomeric units, are often softer – they possess a less steep divergence at small distances as compared to the Lennard-Jones [WRHDF20]. For this reason, the Lennard-Jones potential can be generalized by replacing the scaling exponents in (3.4) as $\{12, 6\} \mapsto \{\nu_1, \nu_2\}$. It turns out [WRHDF20] that

choices $\{8, 4\}$ or $\{4, 2\}$ for the exponents are often more suitable representations of interactions between particles of soft matter.

A special care is required when dealing with electrostatic interactions, fundamentally described by Coulomb's law. Coulomb potential decays only very slowly, as is observable in Figure 3.1. Because of the long-range nature of Coulomb potential, also interactions of a particle with its own periodic images in the periodic boundary conditions have to be considered. Additionally, it can be shown that it is not possible to use cut-off in calculations [NKK02], because it leads to systematic errors. Consequently, one is presented with a challenge of evaluating a conditionally convergent sum

$$\mathcal{U}_{\text{el.}} = \frac{k_{\text{B}}T}{2} l_{\text{B}} \sum_{i,j} \sum_{\vec{n}\in\mathbb{Z}^3}^{*} \frac{z_i z_j}{||\vec{r}_i - \vec{r}_j + \vec{n}L||}, \tag{3.6}$$

where the first sum regards all pairs of charged particles i, j in the simulation box, and the second sum account for all their periodic images. Asterisk in the second sum means that for $\vec{n} = 0$, the terms with $i = j$ are omitted to avoid singularity, as the distance of such a pair is zero. The first solution to the summation (3.6) was proposed by Paul Peter Ewald [Ewa21]. The key idea is to rewrite the $1/r$ term as a sum of two rapidly convergent functions – one short-ranged and evaluated in real space, the other one long-ranged and evaluated in Fourier space [HKDL01, HE89]. The resulting sums can be truncated in their respective spaces and evaluated explicitly. Nevertheless, direct implementation of the Ewald summation in a space of continuous coordinates is computationally expensive. A significant speed-up can be achieved by using particle-particle particle-mesh method (P^3M) [HE89, DH98]. The method uses a finite discrete grid, on which the charges are interpolated as charge densities, allowing to employ highly efficient numerical algorithms of Fast Fourier Transform.

Although the Coulomb potential is exact, the use of the Coulomb interaction in implicit solvent has a few subtle assumptions, making the Coulomb interaction exact only in principle. For example, implicit solvent is usually modelled as a homogeneous continuum described by a single dielectric constant. However, dielectric constant is a local quantity, which depends on the distribution of charged objects in the system. For example, ions locally reduce the permittivity of the solvent in their vicinity, because solvent dipoles align with the local electric field of the ion rather than the external field. Such a change of permittivity becomes especially important for charges separated by a distance comparable to a size of the solvent molecule – for aqueous solutions on the order of $r \sim 0.1$ nm. Inclusion of permittivity gradients is important for example, when modelling electrokinetic phenomena such as electrophoresis by means of coarse-grained simulations [FHSH15].

In contrast to non-bonding interactions, which act between any two particles of a given type, bonding interactions connect a specific pair of particles. Presumably the simplest model describing a bond is a harmonic potential

$$U_{\text{harm}}(r) = \frac{1}{2} k (r - r_0)^2, \tag{3.7}$$

defined by the stiffness constant k and equilibrium bond length r_0, plotted in Figure 3.1. However, the Hooke's law as an underlying assumption of harmonic

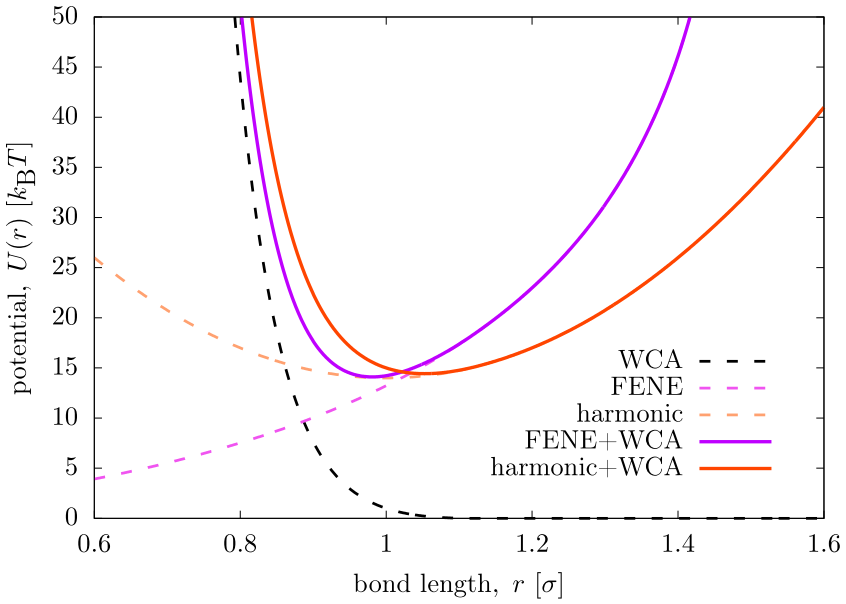

Figure 3.2: Selected bonding pairwise interaction potentials as a function of distance. FENE: $\Delta r_{\max} = 1.5\sigma$, $r_0 = 0$, $k = 30k_\mathrm{B}T/\sigma^2$; Harmonic: $k = 100k_\mathrm{B}T/\sigma^2$, $r_0 = 1\sigma$. Solid lines show total potentials between a pair of bonded particles with excluded volume represented by WCA. Harmonic potential is shifted by a constant, so the minimum of its potential well coincides with the minimum of the FENE + WCA potential.

potential is a valid approximation only at small bond extensions [RC03]. To avoid this limitation, one usually uses anharmonic finite extension nonlinear elastic (FENE) bonding potential

$$U_{\mathrm{FENE}}(r) = -\frac{1}{2}k\Delta r_{\max}^2 \ln\left(1 - \left(\frac{r - r_0}{\Delta r_{\max}}\right)^2\right), \tag{3.8}$$

where r_0 is the equilibrium bond length, and $r_0 + \Delta r_{\max.}$ is the maximum possible bond length at which the potential diverges.

We conclude by emphasizing that with a possible exception of Coulomb potential, the above mentioned potentials are just generic models. Therefore, the choice of a specific interaction potential and force constants for excluded-volume interactions and bonding interactions is often somewhat arbitrary in coarse-grained models, as long as the potentials possess the same qualitative features. Any generic potential is neither better not worse than any other generic potential, and universal properties of macromolecular systems should remain the same regardless of the choice of force field. For example, the average size of a neutral polymer chain of length N in a good solvent should obey a scaling relation

$$\langle \vec{R_{ee}} \cdot \vec{R_{ee}} \rangle \sim N^{3/5}. \tag{3.9}$$

Such a universal property should be a result of a coarse-grained simulations for any choice of bonding potentials and repulsive non-bonding interactions above.

4. Results

In the following chapter, we present our results in a top-down fashion. We introduce our novel method for simulations of phase equilibrium and ion partitioning in complex coacervates. We characterize the key physical principles governing the exchange of solutes between the phase of coacervate and co-existing reservoir. Afterwards, the nature of involved effects is refined in a greater detail in simpler systems of dilute solutions of polyelectrolytes. Finally, we combine the investigated elementary principles to describe yet another complicated system of a reversible electrostatically cross-linked gel, and make a prediction for experiments done in parallel to our theoretical work.

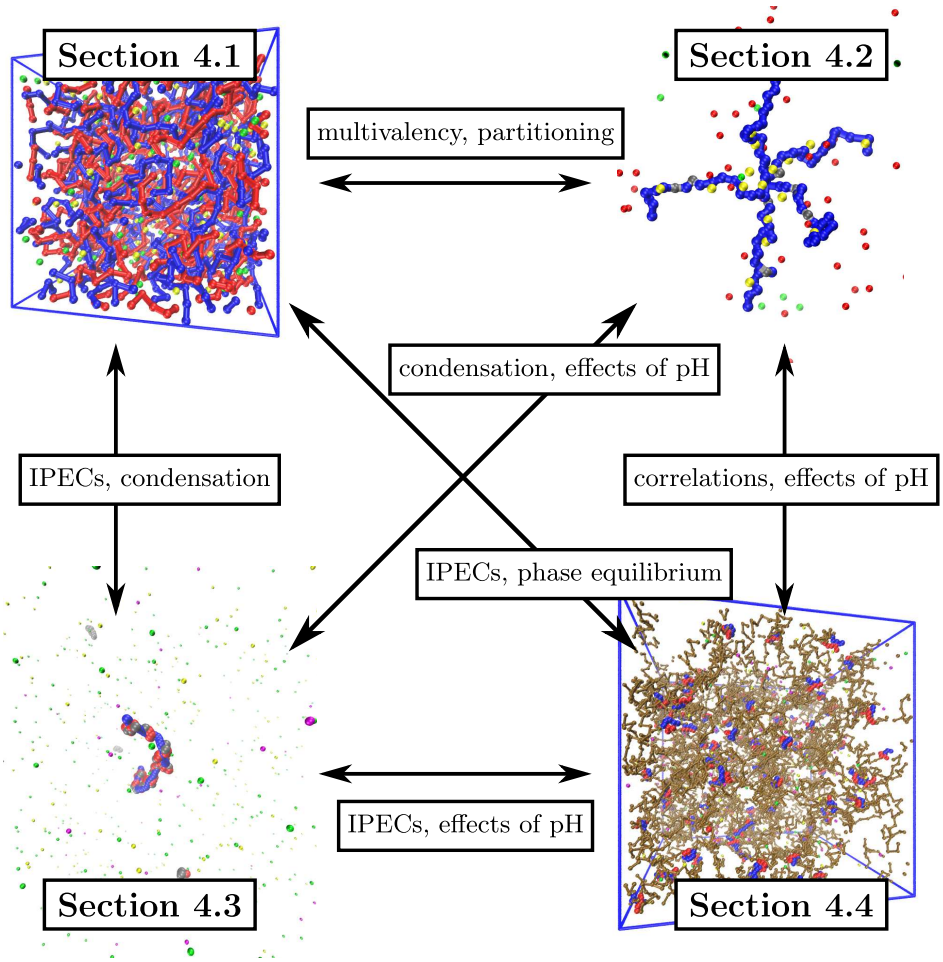

Figure 4.1: A schematic representation of how our case studies relate to each other, and keywords that unify them.

4.1 Coacervate as a scavenger of small ions

In this section we present our newly developed model and method for simulations of partitioning and phase equilibrium in coacervates. We validate our model by comparison with accepted theories and experiments, and then use it to investigate the stability of non-stoichiometric coacervates. Next, we quantify the thermodynamic aspects of partitioning of univalent and divalent ions between the polymer-poor and polymer-rich phase. We explain the observed effects within the framework of the Donnan theory, but accounting for the contribution of interparticle interactions.

4.1.1 Introduction

Complex coacervates are abundant in living systems, for example in the form of DNA-histone complexes or ribonucleoproteins. Charge-driven liquid-liquid phase separation is one of the main mechanisms of intracellular compartmentalization and structural regulation [FA18]. For instance, cells utilize coacervation to create microenvironments comprising membraneless organelles, which can selectively partition specific biomacromolecules between the phase of coacervate and cytosol. Even though the function of coacervate membraneless organelles is not completely understood, their existence inspired the development of new classes of materials, promising for peptide therapy [vLCL19, Bra13].

Peptide therapeutics directly injected to the body are easily denatured or degraded by enzymes, which scales down the functionality of the peptides. However, peptides as polyelectrolytes might be incorporated into a complex coacervate, mitigating the degrading effects of proteases in the living systems. Furthermore, phase stability and properties of coacervates depend on the environment, enabling to use coacervates as therapeutics carriers for peptide drug delivery or targeted sequestration [BPP$^+$14, Bro05].

Indeed, there is a number of experimental studies presenting coacervate systems for uptake and release of peptides, usually controlled by the change of pH [vLCL19]. In some of the cases, the peptides preserved secondary structure upon the release, which is often a prerequisite for their biological function [BPP$^+$14, ZZ18]. Furthermore, some experiments were successful in a controlled selective partitioning of a specific peptide from the mixture of peptides [vLCL19]. Although these results are impressive, the fundamental understanding governing the uptake is not sufficiently understood. Most studies are done in *ad hoc* systems, and explanations of the observed effects are based only on intuitive arguments, such as the Donnan theory – preferential partitioning of peptides with a net positive charge by a coacervate with a net negative charge [vLCL19, LC16, LdVS$^+$09]. Besides the net charge on the peptide, also charge distribution and patchiness or hydrogen bonds, are important in some cases [DDHS14], further complicating understanding of the involved mechanisms. Evidently, a dearth of fundamental understanding of peptide uptake is impeding the rational design of coacervates materials.

Unfortunately, partitioning of solutes between coacervates and co-existing solutions is not completely comprehended not even for simple solutes such as monovalent ions, not to mention complex peptides. Presumably, the understanding of

partitioning of these simpler solutes, is essential for the bottom-up description of more complex solutes. Complex coacervates were extensively investigated in recent years, however the experimental data on salt content of coacervate are rather limited [SYDW19, WS14, PS15, LSA$^+$18]. Furthermore, some experiments are affected by ion specific effects [PLP$^+$14] or by chemistry of the polymers [PLH$^+$15, HPL$^+$15], making it hard to separate generic and specific effects.

To explore the underlying physical principles of ion partitioning, a number of theoretical studies has been conducted [Sin17, Mut17]. However, development of reliable analytical theories for highly-correlated coacervates is still in the early stages. For example, the established Voorn-Overbeek theory, widely used to fit experimental phase diagrams, predicts preferential partitioning of uni-univalent salt into the polymer-rich phase, while experiments show a preference of the polymer-poor phase [OV57, MOV57, SP20]. More sophisticated theories based on liquid-states equations, such as PRISM [PS15], were able to capture the above mentioned partitioning in agreement with experiments, however different theories ascribe this result to different effects, such as excluded volume interactions, inter-particle correlations or polymer connectivity, while their interplay is still not completely understood [ZSAW18, PS15, LS17]. Furthermore, only very few theoretical studies dealt with non-stoichiometric complexes [ZAWW18], which is surprising, considering the importance of charge asymmetry in the applications of bioencapsulation [vLCL19]. The same holds for the effects of pH or multivalent ions which have been investigated only marginally [LS17], in spite of use of coacervates for extraction of multivalent dyes and metal ions from the solutions [VJFZ19, MNW15, PT12].

Supposedly, molecular simulations should be useful in addressing the problem of partitioning, because they directly account for the delicate interplay of the above mentioned effects, and in principle provide a numerically exact solution for a given model. However, particle-based simulations of complex coacervates are very scarce. There are few studies regarding association of a single polycation with a single polyanion in dilute solutions [RSSW18, RZS$^+$18, OM06], but it is not completely clear how results of such simulations relate to the behaviour of a bulk phase of coacervates. One might capture some features of coacervate behaviour by adding more polyions to the dilute solutions, however such studies usually lead to a quasi-phase separation within a simulation box [SGKOdlC20]. One thus simulates a dense globular nano-droplets of an interpolyelectrolyte complex floating in otherwise almost empty simulation box. Results of such simulations provide insights into the formation of interpolyelectrolyte complexes, however they are heavily affected by finite-size effects, and the extrapolation to the macroscopic phase behaviour should be made with extreme caution.

To our knowledge, there are only two research groups whose simulation protocols have been remarkably successful in the description of macroscopic phase behaviour of coacervates. The group of Charles Sing used hybrid calculations involving both Monte Carlo simulations and subsequent simulation-informed analytical Transfer matrix and liquid-state theories [Lyt19]. Their studies were able to match related experiments almost quantitatively [LS17, LCM$^+$19, LRS16, CLR$^+$17], however molecular simulations plays only a partial role in the calculations. Furthermore, their approacher, such as PRISM theory [PS15], depend on used closures, and various assumption which are difficult to prove [Sin17]. To our

knowledge, the studies of Andreev *et. al.* [APD$^+$18] and Li *et. al.* [LSA$^+$18] are the only full-scale molecular simulations of phase equilibria of complex coacervates.

In this section, we introduce a novel coarse-grained model and method for simulations of complex coacervates in the equilibrium with a reservoir. Our approach is similar to Ref. [APD$^+$18], however it differs in details, and it seems to be more systematic, efficient and general because it and allows to include the effects of pH, completely neglected in Ref. [APD$^+$18]. To prove that our model yield meaningful results, we first validate it against experimental results [LSA$^+$18], and then we explore the effects of polyion charge assymetry on the ion partitioning.

4.1.2 Model and methods

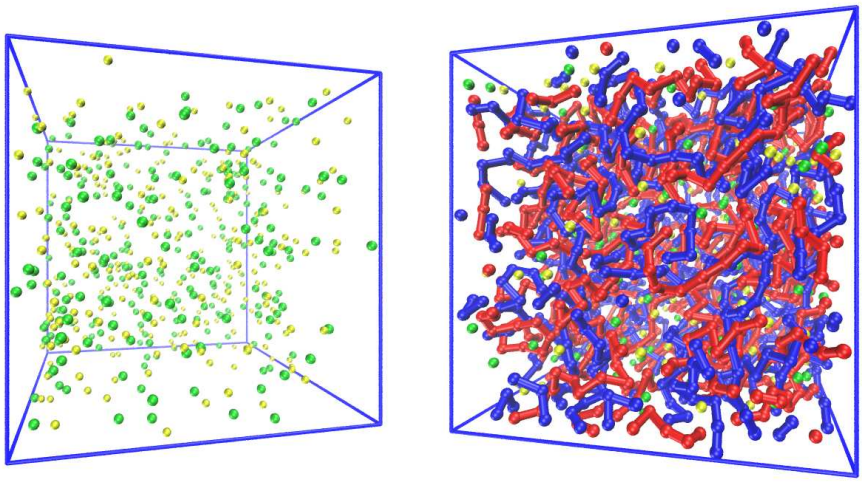

(a) salt reservoir (b) complex coacervate

Figure 4.2: Simulation snapshots of the salt reservoir at $c^{\mathrm{res}}_{\mathrm{NaCl}} \approx 530.6$ mM and the co-existing coacervate.
Color code: polyanion segments, A^-, polycation segments BH^+, Na^+ ions, Cl^- ions,

We carried out coarse-grained simulations of a system of linear polyelectrolytes, coupled to an external reservoir. The system representing the phase of complex coacervate contained N_+ strong polyanion and N_- strong polycation chains of length $M = 32$. We will denote the coacervate phase with the abbreviation IPEC, commonly used for interpolyelectrolyte complex. The model of a polymer chain was derived from Grest-Kremer model. Salt ions were modelled as point particles with a charge and excluded volume. Our simulations covered stoichiometric as well as non-stoichiometric compositions of the coacervate (N_+, N_-), where either $N_+ = 32$ and $N_- \in \{28, 30, 32\}$, or symmetrically $N_- = 32$ and $N_+ \in \{28, 30\}$, covering the polyanion fractions

$$x_- = \frac{N_-}{N_+ + N_-}, \tag{4.1}$$

in the range $x_- \in [0.467, 0.533]$. Typical box sizes were $L \approx 20\sigma \approx 7$ nm resulting in monomer concentrations ≈ 10M, or volume fraction $\phi \approx 10\%$ which is in the usual experimental range [SP20].

The polymer connectivity was represented by harmonic bonds with stiffness constant $k_r = 100 k_\mathrm{B}T/\sigma^2$ and equilibrium distance $r_0 = 1\sigma = 0.355$ nm. Each pair of particles interacted through the WCA interaction with $\varepsilon = 1 k_\mathrm{B}T$, corresponding to a good (athermal) solvent. In addition, charged particles interacted with full Coulomb potential with Bjerrum length $l_\mathrm{B} = 3\sigma = 1.065$ nm. The choice of l_B was arbitrary, however it qualitatively captured the fact that due to the low water content in the coacervate, the dielectric constant in the coacervate is lower as compared to $l_\mathrm{B} = 2\sigma = 0.710$ nm corresponding to aqueous solutions at room temperature. The solvent was treated as an implicit dielectric continuum, omitting its molecular structure.

The system was coupled to a reservoir of Na^+ and Cl^- ions via the Grand reaction method. We assume that the reservoir does not contain any polymer, which is a good approximation for sufficiently long chains, if x_- is not far from 1/2 and $c^\mathrm{res}_\mathrm{NaCl}$ is much lower than the critical salt concentration [LSA$^+$18]. Bjerrum length in the reservoir was set to $l_\mathrm{B} = 2\sigma = 0.710$ nm, and salt concentrations ranged in $c^\mathrm{res}_\mathrm{NaCl} \in [44.9\text{ mM}, 748.6\text{ mM}]$. The electrostatic energy and forces were evaluated using the P^{3}M method in both coacervate and reservoir phase. For better illustration, in Figure 4.2 we present simulation snapshots of the two phases.

We used Langevin dynamics to sample configurations along with the Grand-reaction MC moves to sample exchanges of small ions. Simulations were $2.5 \cdot 10^5 \tau$ long with $2.5 \cdot 10^7$ LD integration steps and $2.5 \cdot 10^6$ MC trials for ionic exchanges.

4.1.3 Validation of the coacervate model

First we describe how we determine the composition of the phases in equilibrium. Phase equilibrium of the reservoir and the coacervate is defined by two conditions: 1.) equality of the chemical potentials of species co-existing in both phases, 2.) equality of pressures in both phases. For the former, we assume that all polymers are in the coacervate, hence the salt ions are the only species exchanged between the phases, and the equality of the chemical potentials is assured by construction of the Grand-reaction method. For the latter condition, we introduce the *Pc-protocol*, further used also in other situations in this thesis. The key idea is to measure the pressure of the reservoir, and then find the density at which the pressure of the coacervate and the pressure of the reservoir is matched. First, we simulate the salt reservoir defined by the formal equilibrium constants of ion exchange (see Subsection 2.4.3), and measure the composition and pressure of the reservoir. Second, we carry out a series of simulations of a coacervate using fixed values of (N_+, N_-) in simulation boxes of various sizes, thus different monomer concentrations $c^\mathrm{ipec}_\mathrm{mon}$. In each of these simulations we measure the mean pressure of the coacervate, and subtract the pressure of the reservoir to obtain the *Pc*-curves, which are subsequently interpolated by a quadratic fit. The dependence of coacervate pressure on $c^\mathrm{ipec}_\mathrm{mon}$ does not follow a linear trend, and parabolic function seems to be the simplest function that accounts for the curvature and allows us a reasonable fit, albeit without a direct physical significance of the fit parameters

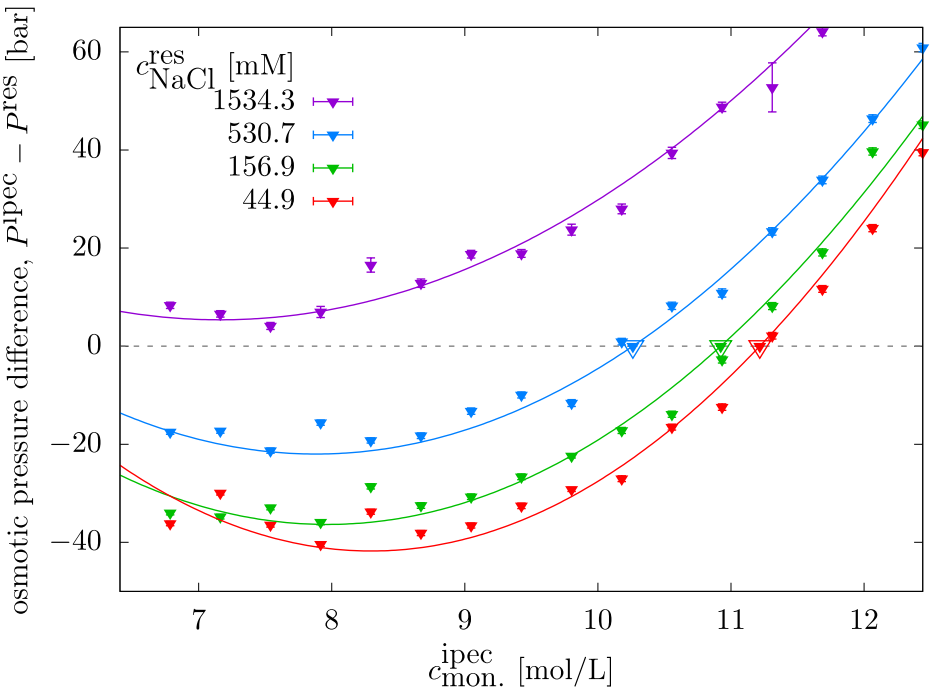

Figure 4.3: Pc-curves of the stoichiometric coacervate phase coupled to the reservoir defined by $c^{\text{res}}_{\text{NaCl}}$. The solid lines comprise the quadratic fits, and the points with highlighted borders are roots of the fits, denoting the point at which the phase equilibria is reached.

[KRH15]. The point at which $P^{\text{ipec}} = P^{\text{res}} \implies P^{\text{ipec}} - P^{\text{res}} = 0$ fulfills the condition 2.) above, hence corresponds to the phase equilibrium.

In Figure 4.3 we plot Pc-curves mapping the dependence of the pressure on the composition. We observe that for $c^{\text{res}}_{\text{NaCl}} \approx 1534$ mM, the Pc-curve does not intersect the zero-pressure line in Figure 4.3 ($P^{\text{ipec}} - P^{\text{res}} = 0$), indicating that at such $c^{\text{res}}_{\text{NaCl}}$, a separate coacervate phase in the equilibrium with the reservoir is not formed. Such a high salt concentration results in a high density of particles, increasing the contribution of the repulsive excluded-volume interactions to the pressure of the coacervate. Excluded-volume interactions along with the strong electrostatic screening due to the high salt content both suppress the formation of the complex. As $c^{\text{res}}_{\text{NaCl}}$ decreases, we observe an emergence of the coacervate phase, manifested by the existence of intersection between the Pc-curve and the zero-pressure line, highlighted by larger points in Figure 4.3. At these polymer densities the coacervate is in the chemical and mechanical equilibrium with the reservoir. A further decrease in $c^{\text{res}}_{\text{NaCl}}$ upholds the existence of the coacervate, however the equilibrium densities are shifted to higher values, because of diminished effect of steric repulsions of the salt ions in the complex, as their number decreases.

After constructing the Pc-curves, we carried out new simulations in the box of size exactly matching the equilibrium $c^{\text{ipec}}_{\text{mon}}$ determined by quadratic fits. The salt and polymer content resulting from these runs are plotted in the form of the phase diagram in Figure 4.4. One can appreciate the similarity of the phase diagram with the scheme in Figure 1.7 based on the experimentally measured phase diagrams. We observe that monomer concentrations in the coacervate are

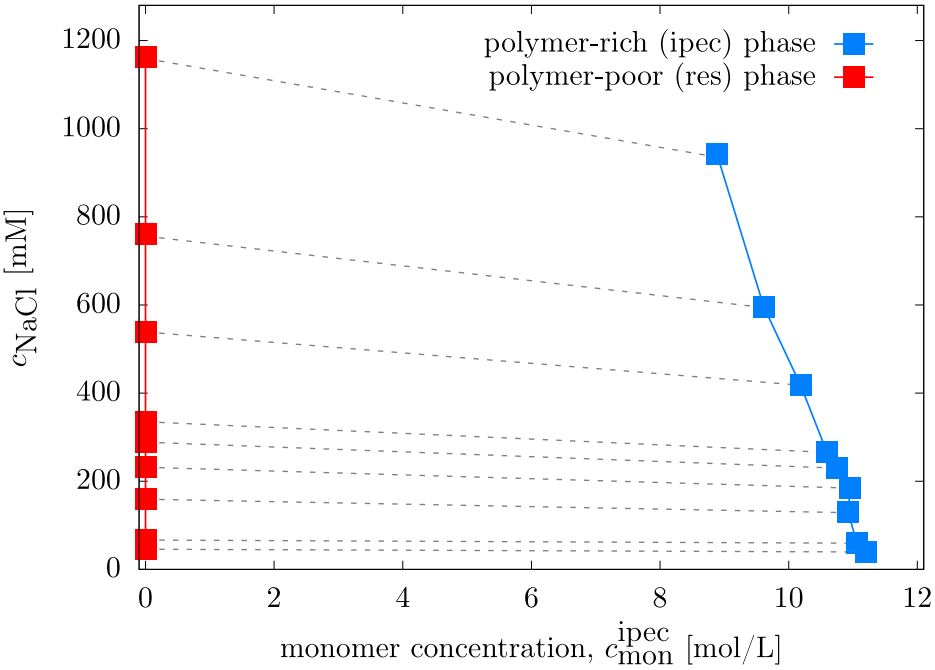

Figure 4.4: Salt content-vs.-polymer content phase diagram of the stoichiometric complex coacervate. The dashed tie-lines connect the co-existing states of the coacervate and the reservoir.

on the order of ~ 10 mol/L or $\sim 10\%$ corresponding to experimental observations [SP20]. Importantly, tie-lines connecting the co-existing states exhibit a negative slope, meaning that salt partitions preferentially to the reservoir as compared to the coacervate. For decades, it was believed that the salt prefers the phase of the coacervate, and only recent experiments proved the contrary to be true [LSA$^+$18]. The failure to capture the preferential partitioning of the salt to the reservoir is a common drawback of many theories, including the popular Voorn-Overbeek theory. However, our simulation model captures this spurious effect.

In Figure 4.5 we show that the partition coefficient of NaCl at $c^{\mathrm{res}}_{\mathrm{NaCl}} \lesssim 150$ mM is on the order of ~ 0.9, followed by a decrease at $c^{\mathrm{res}}_{\mathrm{NaCl}} \gtrsim 150$ mM to the value on the order of ~ 0.8. This trend agrees almost quantitatively with the experiments of Li *et. al.* [LSA$^+$18], further highlighting validity of our model and the simulation protocol.

4.1.4 A place in the episteme and limitations of the model

Herein, we challenge some assumptions and simplifications used in our model, and outline its limitations. Presumably the biggest pitfall of our simulations is the lack of proper description of interactions between the species in the coarse-grained model of the coacervate. For instance, representing the solvent as a dielectric continuum introduces a great simplification with respect to the reality. Because of the low water content in the coacervate, ions are on average separated only by a small number of water molecules [FS16], where the picture of a dielectric continuum is expected to fail [LAO12, OKP03]. Disregarding the possible local gradients in permittivity, not even an average permittivity in the coacervate phase is precisely

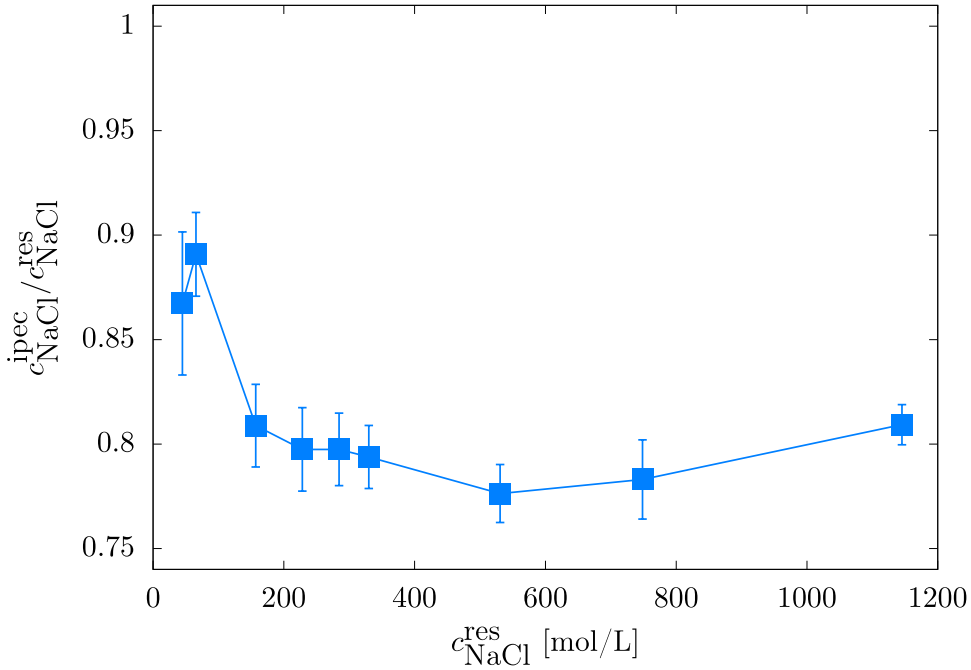

Figure 4.5: Partition coefficient of NaCl between the coacervate phase and the reservoir phase as a function of $c^{\mathrm{res}}_{\mathrm{NaCl}}$.

known from experiments. Our work in progress, not shown in this thesis, suggests that some features of our model are rather sensitive to the strength of electrostatic interactions – for example, a change of the Bjerrum length causes a significant change in the polymer content in the coacervate. Lytle *et. al.* [LS17] proposed to use the dielectric constant of aqueous solutions, which makes the electrostatic contribution to the coacervate behaviour presumably lower compared to the reality. Nevertheless, by tuning the excluded-volume interactions and using specific closures in the theoretical model, Lytle *et. al.* were able to match experimental phase diagrams. However, the extent of error cancellation in this approach is not completely clear. On the other hand, Li *et. al.* [LSA+18] treated the dielectric constant as a tunable parameter, and chose a value which resulted in the best agreement with experimental phase diagrams. The resulting dielectric constant used by Li *et. al.* was approximately equal to the one used by us. Finally, some experiments suggest that not only different permittivity, but also water structure plays a significant role in the formation of coacervates and partitioning of some ionic solutes [FS16]. All these problems might be in principle addressed by invoking atomistic polarizable models. However, the characteristic time scales and length scales at which coacervates evolve make the use of atomistic simulations prohibitively expensive.

Besides electrostatics, in some cases also specific short-range interactions are decisive for polyelectrolyte properties [Smi20]. Hydrogen bonds, hydrophobic effects, ion specific effects all affect properties of the coacervate in some experimental setups [SP20, RBL+17]. For example, the critical salt concentration decreases with salt identity following the Hoffmeister series [PLP+14]. To properly capture such effects is well beyond the resolution and capabilities of our coarse-grained model.

Nevertheless, the general consensus supported by a plethora of experiments is that coacervation is a generic effect governed mainly by electrostatic interactions, and principles of phase equilibrium. Our simulations are not meant to have a predictive power regarding partitioning and phase behaviour for any specific chemical species. On the contrary, they provide numerically exact results for a simple model which allows to decouple all specific effects from the underlying generic effects of electrostatics, polymer connectivity, etc. Our model accounts for the Donnan equilibrium and equality of chemical potential of small species in both phases, and thus it should yield qualitatively correct trends for the phase behaviour and ion partitioning.

Finally, when comparing simulations with experiments, one has to be aware, that the use of Grand-reaction method with Langevin dynamics samples the system properties in equilibrium. Various experiments show that interpolyelectrolyte complexes might exist also in metastable states or in kinetically arrested non-equilibrium states, governed by different principles. Especially, the latter are important for applications such as layer-by-layer assemblies composed of multilayered coacervates [Sin17].

To make a link to contemporary models and methods in the field, we provide a brief comparison of our model with a qualitatively similar model by Andreev *et. al.* [APD$^+$18], which recently attracted attention of the community. Both models use a generic model of a polymer chain derived from the Grest-Kremer model, and explicit salt ions. However, the system of Andreev *et. al.* contains also neutral particles representing the solvent, possessing only excluded-volume interactions. In our case, the solvent is implicit, the effective size of ions includes a hydration shell, and also formulation of the Grand-reaction method accounts for solvation energies. Another distinction is the protocol used to construct the phase diagram. Both models assume that there is no polymer in the reservoir. Andreev *et. al.* fixed the salt concentration in the reservoir, and used the Widom insertion method to measure the chemical potential of the salt and the pressure in the reservoir. Subsequently, they carried out a series of simulations of coacervate simultaneously adjusting both polymer and salt content in an iterative fashion, to find the equilibrium composition. Our approach seems more straightforward because it requires to tune only the polymer content, which can be done in a systematic and well-defined way which can be easily parallelized. Approach of Andreev *et. al.*, iteratively tuning of the composition by hand, seems less efficient and more prone to errors. In the same study, Andreev *et. al.* used also the Gibbs ensemble approach, which leads to the chemical and mechanical equilibrium by construction, without the need to tune compositions. However, simulations in the Gibbs ensemble are generally expensive, as compared to our Grand-reaction scheme, because the Gibbs ensemble requires to simulate the reservoir and coacervate simultaneously, while the Grand-reaction scheme allows to decouple them. Furthermore, Gibbs ensemble might become very inefficient when dealing with partitioning of solutes whose partition coefficients are far from unity – for example multivalent ions, as will be shown in the next subsection. Finally, in contrast to Andreev *et. al.*, the Grand-reaction method can be directly extended to weak polyelectrolytes to explore the coacervate properties as a function of pH, as we are planning to do in the future.

4.1.5 Introducing charge asymmetry of the coacervate

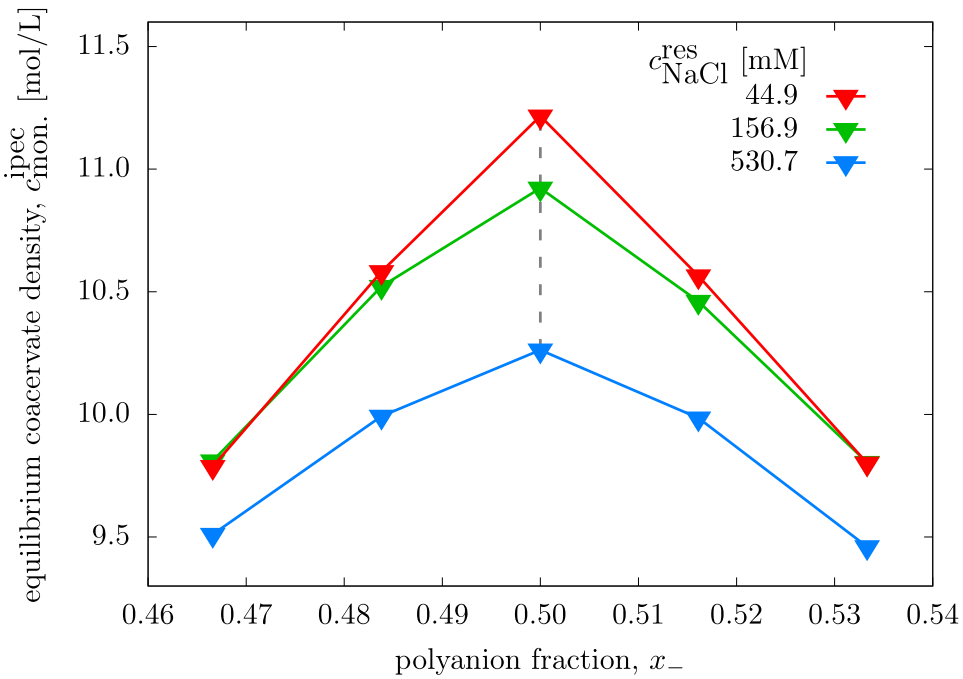

Figure 4.6: Equilibrium polymer concentration in the coacervate phase as a function of polyanion fraction in the coacervate plotted for various c^{res}_{NaCl}. Dashed lines connect points which belong to the binodal in Figure 4.4.

We made a case for legitimacy of our model by comparing its results to experiments on stoichiometric complexes. Now we apply this model to a less understood system of non-stoichiometric complexes. We introduce the charge assymetry into the coacervate, and follow the *Pc*-protocol to determine the equilibrium composition of the coacervate at a given anion fraction. Figure 4.6 shows equilibrium polymer concentration as a function of the polyanion fraction, x_-, for various c^{res}_{NaCl}. The charge assymetry in the coacervate decreases its equilibrium density, hence shrinking the two-phase region of the corresponding phase diagram. This is in agreement with experiments [CSET10], and is caused by the interruption of percolation [CBD$^+$13] of the coacervate, and by lowering the charge and bonding correlations, which promote the formation of the complex [ZAWW18]. One can acknowledge that our model preserves the symmetry upon the permutation of charge signs – the system with inverted numbers of polyanions and polycations converge to the same equilibrium composition, as manifested by the symmetry of Figure 4.6.

In contrast to the stoichiometric complexes discussed above, the net charge of the polymers in the coacervate imposes a non-zero Donnan potential between the two phases. In Figure 4.7 we show partition coefficients of small ions between the coacervate and the reservoir as a function of the polyanion fraction, compared to the Donnan theory estimates for an ideal system. We see that at $c^{res}_{NaCl} \approx 44.9$ mM, increasing the polyanion fraction promotes the accumulation of Na^+ counterions in the phase of coacervate, in order to maintain the electroneutrality. The partition coefficient of Na^+ counterions is on the order of ~ 10, suggesting that coacervates might be used as scavengers of small ions with the

charge opposite to the sign of the excess charge of the coacervate phase. We see that the partitioning of monovalent ions is well described by the Donnan theory. In contrast to Na^+ counterions for $x_- > 1/2$, the Donnan effects suppresses the partitioning of Cl^- counterions into the phase of the coacervate. Expectedly, the Donnan potential between the reservoir and coacervate becomes zero at stoichiometric composition $x_- = 1/2$, predicting the partition coefficient of unity for both Na^+ and Cl^-. However, simulations for $x_- = 1/2$ from the preceding section demonstrate the partition coefficient on the order of ~ 0.8. This difference can be attributed to inter-particle interactions, whose contribution we quantify by calculating the excess chemical potentials.

By invoking the condition of chemical equilibrium of ions co-existing in two phases [LHR+20], we obtain

$$\begin{aligned}
\mu_i^{\text{ipec}} &= \mu_i^{\text{res}} + z_i\mu^{\text{Don.}}, \\
\mu_i^{\text{ipec}\|\text{id.}} + \mu_i^{\text{ipec}\|\text{ex.}} &= \mu_i^{\text{res}\|\text{id.}} + \mu_i^{\text{res}\|\text{ex.}} + z_i\mu^{\text{Don.}}, \\
-k_{\text{B}}T\ln\left(\frac{c_i^{\text{ipec}}}{c^{\ominus}}\right) + \mu_i^{\text{ipec}\|\text{ex.}} &= -k_{\text{B}}T\ln\left(\frac{c_i^{\text{res}}}{c^{\ominus}}\right) + \mu_i^{\text{res}\|\text{ex.}} + z_i\mu^{\text{Don.}}, \\
P_i = \frac{c_i^{\text{ipec}}}{c_i^{\text{res}}} &= \exp\left(-\frac{z_i\mu^{\text{Don.}}}{k_{\text{B}}T} - \frac{\Delta\mu_i^{\text{ex.}}}{k_{\text{B}}T}\right),
\end{aligned} \tag{4.2}$$

where P_i is the partition coefficient and $\Delta\mu_i^{\text{ex.}}$ is the difference of excess chemical potentials of ion i between the phases. The first term of the argument of the exponential in (4.2) is the Donnan potential, and can be calculated from I^{res} and x_-. The second term is the contribution of interactions to the partitioning, and can be calculated from the knowledge of the Donnan contribution, and P_i, which is the ouput of simulations. In Figure 4.8 we plot various contributions to partitioning from Figure 4.7. The Donnan contribution for $c_{\text{NaCl}}^{\text{res}} \approx 44.9$ mM is on the order of $2k_{\text{B}}T$ per particle, which dominates over the effect of interactions with virtually zero contribution. The role of interactions becomes more significant in the limit of high $c_{\text{NaCl}}^{\text{res}}$. Figure 4.7 shows a bigger difference between the simulation and the Donnan theory for $c_{\text{NaCl}}^{\text{res}} \approx 530.6$ mM, when compared to the $c_{\text{NaCl}}^{\text{res}} \approx 44.9$ mM. The quantitative analysis of the contributions to the chemical potential, presented in Figure 4.8, unveils that the Donnan effect and the inter-particle interactions are comparable in magnitude at $c_{\text{NaCl}}^{\text{res}} \approx 530.6$ mM for $x_- \neq 1/2$, which is lower than $k_{\text{B}}T$ per particle. Hence, increased $c_{\text{NaCl}}^{\text{res}}$ decreases the partition coefficients of Na^+ ions to the order of unity, if $x_- > 1/2$.

These results imply that if the total ionic strength of the reservoir is low, then the ion partitioning is well approximated by the Donnan theory, suggesting that the control parameter is x_-/I^{res}. In contrast, at high I^{res}, the Donnan potential decreases, hence the relative importance of the inter-particle interactions to the partitioning increases. Thus, at high I^{res} the Donnan theory only qualitatively describes the trends which emerge from simulations.

4.1.6 Partitioning of multivalent ions

Finally, we couple the coacervate to the reservoir containing a mixture of monovalent and divalent salt, which we will denote as $MgCl_2$ for convenience. The divalent ion is generic, and possesses the same excluded-volume interactions as

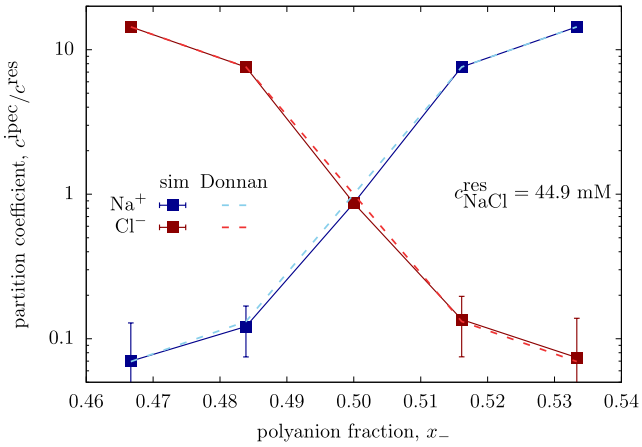

(a) $c_{\mathrm{NaCl}}^{\mathrm{res}} = 44.9$ mM

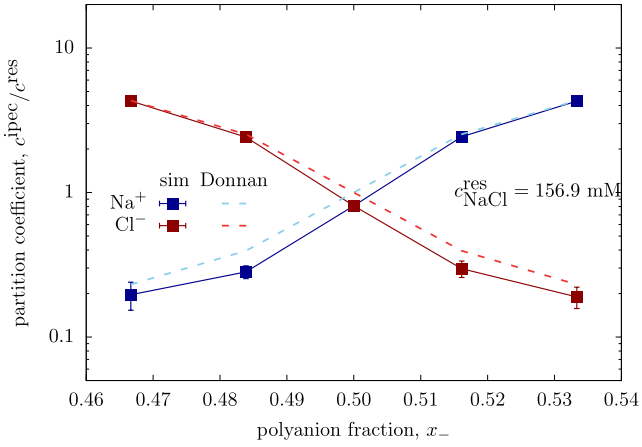

(b) $c_{\mathrm{NaCl}}^{\mathrm{res}} = 156.9$ mM

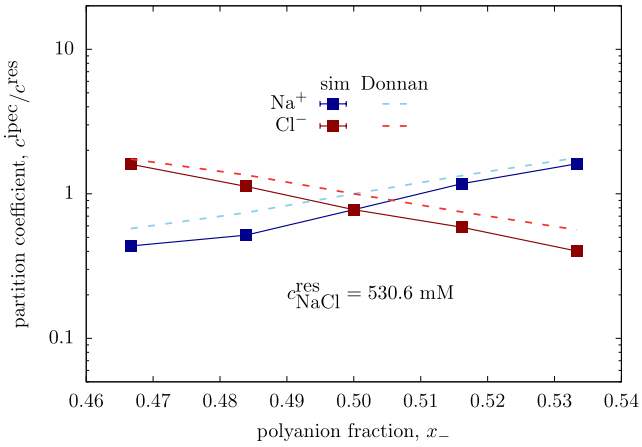

(c) $c_{\mathrm{NaCl}}^{\mathrm{res}} = 530.6$ mM

Figure 4.7: Partition coefficients of small ions exchanged between the coacervate and the reservoir as a function of polyanion fraction for various $c_{\mathrm{NaCl}}^{\mathrm{res}}$. The solid lines are guide to eye for points obtained from the simulations, while the dashed lines represent estimates from the Donnan theory.

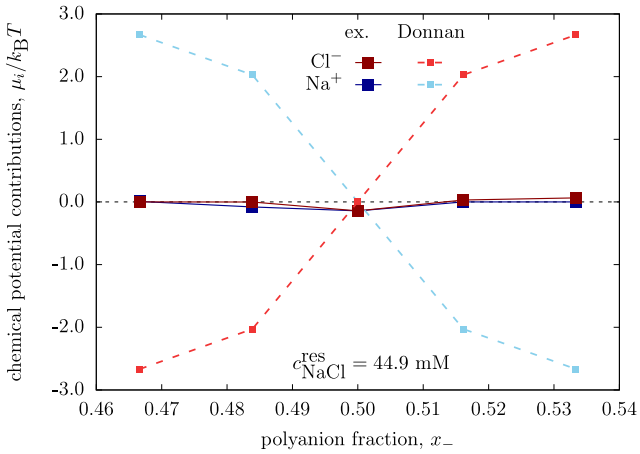

(a) $c^{res}_{NaCl} = 44.9$ mM

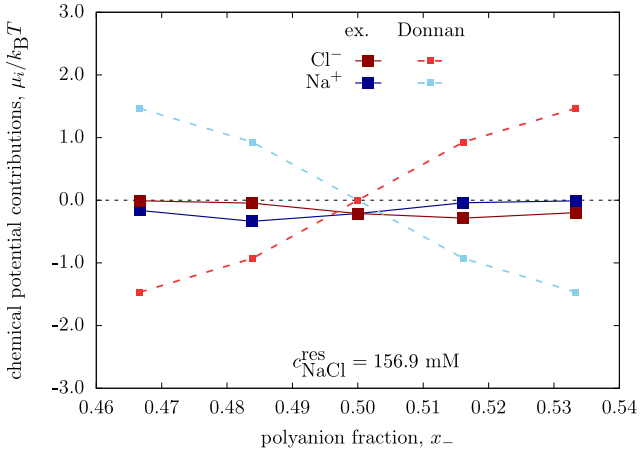

(b) $c^{res}_{NaCl} = 156.9$ mM

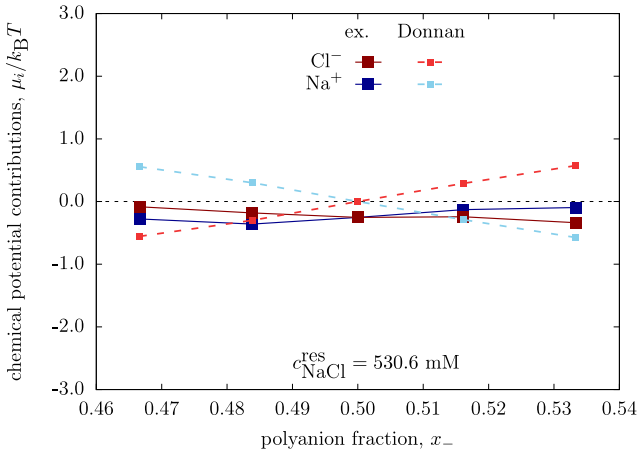

(c) $c^{res}_{NaCl} = 530.6$ mM

Figure 4.8: The contributions of the Donnan effect and inter-particle interactions to partition coefficients of small ions exchanged between the coacervate and the reservoir as a function of polyanion fraction for various c^{res}_{NaCl}. The solid lines are guide to eye for the contributions of interactions, while the dashed lines represent the Donnan contribution.

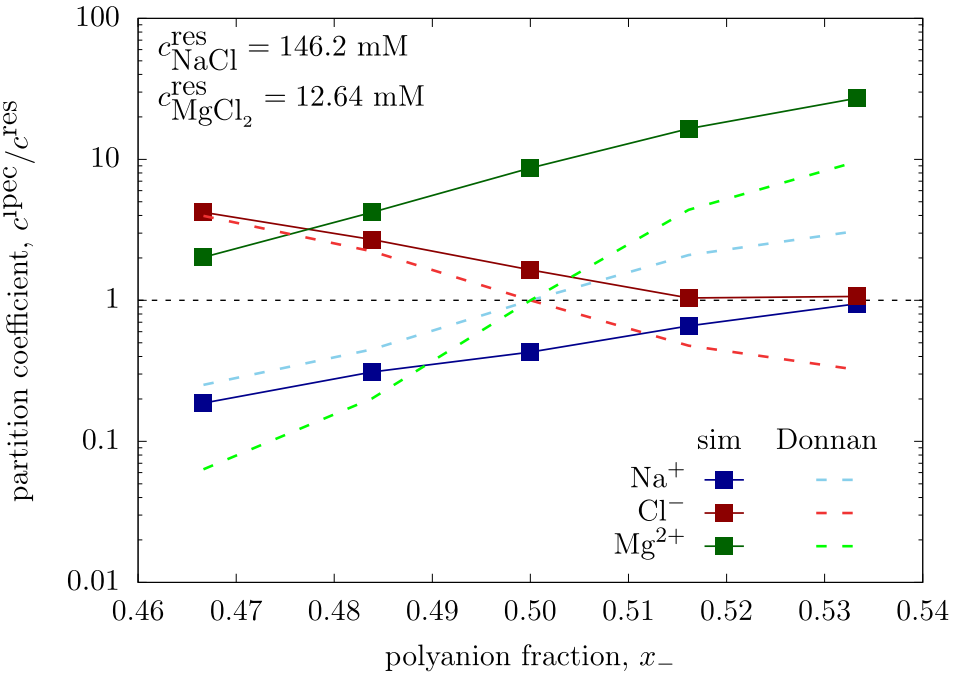

Figure 4.9: Partition coefficients of small ions exchanged between the coacervate and the reservoir as a function of polyanion fraction for $c^{res}_{NaCl} \approx 146.2$ mM and $c^{res}_{MgCl_2} \approx 12.64$ mM. The solid lines are guide to eye for points obtained from the simulations, while the dashed lines represent estimates from the Donnan theory.

Na^+, while having the charge +2. We carried out a simulation of reservoir for $c^{res}_{NaCl} \approx 146.2$ mM and $c^{res}_{MgCl_2} \approx 12.64$ mM, hence the total ionic strength $I^{res} \approx 184.1$ mM. We followed the Pc-protocol to find the equilibrium density of the non-stoichiometric coacervate in the equilibrium with the above mentioned reservoir, and calculated the equilibrium concentrations of each species. In Figure 4.9 we plot the calculated partition coefficients compared to the Donnan theory estimates. The partition coefficient of Mg^{2+} and Na^+ increases with x_- as the polymer charge increases, while Cl^- exhibits a decrease in partition coefficient as a function of x_-. Such qualitative trends were expected from the Donnan theory, however, Figure 4.9 shows significant differences between the analytical theory and simulations.

At $x_- = 1/2$, where the Donnan potential is zero, the partition of Mg^{2+} is on the order of ~ 10, suggesting the importance of inter-particle interactions, which evidently promotes the preferential partitioning of divalent ions into the coacervate. At $x_- = 1/2$, we simultaneously observe an unequal partitioning of univalent ions, with a preference for Cl^- presumably because of the abundance of Mg^{2+} which need to be neutralized.

Shift from $x_- = 1/2$ to $x_- > 1/2$ introduces the Donnan effect, further increasing the partition coefficients of Mg^{2+} and Na^+, while excluding Cl^-. Interestingly, at $x_- < 1/2$ we still observe that Mg^{2+} slightly accumulate in the coacervate with the partition coefficient on the order of ~ 2, which is ~ 20-times higher than predicted by the Donnan theory. Additionally, the Donnan theory underestimates the partitioning of Mg^{2+} and Cl^-, while simultaneously overestimates the partitioning of Na^+ in the whole range of x_-.

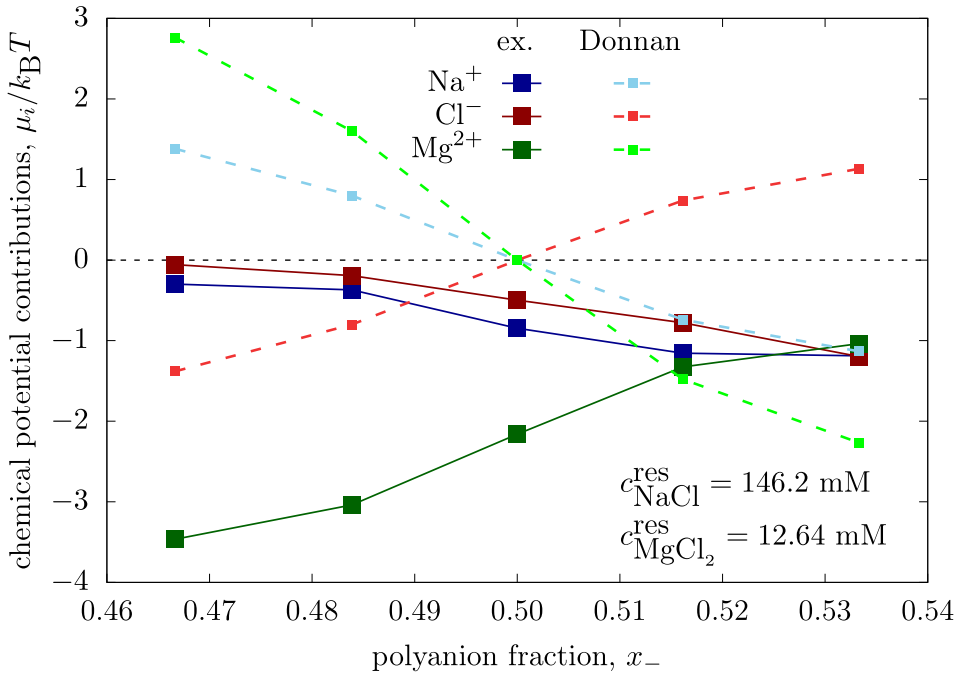

Figure 4.10: The contributions of the Donnan effect and inter-particle interactions to partition coefficients of small ions exchanged between the coacervate and the reservoir as a function of polyanion fraction for various c^{res}_{NaCl}. The solid lines are guide to eye for the excess chemical potentials, while the dashed lines represent the Donnan contribution.

To understand the role of the Donnan effect and the interactions, in Figure 4.10 we present the contributions to the chemical potentials to the partitioning. Unfortunately, the results presented in Figure 4.10 were obtained only few days before submitting this thesis, therefore, their full interpretation is still not clear to us. We hypothesize that, in order to fully understand these phenomena, and additional analysis of respective contributions of electrostatics and excluded-volume interactions is needed. However, we will point out a few non-trivial observations, which can be made based on the currently presented data.

For example, we observe that the excess chemical potential of Mg^{2+} at $x_- < 1/2$ is on the order of $\sim 3k_BT$ per particle, as compared to $\sim 1k_BT$ at $x_- > 1/2$. The latter is quite surprising, taking into account that coacervate at $x_- < 1/2$ has a net positive charge, and one would expect the electrostatic repulsions to increase the excess chemical potential of Mg^{2+}. In addition, the excess chemical potential of Mg^{2+} at $x_- < 1/2$ is quite large in magnitude, and comparable with the magnitude of with Donnan effect, resulting in approximate cancellation of the two strong effects, thus yielding $P_{Mg^{2+}} \sim 1$.

In contrast to the cancellation at $x_- < 1/2$ for Mg^{2+}, a synergistic action of the interactions and the Donnan effect is observed at $x_- > 1/2$. However, in spite of negative net charge on the polymer, the magnitude of the excess chemical potential of Mg^{2+} decreases with increasing x_-. We surmise, that the latter is the results of more pronounced excluded-volume repulsions between particles. Nevertheless, an additional analysis of the interactions is needed, and is planned in the future.

4.1.7 Conclusion

We presented a novel model of a complex coacervate co-existing with reservoir of ionic solution. Our simulation protocol uses the Grand-reaction method to calculate phase diagrams of coacervates and partition coefficients of simple ions between the coacervate and reservoir. Our model captures the existence of the critical point, preferential partitioning of uni-univalent salt into the reservoir, and other non-trivial effects, which have been weak points of many commonly used theoretical approaches.

We have shown that charge asymmetry of the coacervate leads to a shrinkage of the two-phase window of the phase diagram of coacervates, however, preserving the existence of a separate stable phase. The net polymer charge in the coacervate causes an unequal partitioning of small ions, due to the presence of the Donnan effect. In the case of uni-univalent salt, the quantification of the excess chemical potentials, and the Donnan potential for single salt ions demonstrated that the Donnan theory almost quantitatively describes the partitioning at low $c^{\mathrm{res}}_{\mathrm{NaCl}}$. The Donnan theory retains only qualitative validity at high $c^{\mathrm{res}}_{\mathrm{NaCl}}$ because the Donnan contribution decreases to a magnitude comparable to the effect of inter-particle interactions.

The role of inter-particle interactions becomes important also in the presence of multivalent ions. Divalent cations preferentially accumulate in the phase of coacervate, even if the coacervate contains a slight excess of polycation. Contributions to the chemical potential due to the Donnan effect and inter-particle interactions are both strong, each of them significantly exceeding $k_{\mathrm{B}}T$ per particle in the whole range of x_{-}. In addition, the effects are coupled together, suggesting that neither of them alone can be used to explain the ion partitioning in such systems. A further analysis of the role of valency is desired before moving towards more complex solutes, such as oligopeptides or weakly acidic or basic particles.

Although we have simulated only strong polyelectrolytes with permanent ions, the method can be straightforwardly extended for weak polyelectrolytes, and pH-responsive solutes. We are planning to elucidate the effects of the pH on the coacervate phase behaviour in our forthcoming work.

4.1.8 Outlook

As suggested above, our next steps will lead mainly in two somewhat orthogonal directions: 1.) more complex solutes, 2.) the effects of pH.

For the latter, we plan to replace the strong polyelectrolytes by weak ones, couple the coacervate to the reservoir defined by $c^{\mathrm{res}}_{\mathrm{NaCl}}$ and $\mathrm{pH}^{\mathrm{res}}$, and explore the phase behaviour and ion partitioning as a function of pH. To our knowledge, the relation between the stability of coacervate and pH has not been studied theoretically or by a simulation, in spite of the well-known importance of the effect of pH in experiments [SP20].

For the former, our ultimate goal is to understand the partitioning of more complex solutes such as small oligopeptides or particles with patchy charges, to explain the mechanisms involved in selective encapsulation of proteins [vLCL19]. In theory, our coacervate model enables to simulate partitioning of more complex solutes using the same scheme, as presented above. However, in practice, Monte Carlo schemes become inefficient when inserting bulky solutes into the dense

coacervate phase, as presaged in Section 2.3.1. To measure the difference between the free energy of solute in the coacervate and the reservoir, we propose to use the thermodynamic integration method in a similar way as Kanduč *et. al.* used it for calculation of transfer free energies of solutes between a solvent and PNIPAM gels [KKRD19].

With an exception of Section 4.2, all simulations in this thesis were carried out using `ESPResSo` [WWS+19] – an extensible software package for simulating soft matter systems. The kernel of the program is written in `C++`, while the communication between the user and core is provided via a `Python` scripting interface, to which the kernel is imported as a `Python` module. Thermodynamic integration is not available in `ESPResSo`, and we are currently implementing it on the `Python` level. The following paragraphs describe the main features and preliminary results of our implementation, disregarding the technical details.

Thermodynamic integration for the solute in the coacervate was done by introducing the coupling parameter λ, as described in Section 2.3.2, and carrying out two subsequent steps: First, switching off the charges on the solute; Second, switching off the excluded volume interaction between the solute and the rest of the system. The former was done by usual linear scaling procedure, as used by Anwar *et. al.* in salt melts [AFN03]. The latter was done by a rather exotic parametrization of potential

$$U_{\mathrm{LJ}}(r) \mapsto U_\lambda(r) = \lambda^4 U_{\lambda=1}(r), \tag{4.3}$$

proposed by Mezei [Mez89], in contrast to popular "soft-core" schemes, as used for instance in Ref. [KKRD19]. The dependence of shape of the potential well on the coupling parameter for (4.3) is depicted in Figure 6.1. Following the parametrization (4.3) we obtain

$$\left\langle \frac{\partial \mathcal{U}}{\partial \lambda} \right\rangle = \left\langle \frac{\partial U_{\mathrm{LJ}}}{\partial \lambda} \right\rangle = 4\lambda^3 U_{\lambda=1}. \tag{4.4}$$

The advantage of this parametrization is that the measurement of $\langle \partial U/\partial\lambda \rangle$ can be done by using highly optimized functions for energy calculation, already built-in in `ESPResSo`. A drawback of the above parametrization, when compared to the "soft-core" schemes is, that it can create spurious singularities in some cases. However, the numerical stability of both schemes has been thoroughly investigated before [Mez89, BMvS+94, SMC07]. It turns out, that the scheme (4.3) usually avoids singularities, but converges slower as compared to the "soft-core" ones.

We tested the validity of our implementation of thermodynamic integration on two test systems: 1.) Calculation of the excess free energy of a Lennard-Jones fluid to verify that our protocol calculates excluded-volume contributions correctly, 2.) Calculation of the excess chemical potential of NaCl in implicit solvent to verify that our protocol calculates the contribution of electrostatics correctly.

In the former case, we tested our implementation against the study of Mezei [Mez89], in which he estimated the excess free energy per particle of a Lennard-Jones fluid at density $\rho = 0.8\ N/\sigma^3$ and reduced temperature $T^* = 0.75 k_{\mathrm{B}}T/\varepsilon_{\mathrm{LJ}}$, yielding a value $\mathcal{A}^{\mathrm{ex.}}/k_{\mathrm{B}}T = -3.363 \pm 0.001$. Our thermodynamic integration,

carried out in the system of 200 particles at the same parameters resulted in the integration profile depicted in Figure 6.2, which yielded $\mathcal{A}^{\text{ex.}}/k_{\text{B}}T = -3.34 + 0.04$, matching the result of the reference study within the statistical uncertainty.

In the latter case, we tested our implementation against the methods of Widom insertion and Grand-reaction Monte Carlo, and against experimental results of Truesdell *et. al.*, who measured activity coefficients of ions in aqueous NaCl solutions [Tru68]. Preliminary results in Figure 6.3 show that the thermodynamic integration provides a quantitative agreement with both Widom insertion and Grand-reaction methods and with the experiment. Additionally, all these results are consistent with the extended Debye-Hückel theory if $c_{\text{NaCl}} \lesssim 100$ mM where the assumptions of the theory are valid. Furthermore, the almost quantitative agreement with the experiment suggests that the parameters used in our simulations correctly capture the thermodynamic aspects of behaviour of NaCl ions in aqueous solutions.

To conclude, our preliminary results indicate that our implementation of thermodynamic integration is correct. In the next step, we are about to test it against Grand-reaction method for uni-univalent salt in the phase of coacervate, and compare the resulting partition coefficients. In the case of consistent results, we plan to use thermodynamic integration to calculate partition coefficients of small peptides and particles with patchy charges.

4.2 The origins of polyelectrolyte proclivity for multivalent ions

In this section, we explore underlying principles governing the interactions between polyelectrolytes and multivalent ions. Understanding of such interactions is important for water-treatment applications [OMGG16, PLW+16], which utilize polyelectrolytes for capturing metal ions. In addition, multivalency is an imporant motif commonly occurring in supramolecular assembly [AMVL+13], biological systems [SMVV17] or responsive materials [TS12]. To understand the role of valency in polyelectrolyte-counterion interactions in a greater detail, we chose a simpler system, as compared to coacervates – a single star-like weak polyelectrolyte in a dilute solution. The star presents the simplest branched system with radial symmetry, often serving as a starting point for theories describing gels or brushes. This section presents the results of our publication [SNUK20] which builds on preliminary results presented in the Bachelor's thesis [Sta18], where we simulated short chains of length $N = 48$ monomers providing the proof of concept. In the publication we extended the system in size, modified the architecture to the star-like one, and provided a more sophisticated analysis of the relevant quantities.

4.2.1 Introduction

Macromolecular architecture and topology has profound influence on polyelectrolyte properties. For example, ionization of weak star-like polyelectrolytes [PBL+05, UKZB16, UKL+14] is suppressed as compared to the linear ones, because of increased segment density near the branching points. Many widely used theories to describe star-like polyelectrolytes are based on the Poisson-Boltzmann equation [JL09, KWLF+99]. This provides a reasonable approach for aqueous solutions of stars in the presence of monovalent ions.

However, the presence of multivalent ions brings strong charge-charge correlations [NKFP13], thus breaking the assumptions of mean-field theories. For example, the Poisson-Boltzmann equation implies that the distribution of monovalent counterions around the polymer is the same as the distribution of z-valent ions at z-times lower concentration. However, computer simulations [DHM00] show significantly different distributions in the two cases, underlining the importance of correlations.

Numerous experiments and other computer simulations show that multivalent ions have strong anomalous effect on polyelectrolytes in solutions [JBB13, CD16, OdlCBD+95, SOdlC00, TIM20], brushes [YMY+16, NXKD20] or hydrogels [YHDdP08]. Multivalent ions affect rheological properties of polyelectrolyte solutions [WJD+19], the friction between polyelectrolyte brushes [YJX+18] or force-extension behaviour of polyelectrolyte chains [IGPSS19]. Furthermore, as little as one molar percent of La^{3+} ions is sufficient to collapse strong polyelectrolyte brushes [MLH+06, MHBJ08]. Concurrently to the collapse, multivalent ions accumulate in the brushes, and also in hydrogels [OMGG16, PLW+16]. A widely accepted explanation for the phenomenon is based on entropy arguments: Upon localizing a z-valent ion in the brush, z monovalent ions are effectively expelled and released to the solution, increasing their translational entropy. The

change of the free energy is of the order of $\sim (z-1)k_{\mathrm{B}}T$. Even though, different counterions differ in their ion-specific effects, the underlying nature of the accumulation is immanent to the valency itself, as Plamper *et. al.* [PWMB07] demonstrated by using complex counterions with valency switchable by UV light.

The interplay between multivalent ions and polyelectrolytes becomes even more complex when considering weak polyelectrolytes. Molecular simulations by Panagiotopoulos [Pan09] demonstrated that increasing the strength of electrostatic coupling enhances the ionization of a linear weak polyelectrolyte, and collapses the chain. He anticipated the same behaviour also for weak polyelectrolyte in the presence of multivalent ions at low coupling strength. Simulations by Carnal *et. al.* [CUS10, CS11] indeed supported this prediction for linear chains. However, a link to experiments is mostly indirect, since the degree of ionization of a polyelectrolyte is not trivial to measure. For instance, experiments by Qu *et. al.* [QJWZ17] observed collapse of weak polycations upon addition of $SO_4{}^{2-}$ ions. Additionally, as the concentration of $SO_4{}^{2-}$ increased, the collapse was observed at a higher pH, suggesting a shift in the ionization. Similarly, Horkay *et. al.* [HTB01] observed a collapse of PAA gels by multivalent ions at pH where PAA should be neutralized, again suggesting a shift of the ionization. These results are consistent with the molecular model by Nap *et. al.* [NPS18], who observed collapse of weak polyelectrolyte brushes in addition of Ca^{2+} ions. Nevertheless, their work included an additional term for ion specific effects of Ca^{2+} promoting the collapse. Contrarily, recent work by Rathee *et. al.* [RSSW17] shows that weak star-like polyelectrolytes in the presence of divalent ions, swell instead of collapsing. However, the polyelectrolyte simulated by Rathee *et. al.* was hydrophobic, and thus collapsed at low ionization even in the absence of multivalent counterions.

The open question, that we address here, is how multivalent ions affect the ionization of a weak polyelectrolyte, and what is the concomitant conformational response. According to the above mentioned works, two scenarios are possible: First, multivalent ions might enhance the ionization, and swell the polymer as a result of the increased charge on the backbone, as suggested by Rathee *et. al.*; Second, multivalent ions might collapse the chain in a fashion similar to quenched polymers with a fixed charge, as suggested by Carnal *et. al.* To answer this question, we carried out simulations of a weak polyelectrolyte in good solvent, in which the polymer is swollen even if not charged. To provide the fundamental understanding of the effect of valency, all excluded volume interactions in our simulations are repulsive, as opposed to Rathee *et. al.* and Nap *et. al.* In this way, any possible collapse is driven only by electrostatic interactions. We analyze titration curves and gyration radii of stars in the presence of salts with various valencies. Then, we analyze the density profiles, in order to quantify the ion accumulations and propose an explanation for the observed effects.

4.2.2 Model and methods

We carried out simulations of a weak star-like polyelectrolyte in aqueous solution in the presence of a background salt. The star was composed of 5 arms with 19 monomers per arm, bonded to a central segment, totalling $N = 1 + 5 \times 19 = 96$ monomers at concentration ≈ 14 mM. The used monomer concentration could be

mapped to ≈ 1 g/L for PAA which is a usual concentration used in experiments. Each monomeric unit of the polyelectrolyte chain was modeled as a weak acid, defined by acidity constant K_A, and could undergo the ionization reaction

$$\mathrm{HA} \rightleftharpoons \mathrm{A}^- + \mathrm{H}^+. \tag{4.5}$$

The salt present in the solution was denoted as $\mathrm{M}^{z+}\,\mathrm{X}_z^-$, and its concentration was controlled by the charge ratio, defined as $\xi = nz/N$, where n is the number of z-valent ions in the simulation box. We carried out simulations for $\xi \in \{0.25, 0.50, 1.00\}$ and $z \in \{1, 2, 3\}$. To give an example, the simulated systems at $\xi = 0.50$ consisted of either, 48 M^+ and 48 X^- if $z = 1$, or 24 M^{2+} and 48 X^- if $z = 2$, or 16 M^{3+} and 48 X^- if $z = 3$. Each salt ion was represented explicitly as a point particle with a charge and excluded volume interactions as described below.

Every pair of particles interacted via a short-range repulsive potential

$$\frac{U(r)}{k_\mathrm{B}T} = \frac{3}{2}\frac{(r-2b)^2}{r^2}, \tag{4.6}$$

where $b = 0.4$ nm has the physical meaning of the effective size of the particle. The value of the parameter b was chosen in such a way that together with harmonic bonding potential with the stiffness constant $k = 24.4 k_\mathrm{B}T/\mathrm{nm}^2$ it reproduced the effective size of a PAA monomeric unit. If compared to Lennard-Jones interaction, the potential in (4.6) is softer, which improves the stability of integration in our simulation protocol, while retaining a purely repulsive nature. Charged particles interacted via the Coulomb potential, with $l_\mathrm{B} = 0.7$ nm $\approx 1.75b$ corresponding to aqueous solutions at room temperature. Calculation of electrostatic energy utilized the Ewald summation with metallic boundary conditions.

We employed the reaction ensemble method to sample both the configurational space and the composition space. The conformational moves were performed using Hamiltonian Monte Carlo [DKJR87, Irb94]. Random velocities drawn from the Maxwell-Boltzmann distribution were assigned to all particles, and a sequence of 20 steps of microcanonical MD with a time-step $\Delta t = 0.3\tau$ was preformed. The generated configurations were either rejected or accepted using the Metropolis MC algorithm. Reaction moves were the same as the ones described in Subsection 2.4.2, accepted or rejected using criterion (2.23). Titration curves were constructed using the $\mathrm{p}K_\mathrm{A}$-sweep mode with $\mathrm{p}K_\mathrm{A} \in \{-6, -5, \ldots, 1, 2\}$ covering the whole range of degrees of ionization $0 \leq \alpha \leq 1$. A typical simulation was 10^6 MC steps long and yielded $\sim 10^4$ uncorrelated samples of R_g which was a quantity with the slowest evolution. Simulations were carried out in the software `pe` developed in our group [UKL+14, UKZB16].

4.2.3 Enhanced ionization in spite of the collapse

In Figure 4.11 we compare titration curves of a star-like polyelectrolyte in the presence of mono-, di- and trivalent counterions at charge ratio $\xi = 0.50$. The presence of multivalent ions deforms the titration curves and shifts them to higher ionizations. However, the total charge on the salt is kept constant between the curves and therefore, ionic strength is different in each of the systems. To show

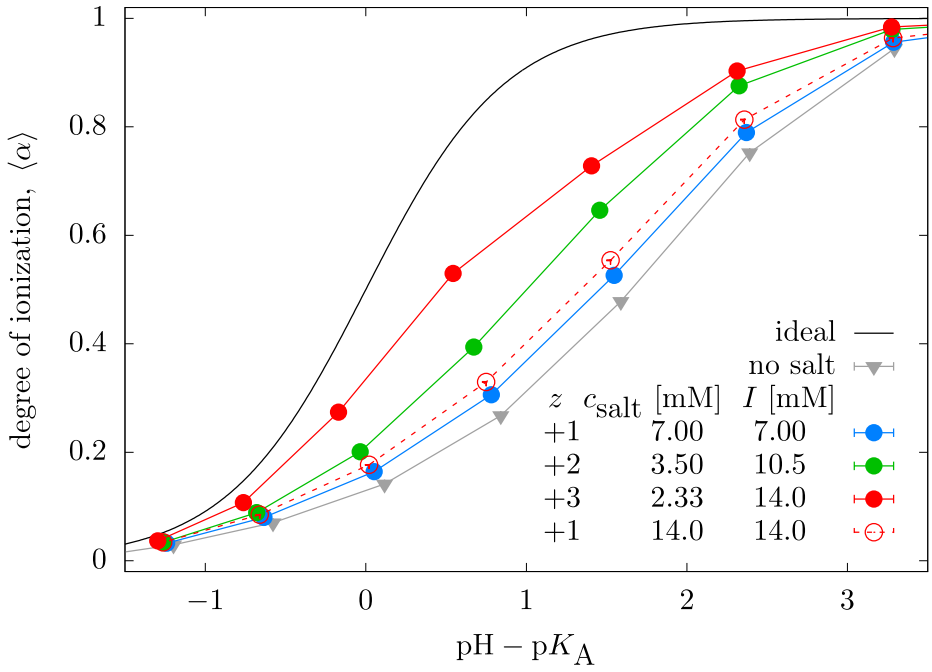

Figure 4.11: Titration curve of a weak star-like polyacid in presence of salt of different valencies at the charge ratio $\xi = 0.50$. Results for trivalent salt are directly compared to the system with uni-univalent salt at the same ionic strength.

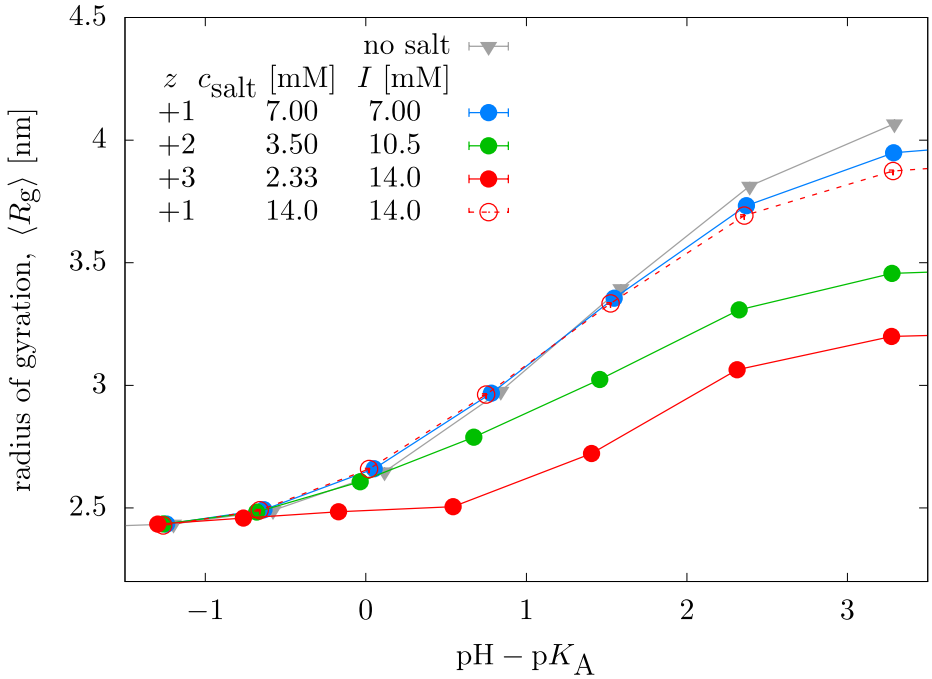

Figure 4.12: Radius gyration of a weak star-like polyelectrolyte as a function of pH − pK_A in presence of salt of different valencies at the charge ratio $\xi = 0.50$. Results for trivalent salt are directly compared to the system with uni-univalent salt at the same ionic strength.

that the observed shift of ionization is mainly the effect of valency and not electrostatic screening, in Figure 4.11 we also compare the titration curve with trivalent ions to the one with monovalent ions adjusted to the same ionic strength as the system with trivalent ions. Electrostatic screening in the monovalent case has only minor effect, as compared to the trivalent ions. Furthermore, Figure 6.6 shows that the shift of ionization caused by multivalent ions is unmatched by univalent ones even at four-times higher ionic strength. Finally, increasing the charge ratio of multivalent salt ξ leads to even more significant shift of ionization (see Figure 6.4).

In juxtaposition to the ionization, Figure 4.12 shows that the presence of multivalent ions causes the polymer to collapse, in spite of increasing its ionization. Anew, the comparison with monovalent salt at the same ionic strength, or even at higher ionic strengths in Figure 6.5, reveals that electrostatic screening has only a weak effect, and the observed collapse is the effect of valency. Figure 6.9 shows that in the limit of full ionization, our results are in agreement with the experiments by Mei *et. al.* [MLH$^+$06, MHBJ08] who followed the collapse of strong polyelectrolyte brushes in the presence of trivalent ions. We claim that the observed enhancement of ionization and the concomitant collapse of the polymer is a consequence of multivalency. Nonetheless, the precise mechanism of the effect is yet to be unfolded.

4.2.4 Quantifying the counterion accumulation

Examination of simulation snapshots (see Figure 4.13) suggests that valency of an ion strongly influences its distribution around the polymer. Multivalent counterions tend to be localized almost exclusively in the vicinity of charged segments of the star, while monovalent ones appear to be scattered in a larger volume. In Figure 4.14 we quantify the distributions in the form of concentration profiles of particles around the center of the star for the ionization $\alpha \approx 0.5$. As the distance from the star increases, monovalent ions follow a gradual decrease in concentration. Bulk concentration of monovalent ions is approximately of one order of magnitude lower in comparison with the concentration inside the star. Contrariwise, multivalent ions exhibit significantly higher difference between concentrations inside and outside the star. Importantly, the concentration of trivalent ions inside the star is more than four orders of magnitude higher as compared to the bulk concentration.

The ability of the polymer to accumulate multivalent ions was assessed in the form of partition coefficient, P_z, defined as

$$P_z = \frac{c_z^{\text{in}}}{c_z^{\text{out}}}, \tag{4.7}$$

where concentration inside the star, c_z^{in}, was computed as an integral of the concentration profile

$$c_z^{\text{in}} = \frac{1}{V^{\text{in}}} \int_0^{\langle R_{\text{ee}} \rangle} \mathrm{d}r \; 4\pi r^2 c(r), \tag{4.8}$$

and concentration outside the star, c_z^{out}, was calculated from c_z^{in} and the total ion concentration, c_z, as

$$c_z^{\text{out}} = \frac{1}{V^{\text{out}}} \left(c_z L^3 - c_z^{\text{in}} V^{\text{in}} \right), \tag{4.9}$$

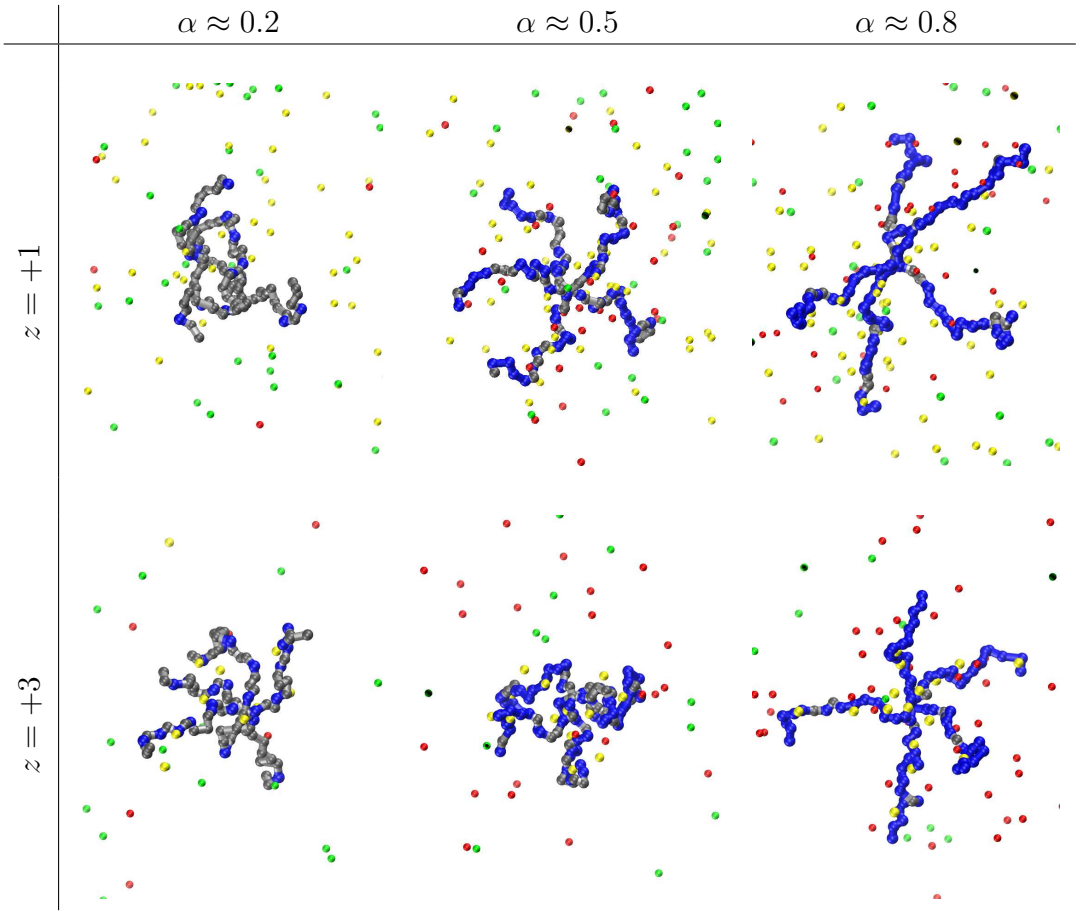

Figure 4.13: Simulation snapshots of star-like weak polyelectrolyte in the presence of trivalent and monovalent counterions at charge ratio $\xi = 0.50$. Color code: ionized monomer A^-, neutral monomer HA, H^+ counterions, M^{z+} counterions, Cl^- co-ions

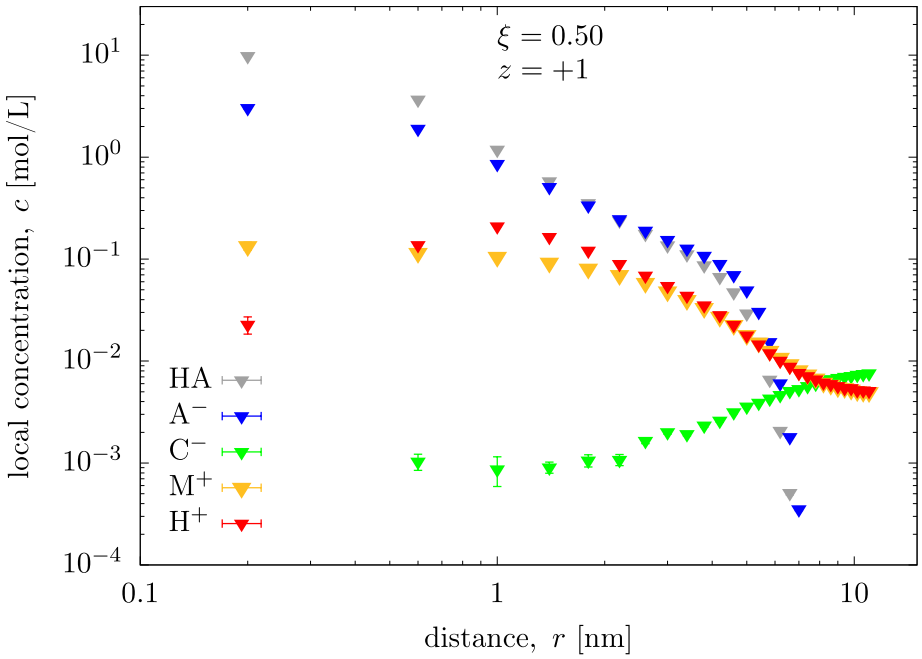

(a) Monovalent counterions.

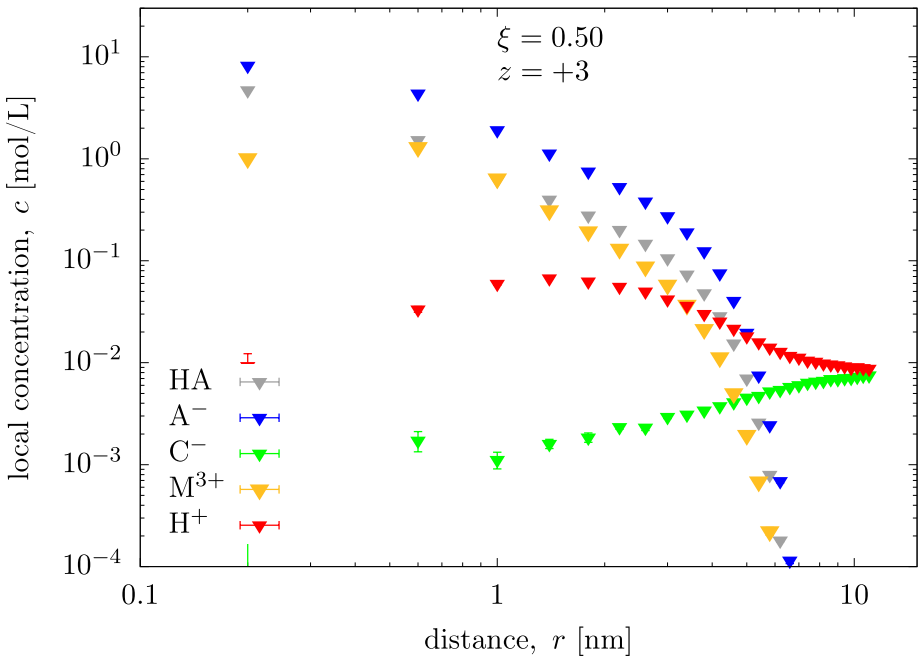

(b) Trivalent counterions.

Figure 4.14: Profiles of local concentration as a function of distance from the center of the star compared for systems $\xi = 0.50$ for different valencies of salt counterions.

where

$$V^{\text{in}} = \frac{4\pi\langle R_{\text{ee}}\rangle^3}{3} \qquad \text{and} \qquad V^{\text{out}} = L^3 - V^{\text{in}}. \tag{4.10}$$

Noticeably, a calculation of the partition coefficient requires an arbitrary choice for the threshold value separating the interior and exterior of the star – we used the average arm extension, $\langle R_{\text{ee}}\rangle$, as an intuitive length scale of separation. Nevertheless, we tested that different values of boundary threshold resulted in the same qualitative results.

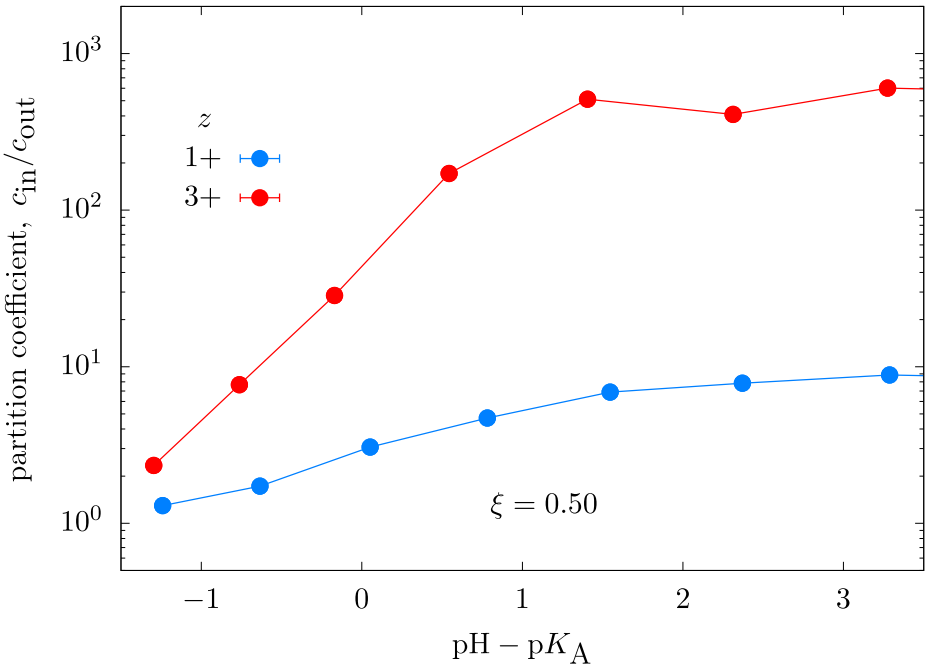

Figure 4.15: Partition coefficients of multivalent and monovalent ions at charge ratio $\xi = 0.50$.

The partition coefficient of monovalent ions is a steadily increasing function of pH − pK_{A}, while the partition coefficient of multivalent ions first increases, and then reaches a plateau in Figure 4.15. Qualitatively, the same observation can be made also for other ξ values (see Figure 6.8), however, the onset of the plateau appears at different values of pH − pK_{A}. Partition coefficients of trivalent ions are of the order of thousands which suggests that in the system of our size, all of the trivalent ions are effectively captured inside the star. To validate the latter claim, we present also mole fractions of ions inside the star in Figure 6.10. Comparing with titration curves, one can notice, that partition coefficient increases up to the point at which the total charge on trivalent ions inside the star is the same as the charge on the star ($\xi < \alpha$). The plateau is a manifestation of saturation and neutralization of the polymer by multivalent ions at $\xi \gtrsim \alpha$. Figure 4.16 shows that practically all trivalent ions are captured by the polymer when $\xi/\alpha \lesssim 1$, while monovalent ones are not quantitatively captured even if $\xi/\alpha \ll 1$. Trivalent ions escape the star only when $\xi > \alpha$, when the charge on the salt exceeds the charge on the polymer, suggesting that ξ/α is the key parameter controlling the ion accumulation.

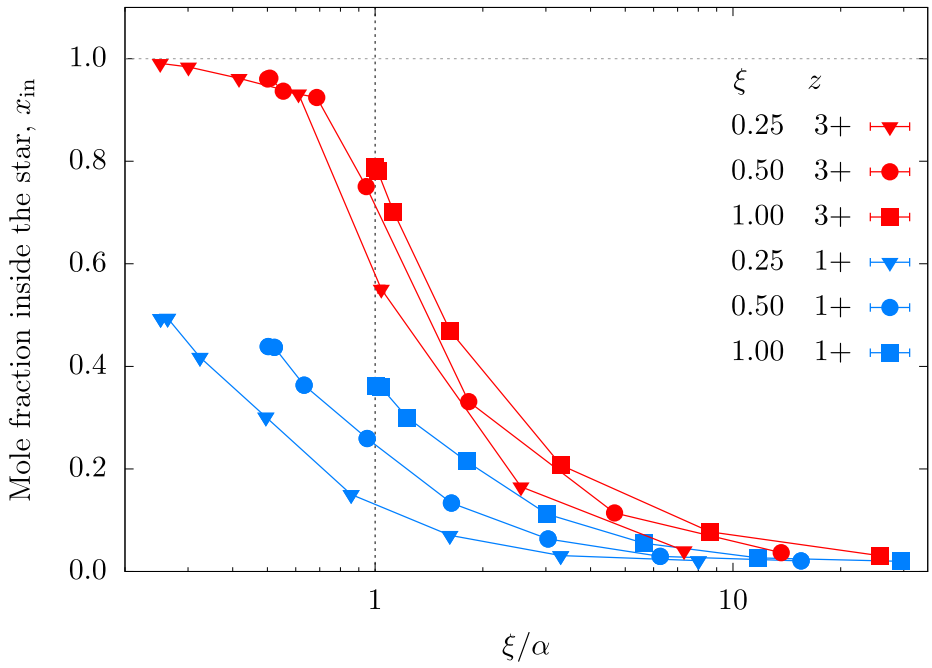

Figure 4.16: Dependence of mole ratio of ions inside the star on the ξ/α compared for different valencies and charge ratios.

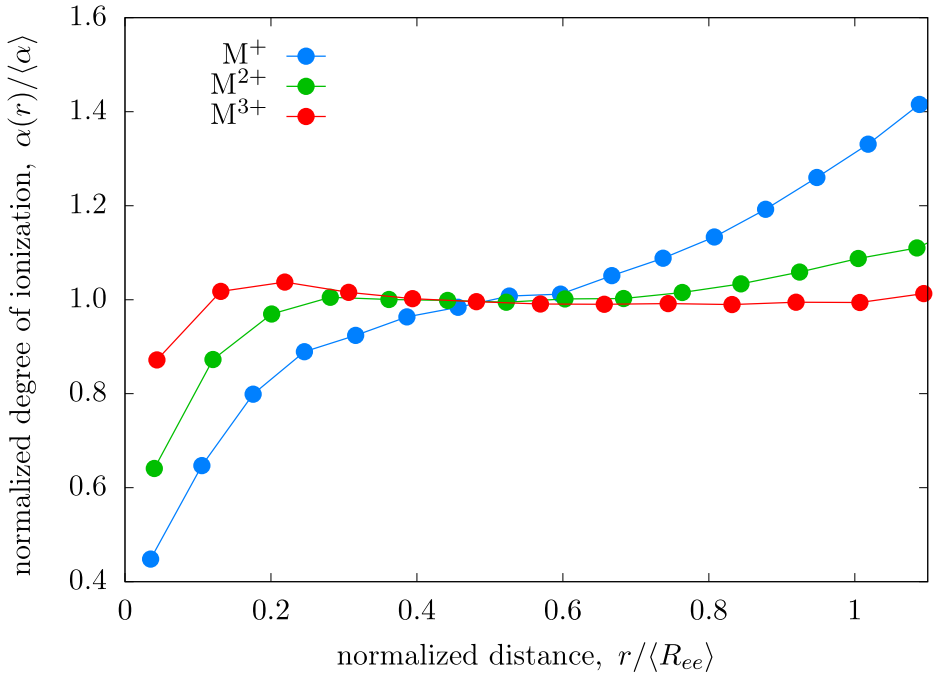

Figure 4.17: Ionization profile along the arm of the star at $\xi = 0.50$ at $\langle\alpha\rangle \sim 0.5$ compared for different valencies.

The interplay between ion accumulation and ionization can be further confirmed by probing ionization profiles along the arm as shown in Figure 4.17. In the case of monovalent ions, ionization in the center of the star is suppressed by strong repulsion between like-charged groups. On the other hand, the presence of multivalent ions enhances ionization in the center of the star, flattening the profiles in Figure 4.17 and simultaneously suppressing the repulsions between the like-charged groups. Therefore, accumulation of ions and local charge regulation comprise a positive-feedback loop.

4.2.5 Ion-ion correlations vs. Poisson-Boltzmann

We claim that the conjunction of enhanced ionization, collapse and ion accumulation is a consequence of strong ion-ion correlations. In the limit of weak coupling (weak correlations), the potential of mean force can be approximated by the averaged electrostatic potential. If that is the case, density profiles of ions should follow the Poisson-Boltzmann equation, which results in the distribution

$$c_i(r) \approx c_i(r \to \infty) \exp\left(-\frac{z_i \psi^{\text{el.}}(r)}{k_\text{B}T}\right), \tag{4.11}$$

where $\psi^{\text{el.}}(r)$ is the spherically averaged mean electrostatic potential and $c_i(r)$ is the concentration of ion i in the distance r from the center of the star. By plugging the definition of the potential of mean force, $w_i(r)$,

$$\frac{w_i(r)}{k_\text{B}T} = -\ln(g_i(r)), \tag{4.12}$$

into the mean-field result (4.11) we arrive at:

$$\frac{w_i(r)}{k_\text{B}T} = -\ln\left(\frac{c_i(r)}{\langle c_i \rangle}\right) \approx \frac{z_i \psi^{\text{el.}}(r)}{k_\text{B}T} \implies -\frac{1}{z_i}\ln\left(\frac{c_i(r)}{\langle c_i \rangle}\right) = \frac{\psi^{\text{el.}}(r)}{k_\text{B}T}. \tag{4.13}$$

Thus, if the mean field approximation is valid, then the potential of mean force normalized by the valency should yield the same $\psi^{\text{el.}}(r)$ regardless of the type of ion used in the calculation.

We tested the applicability of the mean-field assumption by calculating potentials of mean force of small ions and normalizing them by respective valencies. Figure 4.18a shows that all potentials of mean force for small monovalent ions result in the same function. Slight discrepancies between co-ions and counterions can be attributed to angular correlations – counterions tend to concentrate themselves around arms while co-ions occupy mainly the space between the arms. Overall, this justifies the use of mean-field approach for the system containing monovalent ions only.

However, Figure 4.18b shows a different trend – multivalent ions deviate very strongly from the monovalent ones, suggesting that the assumption of weak correlations is violated. Importantly, the difference in the potential of mean force between the interior and exterior of the star is $\sim 4k_\text{B}T$ per elementary charge for a trivalent ion. The difference for monovalent ions is $\sim 2k_\text{B}T$ – the disparity between the two can not be explained by mean-field and we attribute it to strong ion-ion correlations. Additionally, magnitude of the mean-field contribution to the potential of mean force is comparable to the correlation contribution.

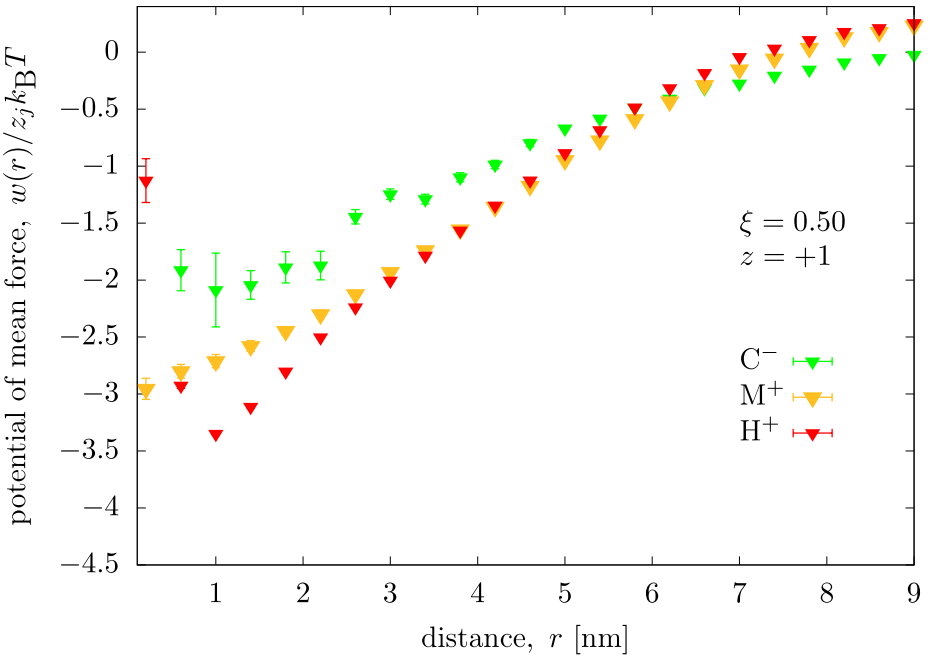

(a) Monovalent counterions.

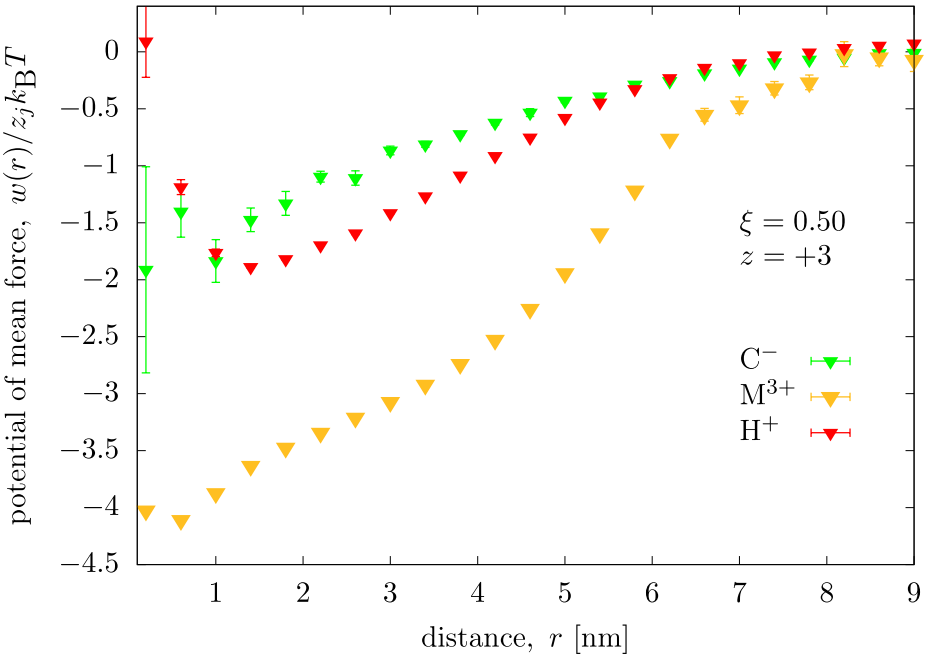

(b) Trivalent counterions.

Figure 4.18: Potentials of mean force for small ions as a function of distance from the center of the star compared for systems $\xi = 0.50$ for different valencies of salt counterions.

This means that neither the weak coupling, nor the strong coupling limit is applicable when dealing with weak polyelectrolytes and multivalent ions. The use of Poisson-Boltzmann equation yields a picture which is only qualitatively correct, predicting partition coefficients $\exp(3 \times (4-2)) \approx 400$-times lower when compared to the full treatment.

4.2.6 Conclusion

We used coarse-grained simulations in the reaction ensemble to explore the effect of multivalent salt on the ionization and conformations of a weak star-like polyelectrolyte. We showed that multivalent counterions significantly enhance ionization of the polymer, as opposed to monovalent ions at the same ionic strength. An apparent shift of the titration curve closer to the ideal one is caused by a cancellation of two highly non-ideal effects: First, the polyelectrolyte effect due to repulsion between like-charged segments on the polymer; Second, the attraction between multivalent ions and the polymer. The latter promotes the collapse of the polymer in spite of increasing its ionization, in contrast to monovalent ions which swell the polymer.

Multivalent ions accumulate inside the star more strongly than the monovalent ones. Furthermore, multivalent ions accumulate in the polymer up to the saturation of its charge, effectively neutralizing it. If the charge on polymer is higher as compared to the total charge on the all multivalent counterions, then the accumulation is almost quantitative, resulting in partition coefficients of the order of $\sim 10^2 - 10^3$.

Coupling of ionization and counterion accumulation comprises a positive feedback loop at pH $\approx$ pK_A, promoted by strong charge-charge correlations, as evidenced by disparities in potentials of mean force for mono- and multivalent ions. Finally, our work provides a fundamental understanding of interactions of multivalent ions and pH-responsive weak star-like polyelectrolytes, underlining the importance of full treatment of correlations in such systems.

4.3 Probing ionization response of peptides in the presence of DNA

The previous chapter provided an insight into the role of multivalency in the ionization of weak polyelectrolytes. However, addition of multivalent salt as a tool to control ionization seems rather impractical. Most of experimentally used small multivalent ions possess various ion specific effects beyond the resolution of our model. Furthermore, pH-dependent response interferes with a non-intuitive conformational change. Therefore, we designed a different but similar model system – we replaced small multivalent ions by long rigid strong polyelectrolytes, allowing us to decouple ionization and conformational responses. Complementary, we replaced the weak star-like polyelectrolyte with short linear weak polyelectrolytes. This setup grants us a higher flexibility with respect to experiments – tuning the length of short multivalent chain seems easier to realize than tuning the valency of a small ion. A possible experimental realization of such a model system is a solution of DNA with short oligopeptides such as polylysine, currently studied in our group.

4.3.1 Introduction

Interactions between oppositely charged polyelectrolytes in the dilute regime have been researched mainly in the connection to the gene delivery [BSHSK$^+$17]. Cationic polypeptides, but also polyethyleneimine (PEI) are used as non-viral vectors able to coordinate the DNA, providing it with a protection from enzyme degradation, and transfer it inside the cell. DNA can be subsequently released upon the change of pH in the cell environment. However, the ionization behaviour of common delivery vectors in the presence of DNA and without the presence of DNA is not very well understood. For example, a number of experimental studies investigated the degree of ionization of commonly used PEI at physiological pH $\sim$ 7.4 and reported values ranging from 10% to 90% [ZW10a]. Clearly, a better understanding of ionization response is needed.

Most of theoretical and computational studies were focused mainly on the structure of the DNA-polycation complexes, which has been researched even on the atomistic level [STUC20], however not accounting for variable ionization and charge distribution. The pH-dependent behaviour of polycation-polyanion complexes in dilute solutions has been partially described in a handful of coarse-grained simulations, which were concerned mainly with the effects of added salt [ZW10a, ZW10b], or driving forces of the complexation with respect to the pK_A [RSSW18]. Nevertheless, the above studies considered only long chains at stoichiometric ratio of polyanion to polycation.

In the current study, we explore the ionization behaviour of short weakly basic oligomers, representing peptides, in the presence of a rigid strong polyanion, representing DNA. In contrast to the above mentioned studies, we systematically vary the length of polycationic chains and ratio between the amount of DNA and peptides. We quantify the peptide accumulation on the DNA, and analyze the nano-heterogeneity of the ionization response.

4.3.2 Model and Method

We carried out coarse-grained simulations of linear weak polyelectrolytes in aqueous solutions in the presence of one strong polyelectrolyte chain and background salt. The strong polyelectrolyte, representing DNA, consisted of $N = 64$ negatively charged monomeric units. Weak linear polyelectrolytes representing the peptides were z monomeric units long, and each peptide monomer was modelled as a weak base defined by the acidity constant K_{A}, and could undergo an ionization reaction

$$\mathrm{BH}^+ \rightleftharpoons \mathrm{B} + \mathrm{H}^+. \tag{4.14}$$

The amount of weak polyelectrolyte in the solution was controlled via the charge ratio ξ, defined as $\xi = nz/N$, where n is the number of peptide chains, similarly to Section 4.2. We carried out simulations for $\xi \in \{0.50, 1.00, 2.00\}$ and $z \in \{1, 2, 4, 8\}$. To give an example, system with $\xi = 0.50$ and $z = 4$ consists of one DNA molecule with $N = 64$ segments and $n = 8$ peptide chains of length $z = 4$. Ions of the background uni-univalent salt were modelled explicitly with the total concentration $c_{\mathrm{NaCl}} = 5$ mM. For each of the simulated systems, we carried out also a reference simulation, in which the DNA was not present, while the amount of peptide and salt was kept the same.

Polymer connectivity was represented by FENE bonds with stiffness constant $k = 30k_{\mathrm{B}}T/\sigma^2$, offset $r_0 = 0$ and maximal extension $r_{\max} = 1.5\sigma$ following the same notation as in (3.8). To assure rigidity of the DNA chain, we added harmonic bond-angle potential with stiffness $20k_{\mathrm{B}}T/\mathrm{rad}^2$ and equilibrium angle $\pi \equiv 180°$. Excluded volume interaction between each pair of particles were purely repulsive (good solvent). Specifically, we used WCA potential with $\varepsilon_{\mathrm{WCA}} = 1k_{\mathrm{B}}T$, and $\sigma = 0.355$ nm. Finally, charged species interacted with Coulomb potential with $l_{\mathrm{B}} = 2\sigma = 0.710$ nm, matching that of aqueous solution at room temperature. Calculation of electrostatic forces employed the $\mathrm{P}^3\mathrm{M}$ method. The size of the simulation cell was $L \approx 133\sigma \approx 47$ nm, resulting in the concentration of DNA monomers $c_{\mathrm{mon}} \approx 1$ mM, approximately corresponding to 0.5 g/L.

To address the variable ionization, we used the Constant-pH ensemble method in the form presented in Subsection 2.4.1 with probability criterion (2.22). For each system, we carried out independent simulations at pH $\in \{3.0$, 3.5, 4.0 . . . , 8.5, 9.0$\}$ with $\mathrm{p}K_{\mathrm{A}} = 7$. The ionic strength in the system was dominated by the background salt at $\mathrm{p}I \approx 1.30$, and thus the choice of the $\mathrm{p}K_{\mathrm{A}}$ value was arbitrary – the only relevant control parameter is $\mathrm{pH} - \mathrm{p}K_{\mathrm{A}}$ (see Section 2.4). Conformational space was sampled by Langevin dynamics with time-step $\Delta t = 0.01\tau$. A typical simulation run was $\sim 10^5\tau$ Langevin dynamics steps long and consisted of $\sim 10^7$ Constant-pH MC reaction trials.

4.3.3 Interaction with the DNA strongly enhances ionization of peptides

In Figure 4.19 we compare titration curves of peptides in the presence of DNA and in solution without DNA. Titration curves for $N = 1$ agree very well with the ideal titration curve, and we see virtually no difference between the solution with and without DNA. For $N \geq 2$, we see that ionization of the peptide without the DNA is suppressed with respect to the Henderson-Hasselbalch equation, because

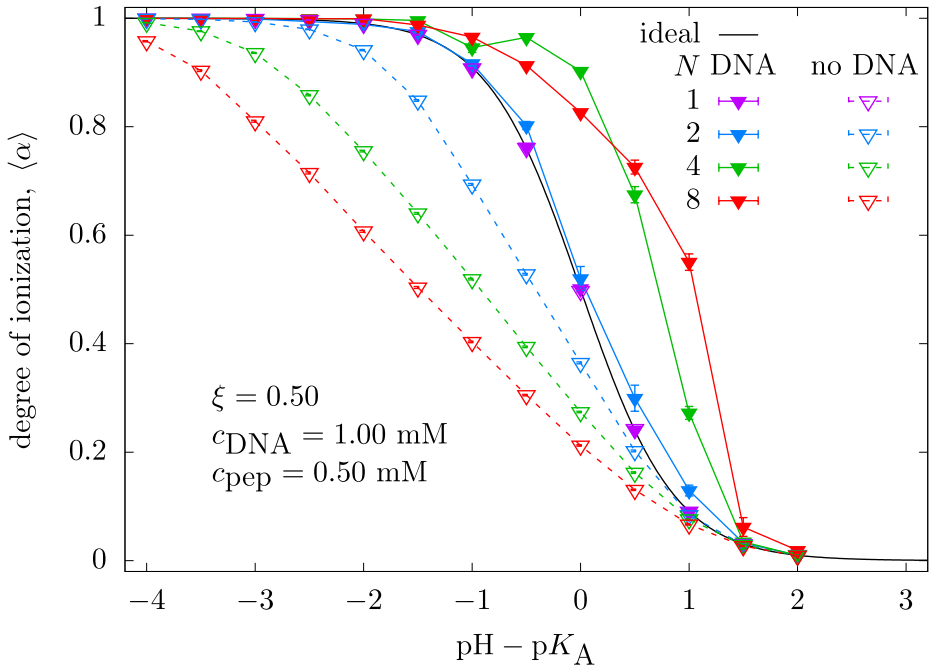

Figure 4.19: Titration curves of peptides of various lengths in solutions with or without the DNA. Charge ratio is $\xi = 0.50$.

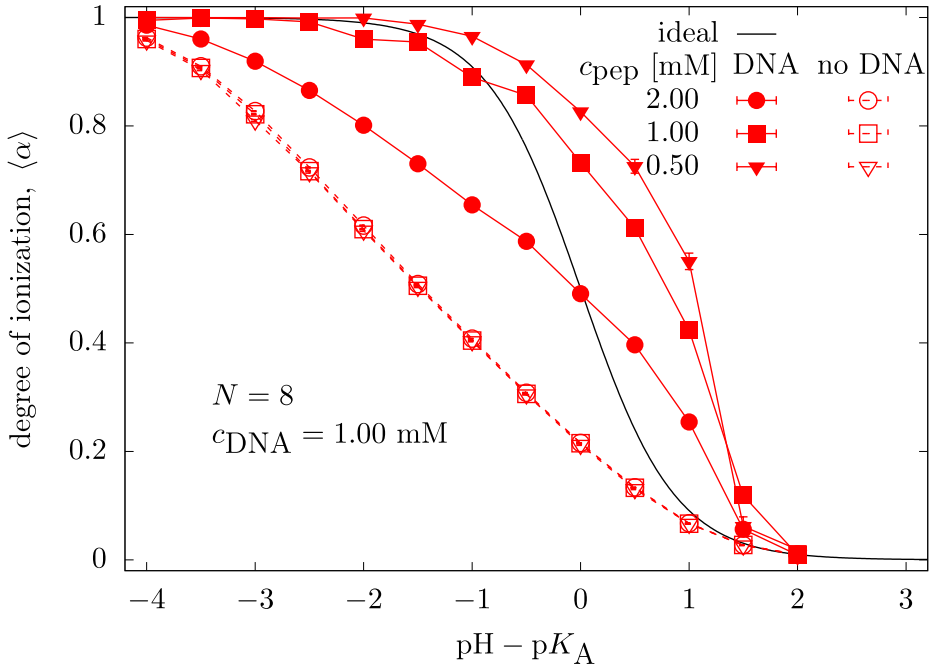

Figure 4.20: Titration curves of peptides of length $N = 8$ in solutions with or without the DNA for different charge ratios.

of the polyelectrolyte effect. The shift to the lower ionization increases with length of the peptide, qualitatively reproducing the results from Figure 1.4. In contrast, presence of the DNA chain significantly increases peptide ionization. In such case, the degree of ionization is even higher than that predicted by the Henderson-Hasselbalch equation, suggesting that the polyelectrolyte effect is effectively overridden by interaction of the peptide with the DNA. We also notice that in the presence of DNA, the peptide ionization increases with N, as opposed to the response without the DNA, when it decreases with N. The observed effect is a direct consequence of the direct interaction of the peptides and the oppositely charges DNA chain.

A comparison of titration curves at different charge ratios in Figure 4.20 for $N = 8$ and also Figure 6.11 and Figure 6.12 for $N \leq 4$ supports the hypothesis that the DNA interacts with peptides directly. Peptide ionization without the DNA is almost independent of the peptide concentration. On the contrary, a strong dependence on peptide concentration is observed upon addition of the DNA. Furthermore, titration curves at $\xi = 0.50$ and $\xi = 1.00$ have similar qualitative course, and exhibit a strong shift as compared to their counterparts without the DNA. Notably, the difference in the effective $\mathrm{p}K_\mathrm{A}$ of the peptides with and without DNA is more than two units of pH. However, this shift is significantly weaker at $\xi = 2.00$, when the peptide is in excess with respect to the DNA. This is because at $\xi > 1.00$, the DNA is fully saturated with a stoichiometric fraction of condensed peptides, which decreases the influence of the DNA on the remaining peptides. When compared to the ideal titration curve, the peptide ionization at $\xi = 2.00$ is increased at $\mathrm{pH} - \mathrm{p}K_\mathrm{A} > 0$ and suppressed at $\mathrm{pH} - \mathrm{p}K_\mathrm{A} < 0$. Incidentally, at $\mathrm{pH} - \mathrm{p}K_\mathrm{A} = 0.0$ peptide attains the ionization predicted by the Henderson-Hasselbalch equation. Nonetheless, this effect in only a result of cancellation of strongly non-ideal effects, as we will explain shortly.

4.3.4 Peptides mightily condense on the DNA

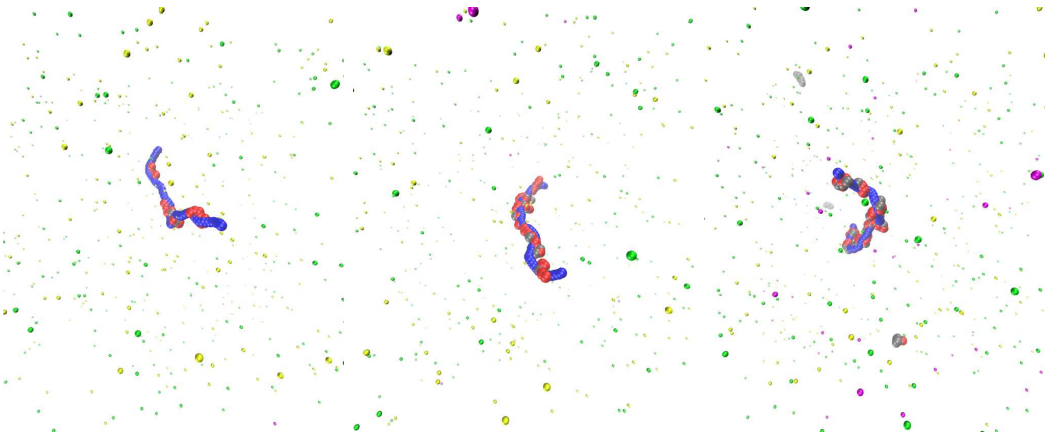

(a) $\xi = 0.50$ (b) $\xi = 1.00$ (c) $\xi = 2.00$

Figure 4.21: Simulation snapshots of the DNA with peptides of length $N = 8$ at $\mathrm{pH} - \mathrm{p}K_\mathrm{A} = 0.0$ at various charge ratios. Color code: peptide monomer BH^+, peptide monomer B, DNA monomer A^-, Na^+ ions, Cl^- ions, H^+ ions,

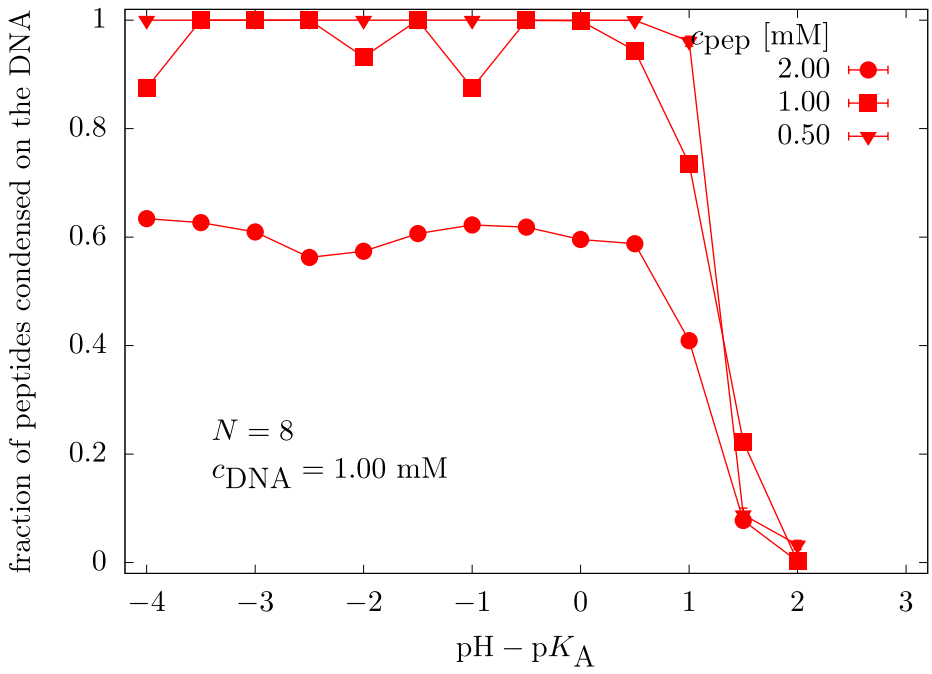

Figure 4.22: Mole fractions of peptides *condensed* on the DNA as a function of $\mathrm{pH} - \mathrm{p}K_\mathrm{A}$ for peptides of length $N = 8$ at various charge ratios.

An inspection of simulation snapshots in Figure 4.21 reveals that ionization of peptides is coupled to their localization in the vicinity of DNA. To make a connection to Section 4.2, the peptide ionization response is coupled to their localization at the DNA in a similar way as the ionization of star-like polymer was coupled to the localization of trivalent ions. To quantify the accumulation of peptide at the DNA chain, we calculated mole fractions of peptides *condensed* on the chain. We defined a peptide as condensed if it contains such a monomeric unit that its distance to the closest DNA segment is less than the threshold $2\sigma = l_\mathrm{B}$. The criterion was chosen arbitrarily, however the trends in the results were the same also for other similar values of the threshold. Figure 4.22, shows that at $\xi \leq 1.00$, practically all peptides of length $N = 8$ are condensed on the DNA chain if $\mathrm{pH} - \mathrm{p}K_\mathrm{A} < 1.0$, and they are able to escape only at $\mathrm{pH} \gg \mathrm{p}K_\mathrm{A}$. Similar to trivalent ions in Section 4.2, a plateau in mole fractions of condensed peptides as a function $\mathrm{pH} - \mathrm{p}K_\mathrm{A}$ is a sign of saturation of the DNA by peptides – this is observable for peptides of length $N \geq 2$ in Figure 6.13. However, the onset of the plateau shifts to lower values of $\mathrm{pH} - \mathrm{p}K_\mathrm{A}$ as N increases. This is expected even on the level of Manning theory, since the condensation threshold for counterions scales as $\sim 1/z$, where z is the valency of a simple counterion. Furthermore, Figure 6.13 and Figure 6.14 show that the fraction of condensed peptides increases with peptide length in the whole range of $\mathrm{pH} - \mathrm{p}K_\mathrm{A}$ and ξ. Lastly, we briefly comment on the apparent irregular trend in Figure 4.22 and Figure 6.13 for $N = 8$ at $\xi = 1.00$. There is no physical reason for oscillations in mole fractions of condensed peptides, and we suspect that data points not obeying the trend might be undersampled. In most of simulations for $N \leq 4$, we were able to observe repeated condensation and decondensation of peptides in the simulations. However, at $N = 8$, the peptides condense on the chain so

strongly, that decondensation of peptides at some pH values was not observed in the whole length of the simulations. We expect that running longer simulations in the future will correct the results.

Finally, fractions of condensed and free peptides at $\xi = 2.00$ are comparable in magnitude. Roughly one half of peptides is strongly coupled on the DNA, effectively neutralizing its charge, while the other half is free in the solution. However, how the DNA affects the peptides which are not directly condensed on it is yet to be explored.

4.3.5 Peptides co-exist in two different states

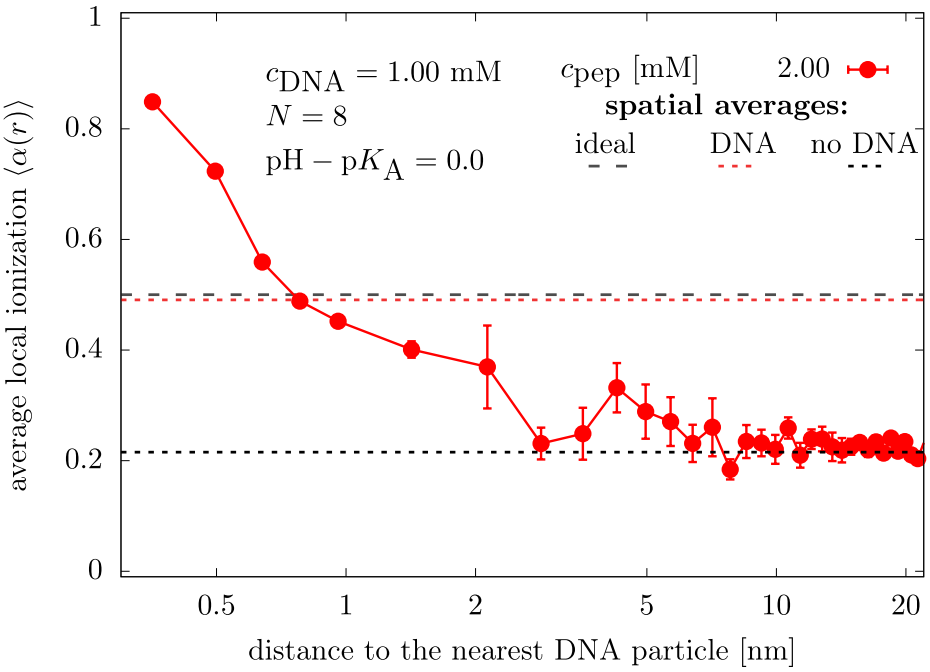

Figure 4.23: Profile of ionization of a peptide of length $N = 8$ as a function of the distance to the nearest DNA particle. Dashed red and black lines show the mean degree of ionization averaged over all peptide in the respective simulation box. Dashed gray line is $\alpha = 1/2$ as predicted by the Henderson-Hasselbalch equation. Charge ratio $\xi = 2.00$ and $\mathrm{pH} - \mathrm{p}K_{\mathrm{A}} = 0.0$.

In Figure 4.23 we show the degree of ionization as a function of the distance of the peptides from the nearest DNA segment. We observe that peptides in the vicinity of DNA ($r \lesssim 1\mathrm{nm} \approx 1.5 l_{\mathrm{B}}$) are highly ionized on average. As their distance from the DNA increases, the peptide ionization decreases. At distances $r \gtrsim 7\mathrm{nm} \approx 10 l_{\mathrm{B}}$ peptides attain their bulk ionization (dashed black line), and behave as if the DNA was not present, confirming that it is effectively neutralized by the condensed peptides. Furthermore, the probability distribution of peptide ionization in Figure 4.24 exhibits two maxima, showing peptides co-exist mainly in two different states. The presence of DNA thus introduces a nano-heterogeneity of ionization response of the peptides. Highly ionized peptides in the vicinity of the DNA co-exist with weakly ionized ones far from the DNA. The fact that total ionization $\langle\alpha\rangle \approx 0.5$ agrees with the Henderson-Hasselbalch equation at $\xi = 2.00$

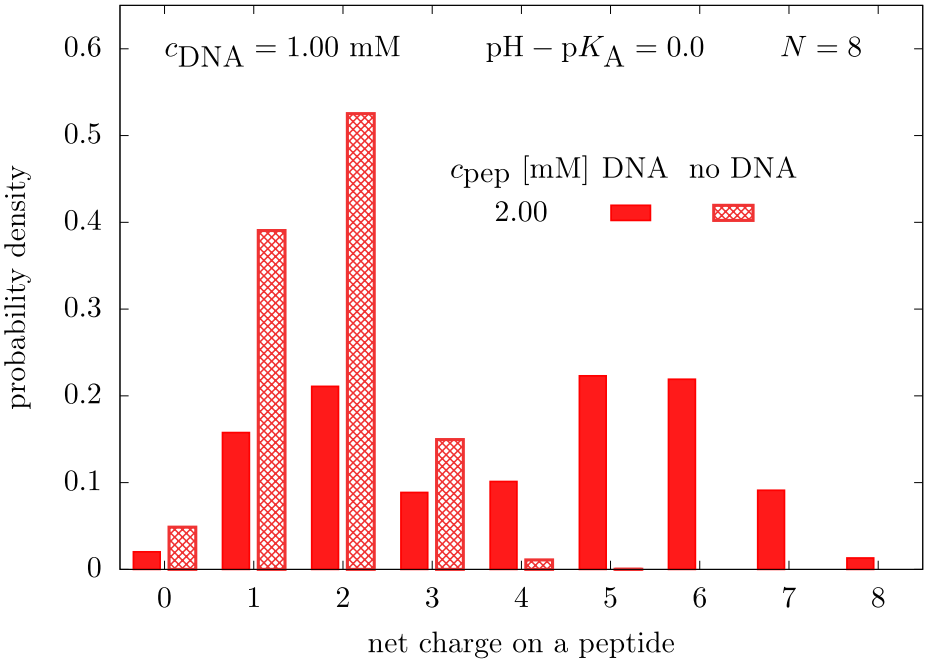

Figure 4.24: Probability distribution of observing a specific ionization state of a peptide of length $N = 8$ with and without DNA present. Charge ratio $\xi = 2.00$ and $\mathrm{pH} - \mathrm{p}K_{\mathrm{A}} = 0.0$.

should be by no means interpreted as if the system became ideal in its behaviour. On the contrary, the observed average ionization is a result of averaging over two extreme states: First, highly ionized peptides in the proximity of the DNA, stabilized by strong ion-ion correlations and counterion release; Second, weakly ionized peptides far from the DNA with ionization suppressed due to the polyelectrolyte effect.

4.3.6 Conclusion and outlook

We carried out coarse-grained simulations of short weakly basic oligopeptides in aqueous salt solution in the presence of a quenched rod-like polyelectrolyte representing DNA chain. We found out that the presence of the DNA strongly promotes ionization of the peptides, as compared to the solution of peptides without DNA. The DNA stabilizes highly charged peptides by creating an interpolyelectrolyte complex with them, up to the saturation of the DNA charge. The resulting interaction between the oppositely charged chains effectively over-rides the repulsions between the like charged peptide segments, and enhances their ionization far beyond the ionization predicted by the Henderson-Hasselbalch equation. Promotion of the ionization is in its nature local, thus introducing a nano-heterogeneity in the ionization response. At $\mathrm{pH} \approx \mathrm{p}K_{\mathrm{A}}$, highly ionized peptides are found almost exclusively in the vicinity of the DNA, and they co-exist with weakly ionized peptides far from the DNA.

We surmise that the observed effect suggest a possible use of DNA chains as nanobuffers for peptides [NMV+09, AZG+19]. The steepness of the titration curve for peptides of $N = 8$ in Figure 4.20 is a manifestation of the "proton-sponge"

effect. The transition between the free neutral peptide and the condensed ionized peptide occurs in a very narrow region of pH, in which the peptide acts as a high capacity buffer – an addition of acid to the solution does not decreases the pH, but rather charges up the peptides. The titration curves obtained by the constant-pH method correspond to experiment, in which we would measure ionization at pH values controlled by a high capacity buffer. We hypothesize that if the simulation or the experiment was carried out by step-wise addition of acid to the DNA-peptide solution without any buffer present, the dependence of measured pH on the added volume of acid would be approximately constant. On the contrary, weakly acidic peptides without the DNA act as a low capacity buffer in a broad range of pH. In contrast, the peptides in the presence of DNA act as a high capacity buffer, but in a very narrow range of pH. The working range and the capacity of such a buffer can be presumably tuned by the length of the oligomer chain and also by the aminoacid sequence on the peptide. Subsequently, the buffering properties can be controlled by a small addition of the DNA.

Recently, we established an experimental protocol [LMH^+] allowing us to measure ionization of peptides in their dilute solution by a combination of electrophoresis, NMR and potentiometric titration. Currently, we are planning to carry out experiments on lysine oligopeptides interacting with the DNA to test the predictive capability of our simulations. On the theory side, we plan to improve our coarse-grained model to better capture the nature of specific aminoacids. Additionally, we plan to extend the work towards peptides with different sequences of monomeric units with different pK_A values.

4.4 Electrostatically cross-linked reversible gels controlled by pH

Herein, we make use of the principles from the preceding section to provide simple design rules for preparation of pH-responsive hydrogels. We demonstrate the strength of the Grand-reaction method in a simulation of the two-phase equilibrium of a non-covalent ionic gel coupled to the reservoir. We show how the Grand-reaction method allows us to separate the Donnan effect from the polyelectrolyte effect and compare their contributions to the ionization. As mentioned in the foreword of Chapter 2, simulations are usually used to either test theories used to interpret experiments, or to predict the behaviour of experimental systems. The works from the preceding sections falls in the former category. In this section however, we try to use modelling to predict certain features of behaviour of experimental systems, which are being investigated simultaneously with our simulations. Thus, our simulations provide a guideline which is immediately used in experiment.

4.4.1 Introduction

Hydrogels are promising candidates for a myriad of applications such as drug delivery systems [JBLK97, KACD13] or responsive biomaterials [NBP$^+$02, Man08]. Hydrogels consist of cross-linked polymer chains forming a 3D network replete with water. A variety of synthetic routes enables to prepare covalently cross-linked hydrogels with a high precision. Chemically cross-linked hydrogels exhibit mechanical strength, however their structure can be hardly altered after the synthesis. Furthermore, covalent cross-links usually can not be reformed if broken, diminishing self-healing properties of the gels [PG03, AdBLS12]. Last but not least, covalent hydrogels are typically non-injectable and not biocompatible, complicating their utilization in living systems [KLC$^+$13].

In contrast to chemical gels, physical hydrogels formed by non-covalent interactions are often reversible, self-healing, biocompatible and injectable, and therefore more suitable for bioapplications [KLC$^+$13]. However, the transient nature of physical cross-links weakens the gel, making it more susceptible to shearing [VBvSH06, HFL$^+$11, WMY$^+$10]. Nevertheless, the non-covalent character of physical cross-links brings a prospect of new forms of responsiveness.

Presumably the most popular motif present in the preparation of physical hydrogels uses amphiphilic block copolymers composed of hydrophilic and hydrophobic blocks [VH16, AdBLS12, Pat20]. In aqueous environments, hydrophobic blocks create collapsed domains, forming gel nodal points, connected by stretched hydrophilic blocks. The structure of such amphiphilic copolymer networks is defined by the architecture of polymers, and can be further controlled by solvent quality or temperature. However, changing the temperature or solvent quality in biological system is often inaccessible – it is desirable to have a different control mechanism.

Replacing hydrophobic blocks of amphiphilic copolymers by oppositely charged polyelectrolyte sequences also results in the formation of a physical gel, driven by coacervation rather than hydrophobic effect [CSHVdK05, YDF$^+$14]. Such block copolymers are usually well soluble, biocompatible, and their complexation-driven

self-assembly can be controled via ionic strength or pH if the polyelectrolyte groups are weak [LSV$^+$10, HFL$^+$11]. Additionally, in contrast to hydrophobic polymers, coacervate domains are polar with high water content, allowing to use them for encapsulation and delivery of charged solutes such as proteins or nucleic acids. Experimental preparation of electrostatically cross-linked gels is often based on mixing triblock copolymers of type ABA, where B is a neutral hydrophilic block, and A is either positively or negatively charged polyelectrolyte [KLC$^+$13, LSV$^+$10, HFL$^+$11, DSP$^+$14, DBK$^+$15]. However, the formation and structure of the gel strongly depend not only on architecture of the building blocks, but also on the total polymer and salt content. Possible structures of the resulting assemblies encompass a dilute polyelectrolyte solution, a dilute phase of flower-like micelles, disordered gels, but also ordered gels [SAL$^+$17]. Presumably, a higher control of the structure of the gel could be reached by controlling the architecture of the building blocks.

Naturally, microstructure and topology of constituents affect the macrostructure and nanostructure of self-assemblies. For example, Sakai *et. al.* prepared tetrahedral 4-arm star-like polymers with telechelic termini, which upon chemical reactions between the termini formed a gel with an almost ideal diamond structure [SMY$^+$08]. In recent years, there has been a surge in synthesis of gels derived from the ensemble of Sakai *et. al.* [SLS19, FAU$^+$12, OFMM14], however all of these gels are covalent gels with very limited self-healing properties. Researchers of the project FOR2811 [FOR] proposed that assembly of 4-arm star-like hydrophilic polymers terminated by short polyelectrolyte sequences should yield a gel with a well-defined structure derived from the covalent diamond structure combined with the responsiveness and self-healing properties of non-covalent gels. To verify this concept, the group of Felix Schacher recently synthesized star-like polymers composed of pentaerythritol core and four arms composed of 55 units of polyethylene glycol (PEG) each. The ends of the arms of these stars were subsequently functionalized by two different polyelectrolyte blocks: strongly cationic block of quaternized poly[2-(dimethylamino)ethyl methylacrylate] (PDMAEMA); weak ampholytic blocks of polydehydroalanine (PDha). A monomeric unit of PDha bears a amino- and a carboxylic group, implying that PDha is charged positively at pH $\lesssim$ 2, negatively at 9 $\lesssim$ pH and neutral at 2 $\lesssim$ pH $\lesssim$ 9. Ampholytic nature of PDha makes it a common choice for building blocks in the design of pH-responsive materials [MMTS20, MKK$^+$20]. Supposedly, mixing of PDMAEMA stars with PDha stars at low pH should result in a solution of positively charged stars. However, increasing the pH should progressively charge the PDha negatively, inducing the assembly with cationic PDMAEMA stars, potentially resulting in the formation of a pH-responsive hydrogel.

The main aim of this work is to employ coarse-grained simulations to find out whether an ensemble of anionic and cationic stars can form a reversible gel, and how the charge-driven assembly depends on the pH and ionic strength of the solution. This work was done within FOR2811 [FOR] collaborative project, during the internship of the author of this thesis in the group of Christian Holm at Institute for Computational Physics at University of Stuttgart.

There are many theoretical or computational studies of covalent gels (see Section 1.5), however simulation studies of non-covalent copolymer networks are very rare, and usually use mean-field approaches or scaling theories [PG03]. Very re-

cently, a significant progress has been made in modelling of complex coacervates (see Section 4.1 and Section 1.6), however instances of molecular simulations of coacervation-driven gels are not so common. Srivastava *et. al.* [SAL$^+$17] and Dyakonova *et. al.* [DBK$^+$15] employed molecular simulations to study the assembly of linear copolymers, however containing strong polyelectrolyte blocks, thus not incorporating the effects of pH and variable ionization. Furthermore, the two above mentioned studies were concerned mainly with the structural properties, and did not explore reversibility of the gel. In Section 4.2, we reviewed some literature on simulations of weak polyelectrolytes, however almost all of the studies regarded systems composed of either polyanions or polycations in dilute solutions. Our work is conceivably the first simulation study of the formation of a electrostatic gel composed of weak polyelectrolytes, where we directly account for ionization equilibria and the effect of pH.

The studied system is derived from the preceding study of Tagliabue *et. al.* [TLMH], who provided the proof of concept that oppositely charged star-like strong polyelectrolytes indeed form a percolating network. However, this preliminary work regarded only stars with arms composed of 10 monomers in total, where the last $2-5$ monomers were charged. We extend this work in three aspects relevant for experiments, which are being conducted in the group of Felix Schacher in parallel to our simulations:

1. **prolongation of the arms of the stars as compared to** Ref. [TLMH]**:** the arms of stars used in experiments are ~ 60 monomers in contrast to 10 used in Ref. [TLMH]. The loss of conformational entropy of the arms upon formation a cross-link increases with the length of arms. Increasing the length of the arms should therefore act against the formation of the gel, however the magnitude of this effect is not *a priori* known.

2. **inclusion of salt:** Presumably the greatest simplification in the work of Tagliabue *et. al.* with respect to the experiments is the complete neglect of the presence of counterions. An increase in salt concentration suppresses the formation of interpolyelectrolyte complexes by means of excluded-volume repulsions and electrostatic screening.

3. **inclusion of pH:** Finally, we consider that anionic monomers are weakly acidic, and their average charge depends on the pH.

In the following subsections we describe the model and method used in the simulations, and then report on the formation of ionic gel. In a systematic fashion, we discuss effects of the pH and ionic strength on the equilibrium composition of the gel, structural properties, and reversibility of the gelation.

4.4.2 Model and Method

We carried out coarse-grained simulations of an ensemble of star-like polyelectrolytes in a system coupled to an external reservoir. The system contained 32 cationic and 32 anionic stars. Each star consisted of 4 identical arms attached to a central segment. Each arm was composed of 25 neutral segments followed by a sequence of $n = 5$ *terminal segments*. Each arm of a cationic star was terminated

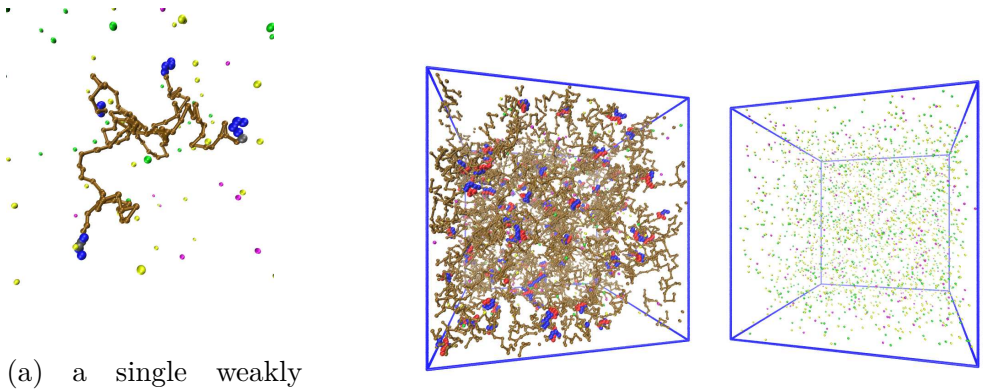

(a) a single weakly acidic star in a dilute solution

(b) gel of stars coupled to the reservoir

Figure 4.25: Snapshots of a free star in a dilute solution at $\mathrm{pH}^{\mathrm{res}}$ and of a gel phase and auxiliary reservoir at $I^{\mathrm{res}} \approx 17.5$ mM and $\mathrm{pH}^{\mathrm{res}} \approx 11.87$.
Color code: ionized acidic segments, A^-, neutral acidic segments, HA, basic segments BH^+, neutral PEG segments, Na^+ ions, Cl^- ions, OH^- ions,

by $n = 5$ strong (quenched) polyelectrolyte segments of charge $z = +1$, thus creating a star with a total charge $+20$. Each arm of an anionic star was terminated by $n = 5$ weakly acidic (annealed) segments with acidity constant, $K_{\mathrm{A}} = 9.87$, corresponding to the $\mathrm{p}K_{\mathrm{A}}$ value of alanine. The anionic segments can undergo the ionization reaction

$$\mathrm{HA} \rightleftharpoons \mathrm{A}^- + \mathrm{H}^+, \tag{4.15}$$

and thus bear a charge either $z = 0$ or $z = -1$, resulting in an anionic star with a net charge totaling from 0 to -20. To be able to separate the effects of pH, and electrostatic screening, we carried out simulations with quenched anionic stars as well. In this case, the anionic star permanently bears a net charge -20, which can be perceived as a limiting case of the annealed star, where $K_{\mathrm{A}} \to \infty$. Typical box sizes were $L \approx 70\sigma \approx 25$ nm, resulting in monomer molarity in the range $\sim 0.5\mathrm{M} - 1.0\mathrm{M}$ in the system. Figure 4.25 shows snapshots of a single anionic star in a dilute solution, and the gel of stars with reservoir.

The bonds including at least one of *terminal segments* were modelled with FENE potential with stiffness constant $k_r = 30k_{\mathrm{B}}T/\sigma^2$, equilibrium distance $r_0 = 0$ and maximum extension $r_{\max} = 1.5\sigma$. The bonds between neutral segments were modelled as harmonic springs with stiffness constant $k_b = 30k_{\mathrm{B}}T/\sigma^2$ and equilibrium length $b_0 = 2\sigma$ where $\sigma = 0.355$ nm. This makes the bonds between neutral segments softer and more extensible, with respect to the ones connecting charged segments. Additionally, each pair of particles interacted through the WCA interaction with $\varepsilon = 1k_{\mathrm{B}}T$ corresponding to a good (athermal) solvent. Finally, charged particles interacted with full Coulomb potential with Bjerrum length $l_{\mathrm{B}} = 2\sigma = 0.710$ nm approximately corresponding to the permittivity of aqueous solutions at temperature $T = 298$ K. The solvent was treated as an implicit dielectric continuum, omitting its molecular structure.

The system was coupled to a reservoir via the Grand-reaction ensemble method. The gel of annealed stars was coupled to a reservoir containing Na^+, Cl^-, H^+ and

OH^-, which was defined by $c^{\text{res}}_{\text{NaCl}}$ and pH^{res}. We carried out simulations of reservoirs at the pH $\in [8.9, 11.9]$, with added NaCl resulting in ionic strengths in the range $I \in [13.2\text{ mM}, 17.5\text{ mM}]$. The gel of quenched stars was coupled to a reservoir containing Na^+ and Cl^- defined by $c^{\text{res}}_{\text{NaCl}} \in [4.0\text{ mM}, 531\text{ mM}]$. Quenched stars do not participate in any ionization equilibrium, and since all small ions have the same interaction parameters, the addition of H^+ or OH^- has the same effect as the addition of Na^+ or Cl^-, respectively. Therefore, we can neglect the presence of H^+ and OH^- in the reservoir, which is then completely defined by $c^{\text{res}}_{\text{NaCl}} \equiv I$.

We used Langevin dynamics to sample the conformational space, in addition to Grand-reaction MC exchanges and reactions sampling the composition. We carried out two sets of simulations of the system: First, single point calculations for Pc protocol the same as in Subsection 4.1.3 to find the phase equilibrium for a specific choice of the coupled reservoir; Second, the production runs in the phase equilibrium. The former were $10^5\tau$ long with 10^7 LD integration steps and $2 \cdot 10^6$ MC trials for reactions and ionic exchange. The latter were $4 \cdot 10^5\tau$ long with $4 \cdot 10^7$ LD integration steps and $8 \cdot 10^6$ MC trials for reactions and ionic exchange.

Finally, we comment on the model in the context of related experiments. Our collaborators in the group of Prof. Felix Schacher synthesized 4-arm stars with exactly 55 neutral hydrophilic PEG monomers per arm. Ends of the arms were subsequently functionalized by a block of terminal segments. In the case of cationic stars, with a block of 5 quarternized PDMAEMA units. In the case of anionic stars, the synthesis yielded a polydisperse sample with PDha termini ranging from 3 to 7 units in length.

In our simulations, we decided to lower the number of PEG segments from 55 to 25, prolonging the bonds between them, and making them softer. This reduces the number of particles in the box roughly two-times, reducing the computational cost. In the presented results, the choice of interaction parameters for bonds was arbitrary, however we plan to tune the force constants to match the gyration radius of experimentally prepared stars. Another simplification with respect to the experiment, is that in the simulations, all anionic blocks are 5 segments long. Finally, the choice of K_{A} is based on the value measured for alanine, which is structurally very similar to a single PDha monomeric unit, used in the experiments.

4.4.3 Quenched stars form a dense phase

We begin by exploring the system where both anionic and cationic stars are quenched. In Figure 4.26 we present pressure-concentration (Pc) curves for a system of stars coupled to reservoirs with different salt concentration. First, we observe that sufficiently high salt concentration ($c^{\text{res}}_{\text{NaCl}} \sim 530$ mM) does not results in the formation of a separate phase of stars that would be in equilibrium with the reservoir. Similar to interpolyelectrolyte complexes in Chapter 4.1, it is a combination of two main effects: Firstly, strong electrostatic screening which suppresses the formation of polycation-polyanion complexes; Secondly, the prevalence of excluded-volume repulsions with respect to electrostatic attractions, as a results of high density of species in the system. However, the Pc-curve for $c^{\text{res}}_{\text{NaCl}} \sim 317$ mM intersects the zero-pressure line, indicating that stars form a

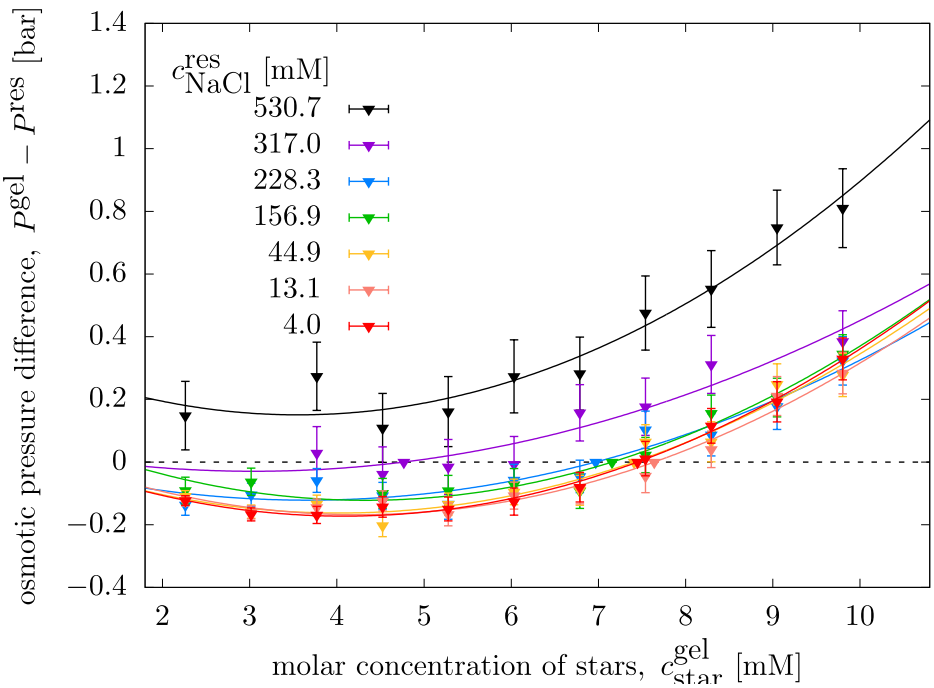

Figure 4.26: Pc-curves of polymer-rich phases of quenched anionic and quenched cationic stars coupled to NaCl reservoirs at various salt concentrations.

separate phase in mechanical and chemical equilibrium with the reservoir. As $c^{\mathrm{res}}_{\mathrm{NaCl}}$ decreases, the multi-phase equilibrium remains present, but the equilibrium density of the system shifts to higher polymer concentrations, as both screening effects and excluded-volume repulsions become weaker, and formation of cross-links between the arms is stronger. Expectedly, the effect of salt becomes very weak for $c_{\mathrm{NaCl}} \lesssim 157$ mM. It is instructive to notice how the magnitude of standard errors of pressure varies with both $c^{\mathrm{res}}_{\mathrm{NaCl}}$ and density of the system. Increasing either of them yields larger errors, because both effects result in a denser system with higher total density of particles. In a denser system, collisions between particles are more frequent, implying more significant contribution of strongly fluctuating forces due to short-range repulsions to the total pressure. Indeed, Figure 4.26 shows that the system of stars can co-exist with a reservoir in the mechanical and chemical equilibrium. However, whether the phase is really a gel is yet to be explored.

4.4.4 Separated stars or an interconnected network?

In order to quantify the structural properties of the polymer-rich phase, we coin a term *connection* to describe the existence of a temporary cross-link between two arms. We consider two arms to be connected if there is a pair of monomers belonging to these arms such that their distance if is less than 1.2σ. Moreover, we consider two stars to be connected if there is a pair of arms belonging to respective stars such that they are connected. Finally, a *dangling* arm is an arm not having any connections. Analogically, a dangling star is a star not involved in any connections, thus a star possessing four dangling arms. Similar to Section 4.2 and Section 4.3, the choice of the threshold is arbitrary, but the resulting trends

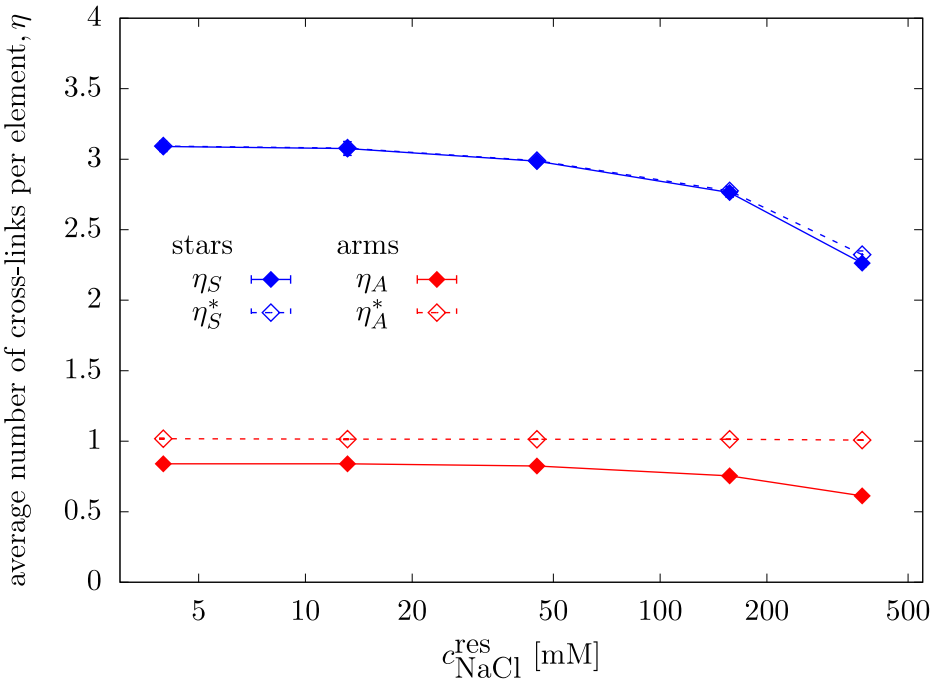

(a) Average number of star-star contacts per star and average number of arm-arm contacts per arm as a function of $c_{\mathrm{NaCl}}^{\mathrm{res}}$. The solid lines average over the whole ensemble of star (η_S) or arms (η_A), while the dashed lines exclude dangling stars (η_S^*) or arms (η_A^*) from the respective ensembles.

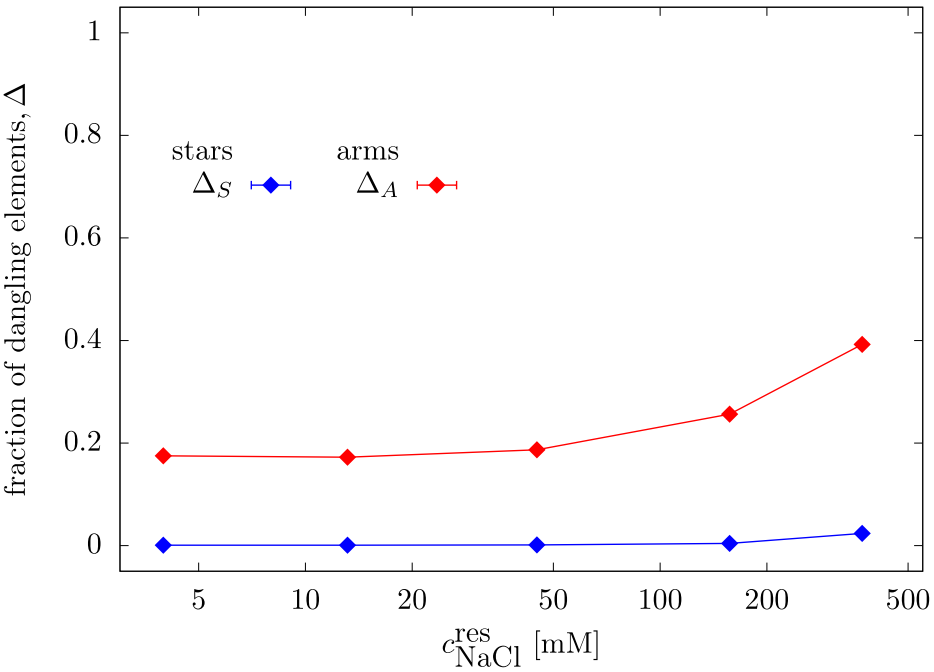

(b) Fractions of dangling stars (Δ_S) and dangling arms (Δ_A) as a function of $c_{\mathrm{NaCl}}^{\mathrm{res}}$

Figure 4.27: Structural properties of the gel phase as a function of $c_{\mathrm{NaCl}}^{\mathrm{res}}$.

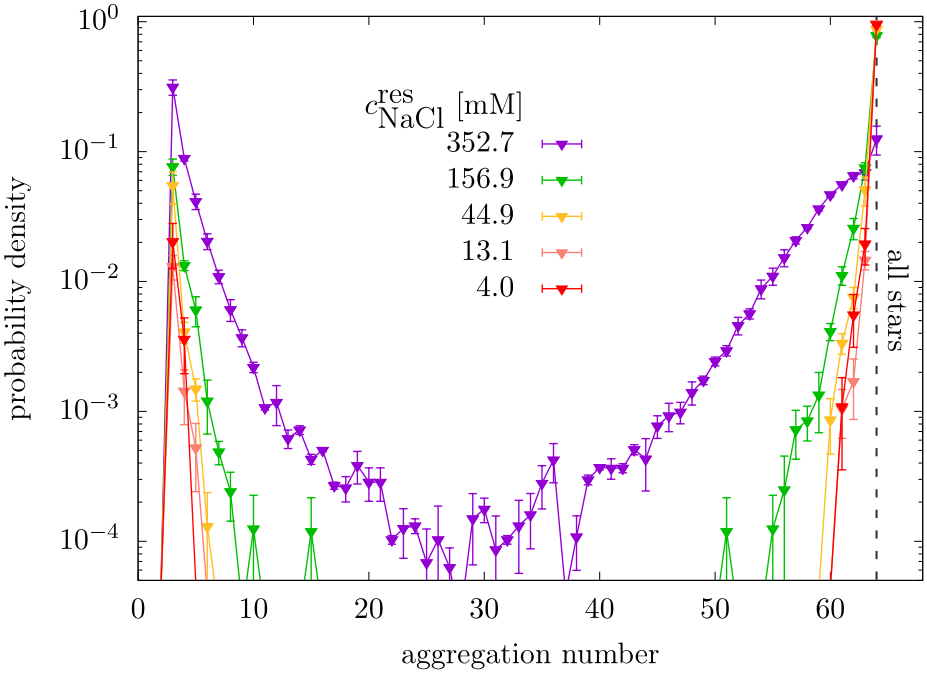

Figure 4.28: Probability distribution of sizes of clusters of star in the polymer-rich phase coupled to reservoirs at various $c^{\mathrm{res}}_{\mathrm{NaCl}}$.

are rather insensitive to the specific choice of the threshold value.

In Figure 4.27a we show the average number of stars connected to an arbitrary star as a function of $c^{\mathrm{res}}_{\mathrm{NaCl}}$. The solid line represents the average over the whole ensemble of stars, while the dashed line presents the average over the ensemble excluding the dangling stars. Figure 4.27a shows that with increasing $c^{\mathrm{res}}_{\mathrm{NaCl}}$, stars form fewer connections. However, even at high $c^{\mathrm{res}}_{\mathrm{NaCl}}$, average star is connected to more than two other stars. Concurrently, arms exhibit qualitatively the same trend – the number of arm-arm connections decreases as $c^{\mathrm{res}}_{\mathrm{NaCl}}$ increases. Following the dashed line, if an arm possesses a connection, it is most likely to be connected to only one arm. Furthermore, Figure 4.27b shows that the number dangling arms increases as a function of $c^{\mathrm{res}}_{\mathrm{NaCl}}$, and at $c^{\mathrm{res}}_{\mathrm{NaCl}} \approx 352$ mM almost doubles as compared to the limit of low salt.

Clearly, each star possesses numerous connections thanks to its high number of arms. However the presented results does not exclude a possibility that the observed phase is just a collection of small aggregates, in contrast to percolating gel spanning the whole box. To prove that ensemble of stars represents a single network, we define a *cluster of stars*. If we represent all connections between stars in a given moment as a non-oriented graph, a cluster of stars is any subgraph of the graph with more than two vertices (stars). Additionally, we define the *size* of the cluster of stars as the number of vertices of the corresponding subgraph. In Figure 4.28 we plot the probability distribution of sizes of clusters observed in the simulations. We see that at $c^{\mathrm{res}}_{\mathrm{NaCl}} \lesssim 45$ mM practically all of the stars are connected in one continuous network. The distribution slightly broadens at $c^{\mathrm{res}}_{\mathrm{NaCl}} \approx 157$ mM, nevertheless a network containing all stars remains the most probable state. In contrast to $c^{\mathrm{res}}_{\mathrm{NaCl}} \lesssim 157$ mM, at $c^{\mathrm{res}}_{\mathrm{NaCl}} \approx 350$ mM we observe clusters of stars in the whole range of aggregation numbers, as opposed to a

single percolating network spanning the whole box. This is in accordance with the Figure 4.27b and Figure 4.27a. Smaller average numbers of contacts between arms and stars result in a lower connectivity of the network, as the presence of the salt in high concentration suppresses formation of cross-links.

Fairly, the system is in the phase equilibrium with reservoir, and the stars fill up the whole box, forming a single cross-linked network. The latter is necessary, but not a sufficient condition for the system to be a physical gel. Prior to claiming that the system comprises a reversible gel, an investigation of the characteristic time-scales and the strength of cross-links is essential.

4.4.5 Life-times and reversibility of cross-links

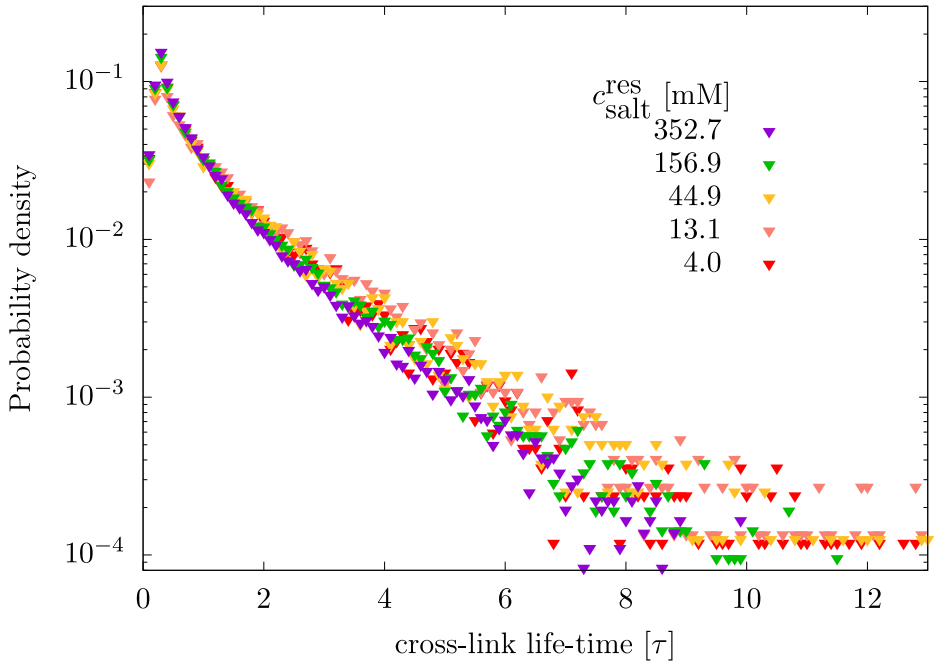

Figure 4.29: Probability distribution of life-times of cross-links between arms as a function of $c_{\text{NaCl}}^{\text{res}}$.

In Figure 4.29 we show the probability distribution of life-time of cross-links between arms. The figure shows that connections are kinetically not frozen and persist for times of order on ones of τ on average. As $c_{\text{NaCl}}^{\text{res}}$ increases, we observe a slight shift of the distribution to higher life-times. Accordingly, the mean life-time calculated as

$$\langle \tau \rangle = \int_0^\infty \mathrm{d}\tau \; p(\tau)\tau, \tag{4.16}$$

where $p(\tau)$ is the probability density decreases as a function of τ, as shown in Figure 4.30.

The simulations are significantly longer than the characteristic time-scale on which cross-link persist between the arms. Indeed, the cross-links dissolve and re-form, and the network is being structurally reformed on the time scale of the simulation. Observing the simulation movies, we were able to identify three key mechanisms involved in the reconstruction of the network, schematically depicted

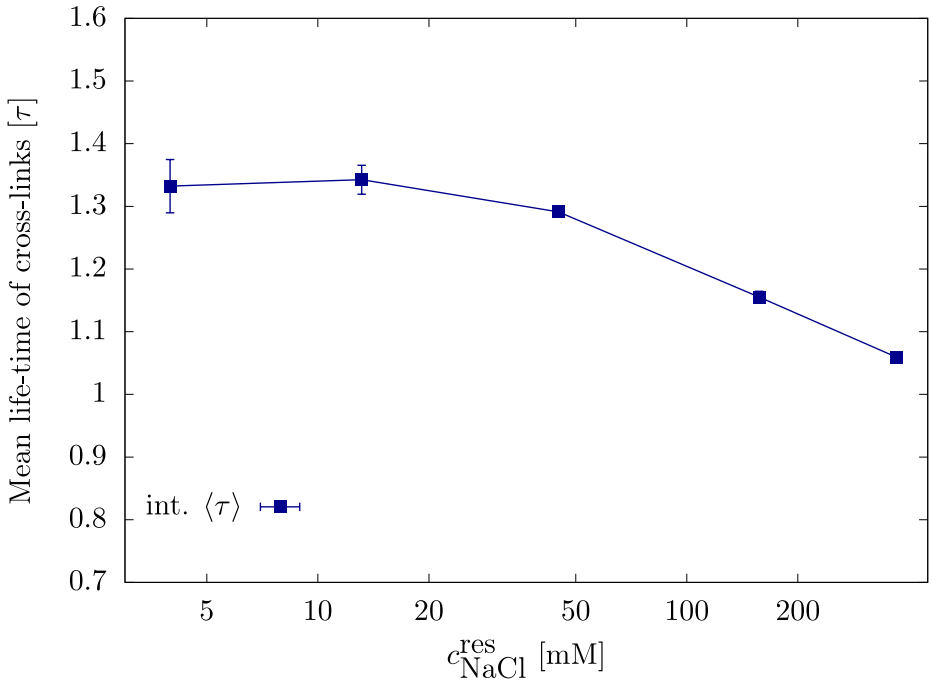

Figure 4.30: Mean life-time of cross-links as a function of $c^{\text{res}}_{\text{NaCl}}$. The mean value was calculated as an integral of distribution in Figure 4.29.

in Figure 4.31. The terminology was established by Tagliabue *et. al.* [TLMH] and it comprises:

(a) *intermittent bond*, $\mathcal{I}$ with a scheme
$\alpha\cdots\beta \underset{\tau_{\text{lag}}}{\overset{\tau_{\text{bond}}}{\rightleftarrows}} \alpha + \beta$,
defined by three events: formation of a cross-link between arms α and β at the time t_1; dissolution of the cross-link at the time t_2; re-formation of the cross-link between arms α and β at the time t_3. Then $t_3 - t_2 = \tau_{\text{lag}}$ and $t_2 - t_1 = \tau_{\text{bond}}$. Additionally, α and β are not allowed to participate in any other cross-links in the time interval $[t_1, t_3]$.

(b) *anticipated partner switch*, $\mathcal{S}_{\text{ant}}$ with a scheme:
$\gamma^{-} + \alpha\cdots\beta \xrightarrow{\tau_{\text{lag}}} \gamma\cdots\alpha\cdots\beta \xrightarrow{\tau_{\text{bond}}} \gamma\cdots\alpha + \beta$
defined by three events: formation of a cross-link between arms α and β at the time t_1; formation of a an additional cross-link between arm α (without loss of generality) and arm γ at the time t_2; dissolution of the cross-link between α and β at the time t_3. Then $t_2 - t_1 = \tau_{\text{lag}}$ and $t_3 - t_2 = \tau_{\text{bond}}$. Additionally, cross-link between α and γ has to be preserved at the time t_3, and any involvement of a fourth arm is forbidden during the time interval $[t_1, t_3]$.

(c) *postponed partner switch*, $\mathcal{S}_{pos}$ with a scheme:
$\gamma + \alpha\cdots\beta \xrightarrow{\tau_{\text{bond}}} \gamma + \alpha + \beta \xrightarrow{\tau_{\text{lag}}} \gamma\cdots\alpha + \beta$
defined by three events: formation of a cross-link between arms α and β at the time t_1; dissolution of the cross-link at the time t_2; formation of a cross-link between arms α and γ at the time t_3. Then $t_3 - t_2 = \tau_{\text{lag}}$ and

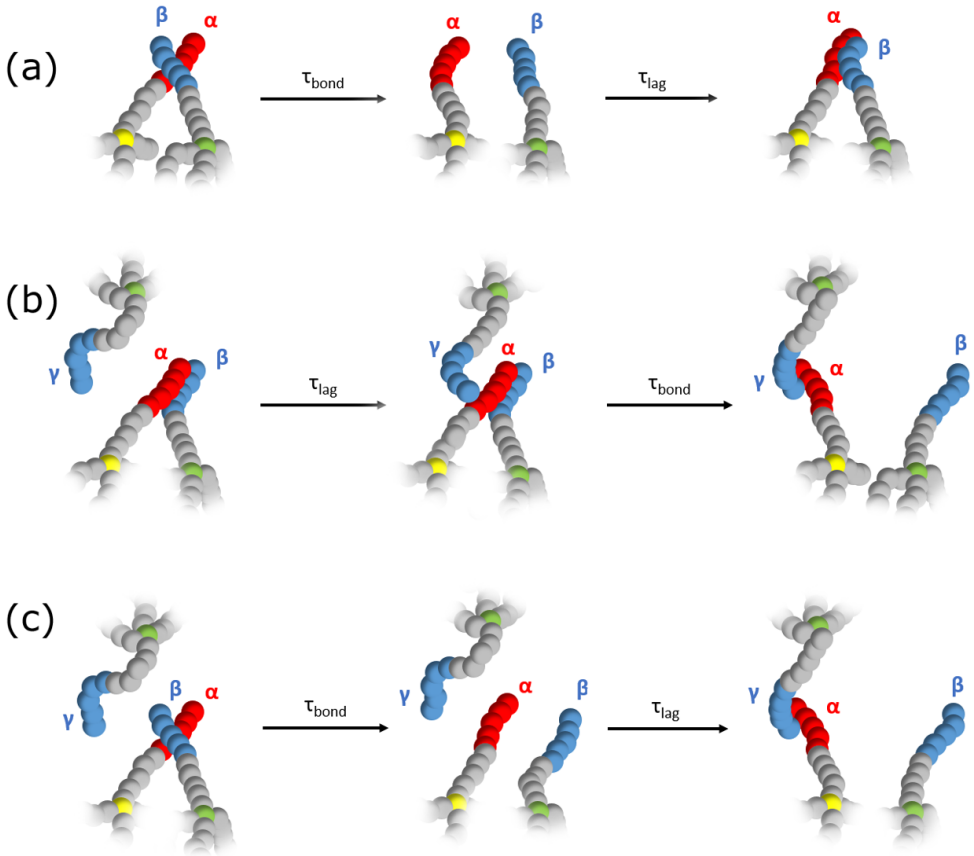

Figure 4.31: Proposed model mechanisms involved in cross-link formation and dissolution: (a): intermittent bond, $\mathcal{I}$, (b): anticipated partner switch, $\mathcal{S}_{\text{ant}}$, (c): postponed partner switch, $\mathcal{S}_{\text{pos}}$. This scheme is from the manuscript Ref. [TLMH] in preparation, and was used with the permission of its author Andrea Tagliabue.

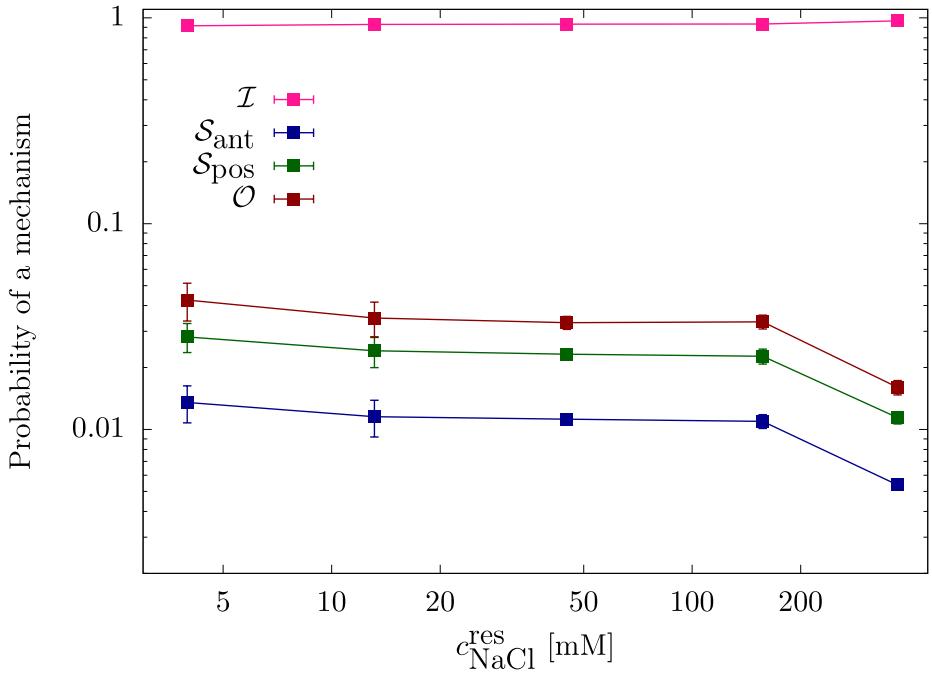

Figure 4.32: Relative contribution of mechanisms from the Figure 4.31 to the reconstruction of the gel as a function of $c^{\text{res}}_{\text{NaCl}}$.

$t_2 - t_1 = \tau_{\text{bond}}$. Additionally, any involvement of a fourth arm is forbidden in the time interval $[t_1, t_3]$.

Finally, we propose a label *other*, $\mathcal{O}$, for any mechanism that does not belong to any of the above classes. In Figure 4.32 we plot the contributions of respective mechanisms to the dynamical structural rearrangements of the gel. We observe that intermittent bond is the most prevalent one in the whole range of c_{NaCl} and accounts for $\gtrsim 90\%$ of restructuring events. Presumably, the intermittent bond is prevalent because it requires an involvement of two arms at a time, as opposed to different mechanisms. Moreover, when a cross-link between the two arms is broken without the presence of a third arm, re-establishment of the same cross-link is very probable due to the mutual attraction and proximity of the now-dangling arms. Additionally, we observe that other mechanisms participate in the cross-link exchange with probability of two orders of magnitude lower, however totaling at $\approx 10\%$ participation on the events. The presence of these other mechanism indicates that our simulations are long enough to observe not just dissolution of cross-link, but also an exchange of binding partners between the arms and stars. The latter suggests that the system is not trapped in a kinetically frozen state, and thus represents an electrostatically cross-linked reversible physical gel.

4.4.6 The first step towards pH-responsive gel formation

Finally, we replaced quenched anionic segments by weakly acidic ones, and couple the system to a reservoir containing also H^+ and OH^- ions, in order to study pH-controlled gelation. The reservoir was then described by I^{res} and pH^{res}. *Pc*-curves in Figure 4.33 show that at $\text{pH}^{\text{res}} \lesssim 9.65$, the phase equilibrium is not reached. In contrast to the quenched anionic segments at high $c^{\text{res}}_{\text{NaCl}}$ limit, the

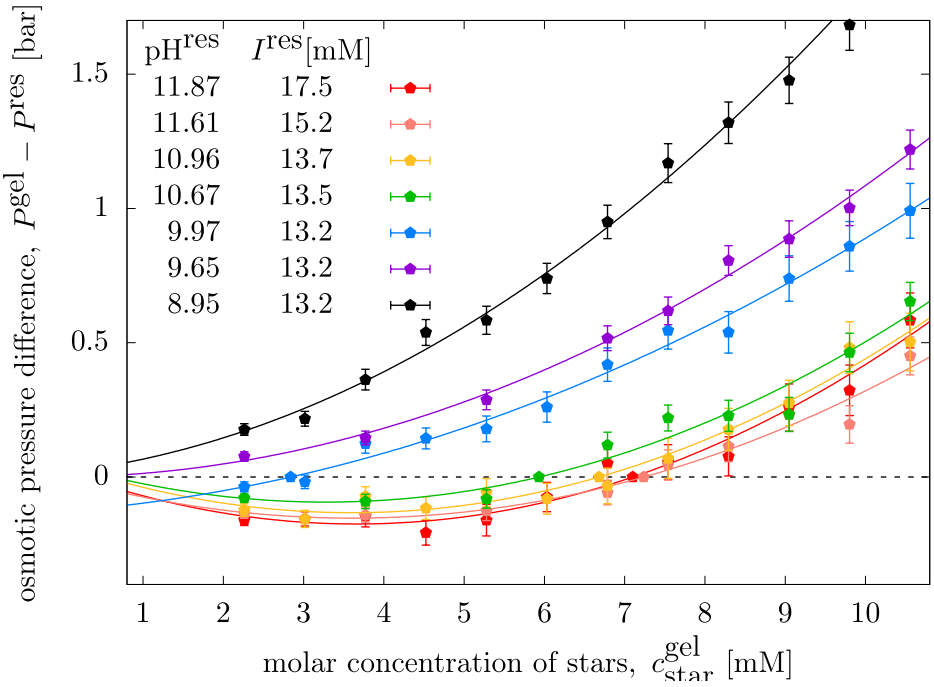

Figure 4.33: Pc-curves of polymer-rich phases coupled to reservoirs at various $\mathrm{pH}^{\mathrm{res}}$ and I^{res} values.

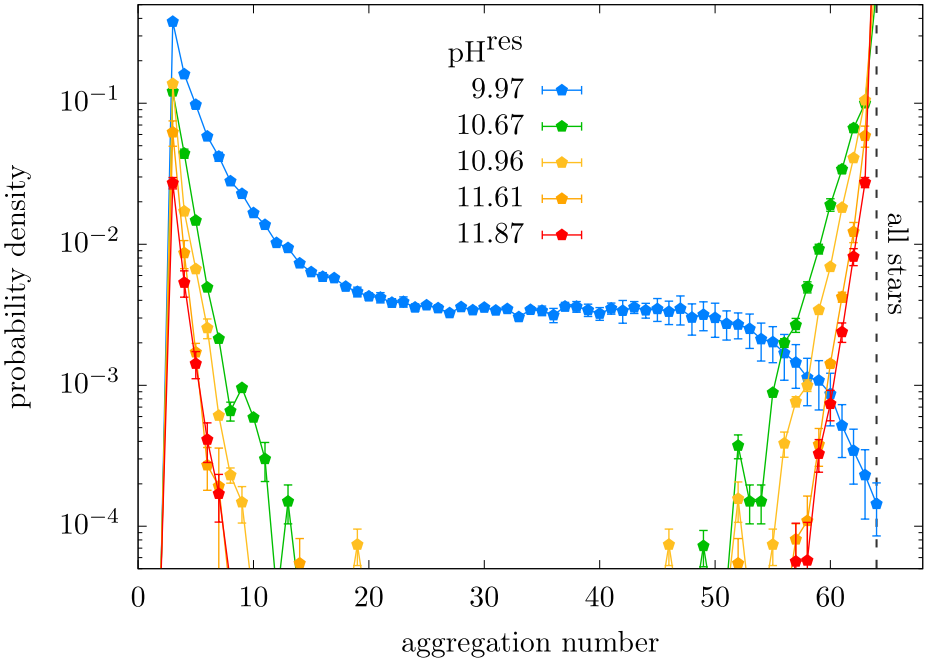

Figure 4.34: Probability distribution of sizes of clusters of star in the polymer-rich phase coupled to reservoirs at various $\mathrm{pH}^{\mathrm{res}}$ values.

annealed stars at $\mathrm{pH}^{\mathrm{res}} \lesssim 9.65$ are only partly dissociated. The formation of polyanion-polycation cross-links is therefore suppressed, because of weaker attractions between the oppositely charged arms. We observe that increasing the $\mathrm{pH}^{\mathrm{res}}$ leads to the formation of a stable gel phase in equilibrium with the reservoir at progressively increasing equilibrium polymer densities. Notably, the equilibrium polymer concentration at $\mathrm{pH}^{\mathrm{res}} \gtrsim 10.96$ is almost independent of the specific value of $\mathrm{pH}^{\mathrm{res}}$, suggesting, that anionic arms have reached the full ionization, and thus the same charge as in the system of quenched stars. Because of practical pitfalls of grand reaction method, we were not able to compare the systems at exactly matching I^{res}. However, the preceding subsections demonstrated that ionic strength at $I^{\mathrm{res}} \lesssim 44.9$ mM has only marginal effect on the gel properties. Therefore, the equilibrium composition and structure of the gel is caused mainly by the effects of pH.

Similar to the analysis in Section 4.4.3, in Figure 6.15b we show the average numbers of cross-links per arm and per star. We see that number of cross-links increases with $\mathrm{pH}^{\mathrm{res}}$ and thus with the average charge on the anionic arms. Consequently, increase in $\mathrm{pH}^{\mathrm{res}}$ means a decrease in the fraction of dangling arms and stars (see Figure 6.15d). Importantly, for a sufficiently high pH, we converge to the same results as in the case of quenched stars at comparable I^{res}. Next, Figure 4.34 shows that for $\mathrm{pH}^{\mathrm{res}} \gtrsim 10.67$, the stars form a single network spanning the whole system, in contrast to $\mathrm{pH}^{\mathrm{res}} \lesssim 9.97$ where the most probable size of a cluster of stars is of the order of unity. However, in the case when a single percolating network is formed, its formation is reversile gelation, as shown in Figure 6.17 and Figure 6.18.

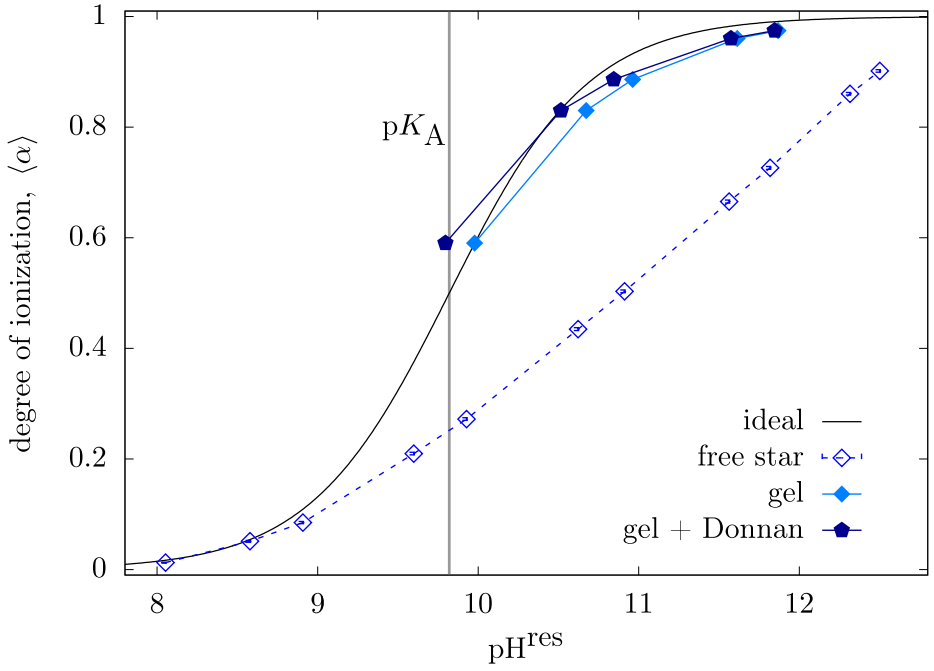

Figure 4.35: Titration curve of positive stars in the gel with and without explicit inclusion of the Donnan effect. The curves are compared to the ideal titration curve and titration curve of a single positive star in a dilute solution at $I \approx 13$ mM and $c_{\mathrm{star}} \approx 0.277$ mM

Finally, we provide a direct link between $\mathrm{pH}^{\mathrm{res}}$ and the average charge on the annealed sequences. In Figure 4.35 we compare titration curves of annealed stars in the gel and a free star in a dilute solution at $c_{\mathrm{star}} = 0.277$ mM coupled to the same reservoir. In close analogy with Section 4.3 we observe that titration curve of a free star is shifted to lower ionization, as compared to the ideal one due to the polyelectrolyte effect between the like-charged segments. The presence of oppositely charged cationic sequences in the gel shifts the titration curve of acidic stars to higher ionization. Enhanced ionization is promoted by two effects: 1.) formation of the interpolyelectrolyte complex between the oppositely charged arms and 2.) the Donnan effect. The former has already been discussed in detail in Section 4.2 and in Section 4.3. The latter however, has not been present in the previous two systems, because these systems were closed, as opposed to the gel coupled to a reservoir. If the anionic stars are fully charged, their charge neutralizes the total charge on cationic stars, resulting in zero Donnan potential between the gel and the reservoir [LHR$^+$20]. However, as the ionization on the acidic stars decreases, the gel attains a net positive charge, resulting in the Donnan effect causing $\mathrm{pH}^{\mathrm{res}} < \mathrm{pH}^{\mathrm{gel}}$. In Figure 4.35 we show also the titration curve of the gel accounting for the Donnan effect evaluated by (1.27). Plotting the degree of ionization as a function $\mathrm{pH}^{\mathrm{res}}$ with the Donnan effect included is equivalent to plotting the degree of ionization as a function of $\mathrm{pH}^{\mathrm{gel}}$. Finally, we see that the shift of the ionization between the gel and free star is caused mainly by the polyelectrolyte effect, and the Donnan effect is overall weak in the studied range of pH.

4.4.7 Conclusion and outlook

We employed the Grand reaction method to carry out simulations of an ensemble of tetra-functional star-like polymers composed of hydrophilic arms terminated by charged blocks of two types – quenched cationic or annealed anionic. Oppositely charged termini electrostatically cross-link the stars, leading to the formation of a gel phase. The gel of stars is a single interconnected percolating network spanning the whole system. Simultaneously, cross-links are not frozen, and the network reorders itself, which poses a necessary condition for a gel to be reversible.

The gel formation is not observed if the salt concentration in the reservoir is too high, because the phase of stars becomes too dense in the number of particles, and electrostatic cross-links are no longer able to stabilize it. Sufficiently high value of pH is also a prerequisite for the gel formation, although for a different reason – if the pH of reservoir is low, anionic termini are on average weakly charged resulting in insufficient stability of cross-links.

Repulsions between the like charges, and correlations due to attraction between opposite charges, complicate the description of ionization of single stars. However, both these effects in our system almost quantitatively cancel each other, substantially simplifying the characterization of the gel – the titration curve of the acidic star in the gel is well approximated by the ideal one. Furthermore, we see that the gel is formed when $\mathrm{pH}^{\mathrm{res}} > \mathrm{p}K_{\mathrm{A}}$, which might be useful in predicting the pH of the gel-sol transition for the possible choice of acidic segments different from PDha. Our collaborators in the group of Felix Schacher in Jena are currently planning to conduct experiments on these systems, to measure the

titration curves of the polymer to verify the results of our simulations. Thus our simulations are directly being used as a predictive tool for the experimental design of specific reversible gels with the gelation controlled by pH.

5. Conclusion

In summary, we have used coarse-grained Monte Carlo simulations to explore ion partitioning and ionization equilibria in polyelectrolyte systems differing in the composition and structure, yet governed by the closely related physical principles. The unifying motif, repeatedly occurring in the studied systems, is a competition between strong non-ideal effects: 1.) repulsions between like charges on the polymer; 2.) associative complexation of ionized segments with multivalent counterions or oppositely charged chains. The former suppresses ionization of the polyelectrolyte by increasing the enthalpic contribution to the free energy, upon accumulation of the charge on the chain. The latter enhances the ionization due to both entropy gained by counterion release, and lowering the internal energy by the formation of ionic complexes. The relative magnitude of the contributing effects depends on the properties of the system.

In Section 4.2, we have shown that addition of just a small amount of trivalent ions shifts the titration curve of a weak polyelectrolyte closer to the ideal one, implying enhancement of ionization. Additionally, the polymer accumulates the trivalent ions up to effective neutralization of its charge, suggesting that the ratio between the total charge on the polymer and the total charge on the multivalent counterions, ξ, is the key controlling parameter. While in Section 4.2 we focused on $\xi \approx 1/2$, in Section 4.3 we focused mainly on $\xi \approx 2$. The excess of strong polyelectrolyte, representing DNA, enhanced the ionization of oligopeptides of length $N = 8$, shifting the titration curve to the ionization much higher than predicted by the Henderson-Hasselbalch equation. Finally, in Section 4.4 we described a system in which $\xi \approx 1$, where the titration curve almost quantitatively coincided with the ideal titration curve, which suggests approximate cancellation of the two effects mentioned above.

Besides the investigation of the ionization response, in Section 4.1, we have introduced a novel model of complex coacervate to understand the ion partitioning between the polymer-rich and co-existing polymer-poor phase. We showed that partitioning of ions is driven by interplay of two main mechanisms: 1.) the Donnan effect, which arises by imposing the electroneutrality constraint for each of the phases in coacervate system; 2.) the effect of inter-particle interactions. The former is dominating for univalent ions at low $c^{\mathrm{res}}_{\mathrm{NaCl}}$ or if $\Xi \neq 1$, where Ξ is the ratio between polyanion and polycation in the coacervate. The Donnan effect as a driving force becomes weaker at higher $c^{\mathrm{res}}_{\mathrm{NaCl}}$ or at Ξ closer to unity, while it diminishes completely for $\Xi = 1$. If multivalent ions are present, both effects are strongly coupled, and neither of them alone can be used to quantitatively describe the partitioning.

6. Supplementary figures

6.1 Coacervate as a scavenger of small ions

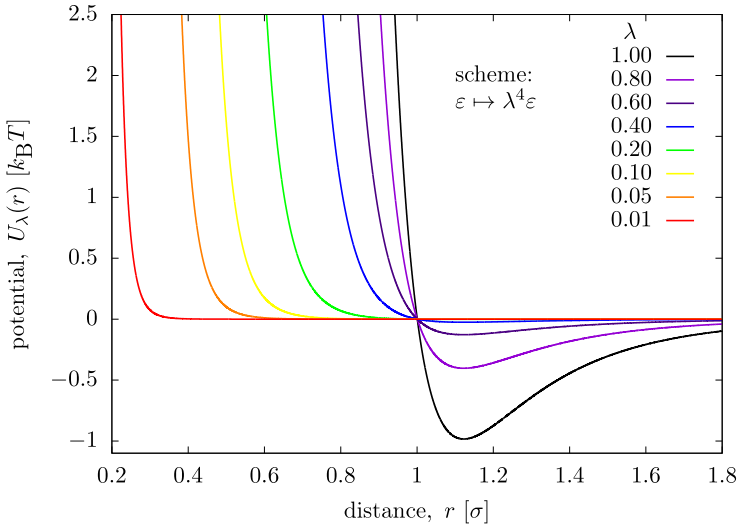

Figure 6.1: The Lennard-Jones potential parametrized with the (4.3) scheme, plotted for $\varepsilon = 1\ k_\mathrm{B}T$, $\sigma = 1$, $r_\mathrm{c} = 2.5\sigma$, and various values of the coupling parameter λ.

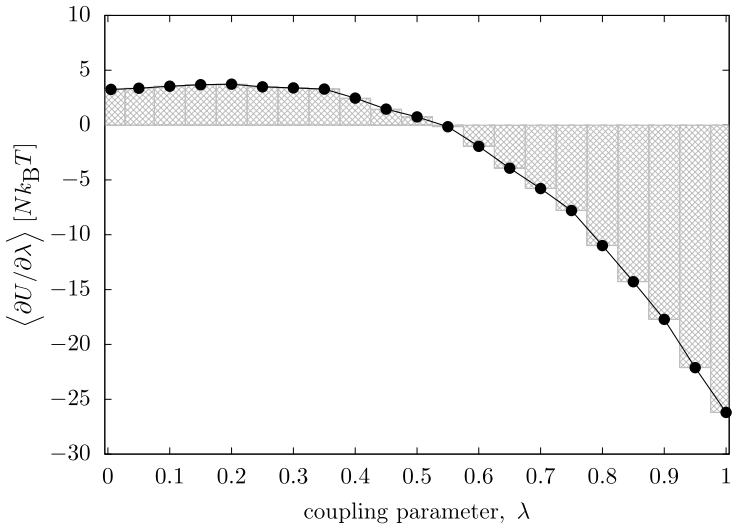

Figure 6.2: Free energy curve for the excess free energy per particles of Lennard-Jones fluid at density $\rho = 0.8\ N/\sigma^3$ and reduced temperature $T^* = 0.75k_\mathrm{B}T/\varepsilon_\mathrm{LJ}$ carried out by decoupling scheme (4.3).

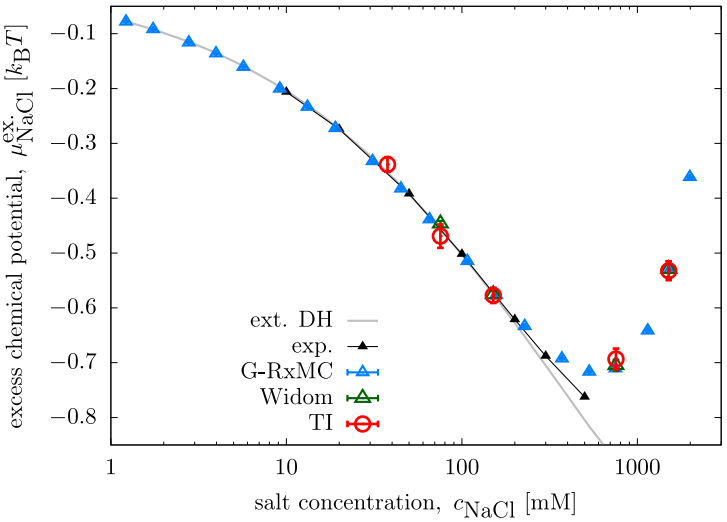

Figure 6.3: Excess chemical potential of NaCl as a function of c_{NaCl} calculated with thermodynamic integration, Widom insertion method and Grand-reaction Monte Carlo methods. The results are compared with the experimental results of measurements of activity coefficients of ions in aqueous NaCl solutions [Tru68], and compared with the extended Debye-Hückel theory.

6.2 The origins of polyelectrolyte proclivity for multivalent ions

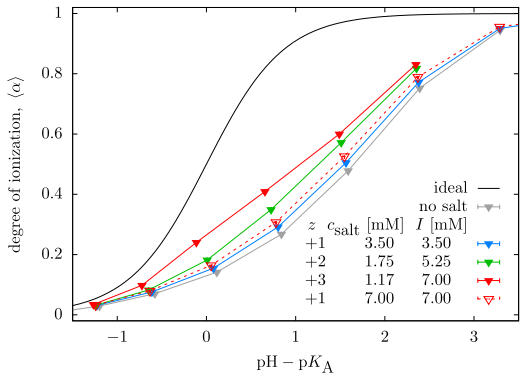

(a) $\xi = 0.25$

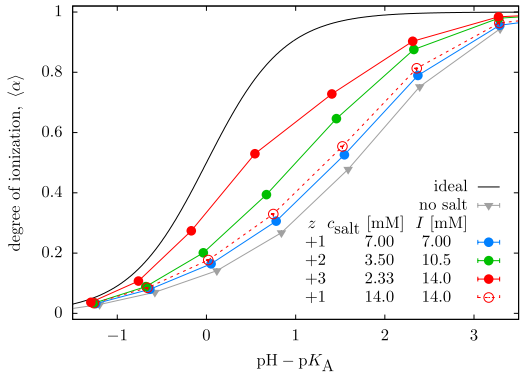

(b) $\xi = 0.50$

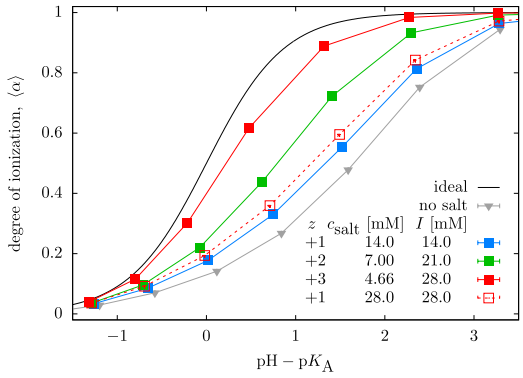

(c) $\xi = 1.00$

Figure 6.4: Titration curves of a weak star-like polyelectrolyte in presence of multivalent salt at fixed charge ratio ξ. The curve for trivalent curve is compared to the uni-univalent one at the same ionic strength.

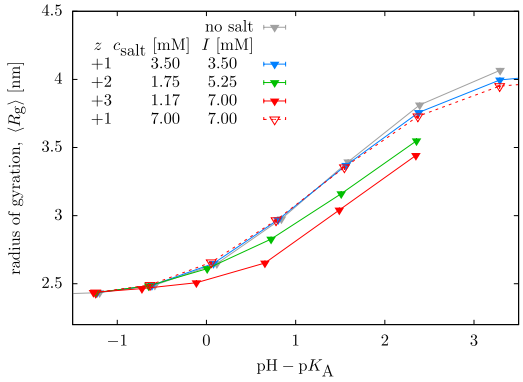

(a) $\xi = 0.25$

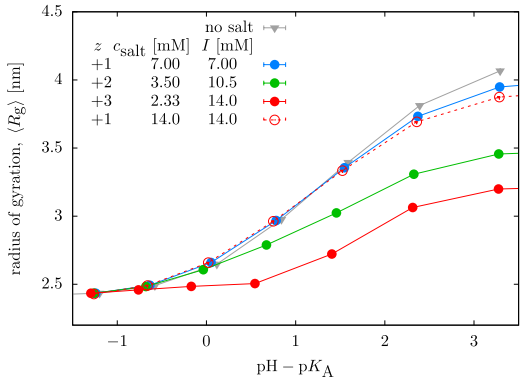

(b) $\xi = 0.50$

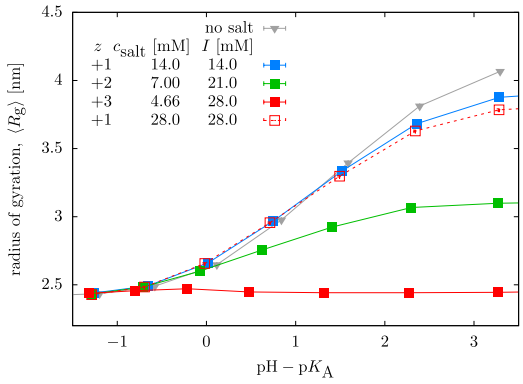

(c) $\xi = 1.00$

Figure 6.5: Radius of gyration of a weak star-like polyelectrolyte in presence of multivalent salt at fixed charge ratio ξ. The curve for trivalent curve is compared to the uni-univalent one at the same ionic strength.

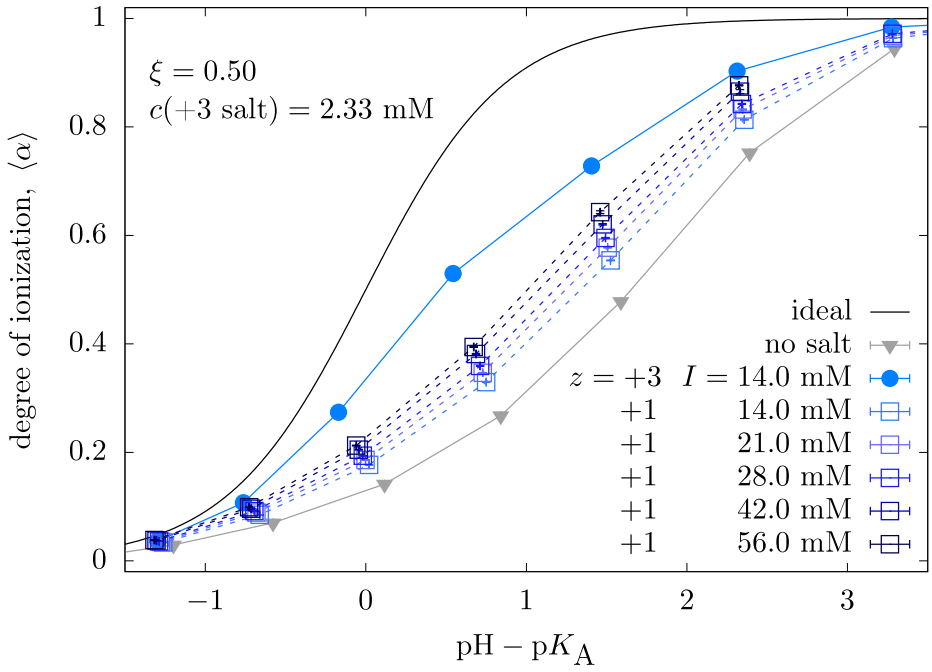

Figure 6.6: Titration curves of a weak star-like polyelectrolyte in presence of multi- and monovalent salt. Charge ratio of solution with multivalent salt was set constant $\xi = 0.50$. The multivalent titration curve is compared to titration curves for monovalent salt at various ionic strengths to show the magnitude of electrostatic screening and its effect on the ionization.

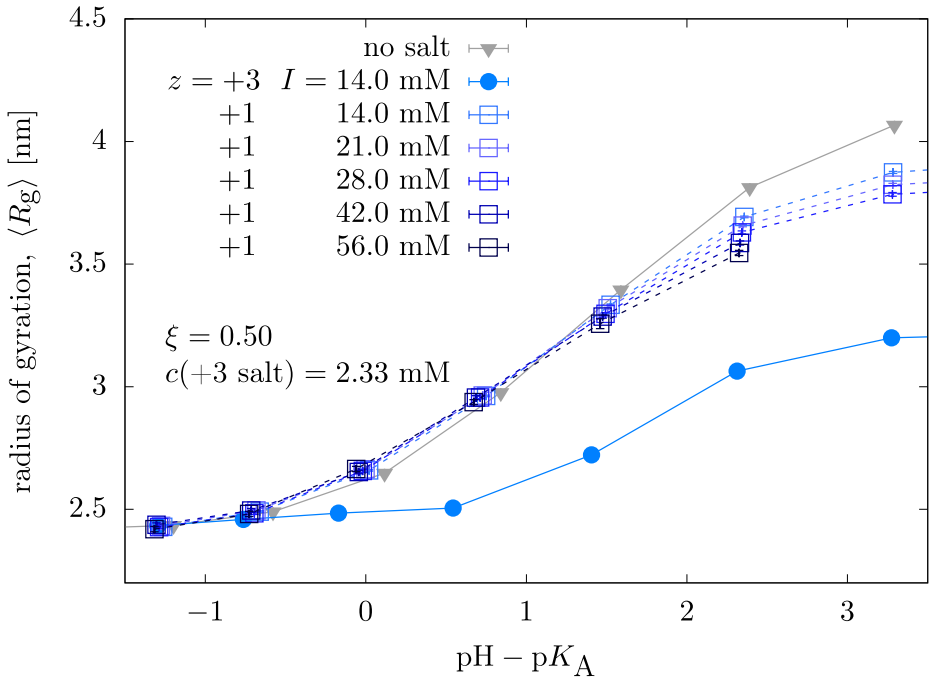

Figure 6.7: Radius of gyration of a weak star-like polyelectrolyte in presence of multi- and monovalent salt. Charge ratio of solution with multivalent salt was set constant $\xi = 0.50$. The multivalent radius of gyration is compared to radius of gyrations for monovalent salt at various ionic strengths to show the magnitude of electrostatic screening and its effect on conformation.

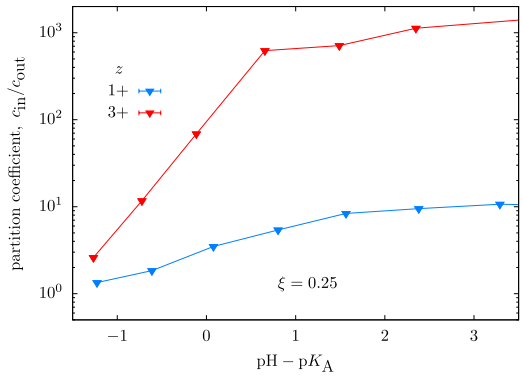

(a) $\xi = 0.25$

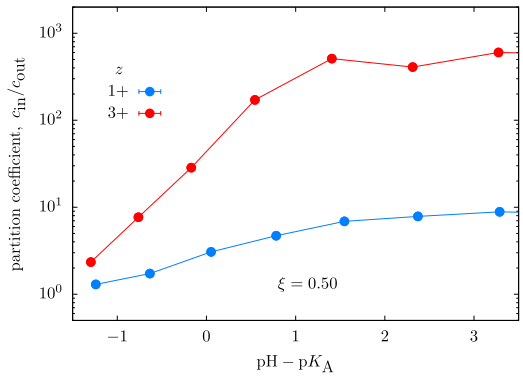

(b) $\xi = 0.50$

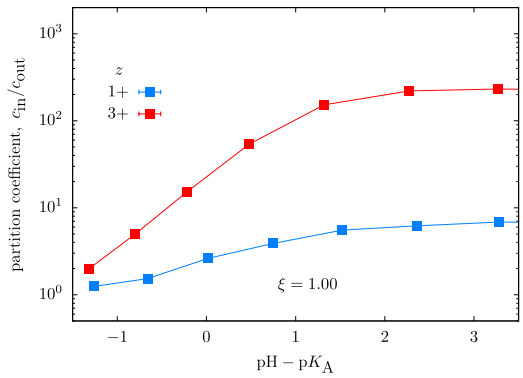

(c) $\xi = 1.00$

Figure 6.8: Partition coefficient for mono- and multivalent counterions at fixed charge ratio ξ.

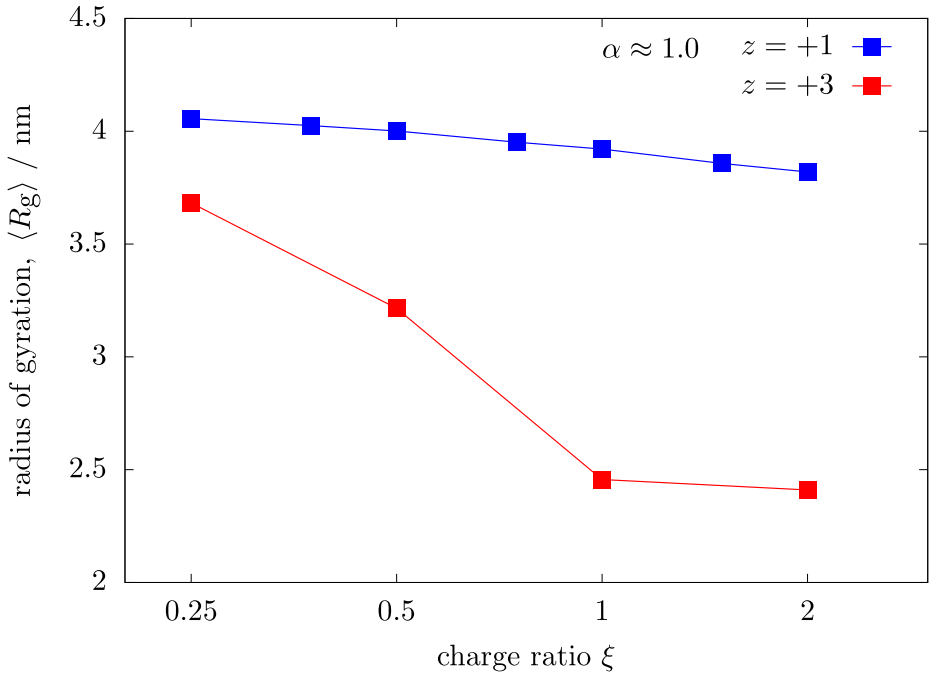

Figure 6.9: Radius gyration of a weak star-like polyelectrolyte in the limit of full ionization as a function of the charge ratio, ξ, for trivalent and monovalent salt.

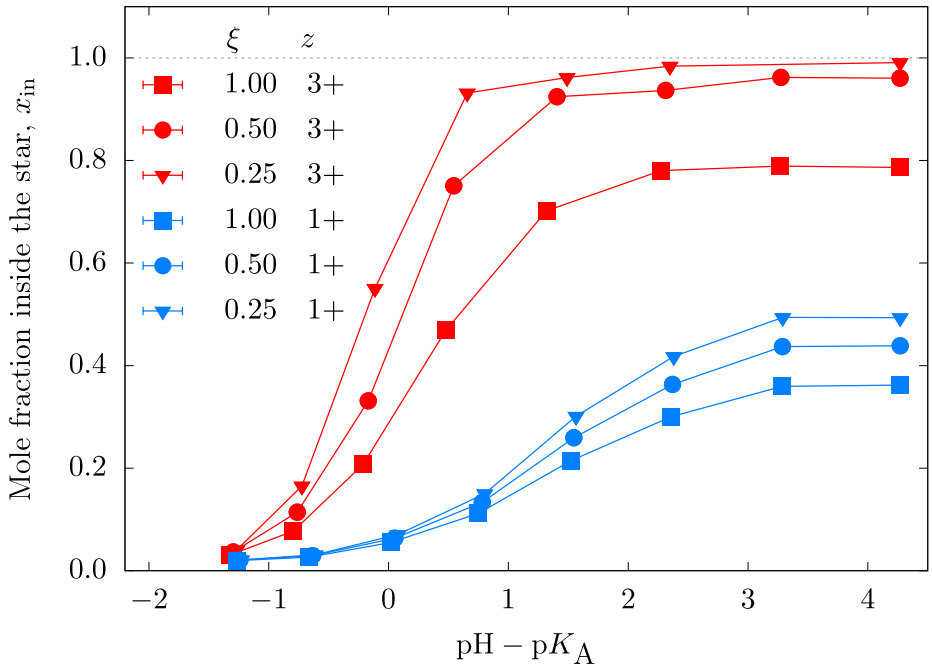

Figure 6.10: Mole fraction of monovalent and trivalent counterions inside the star as a function of pH − pK_A, compared for various charge ratios, ξ.

6.3 Probing ionization response of peptides in the presence of DNA

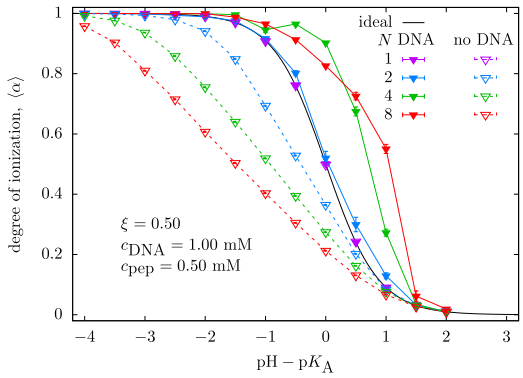

(a) $\xi = 0.50$

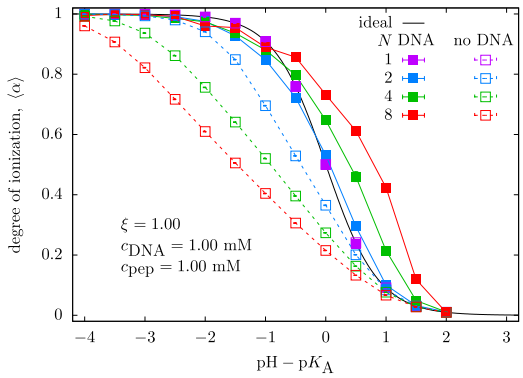

(b) $\xi = 1.00$

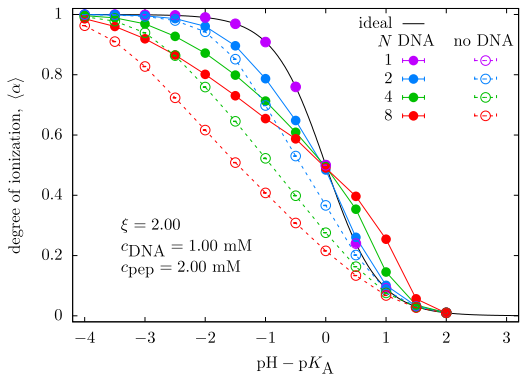

(c) $\xi = 2.00$

Figure 6.11: Titration curves of peptides of various lengths at the fixed charge ratio in solutions with and without the DNA present.

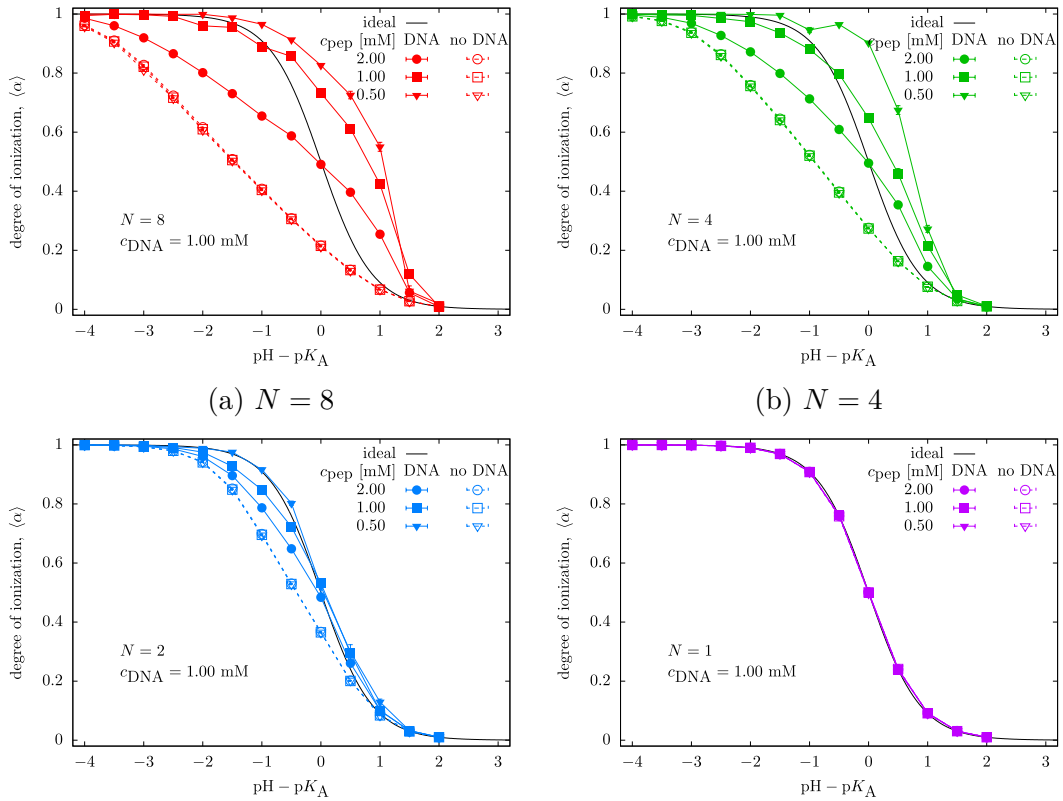

(a) $N = 8$ (b) $N = 4$

(c) $N = 2$ (d) $N = 1$

Figure 6.12: Titration curves of peptides at various charge ratios at fixed peptide length.

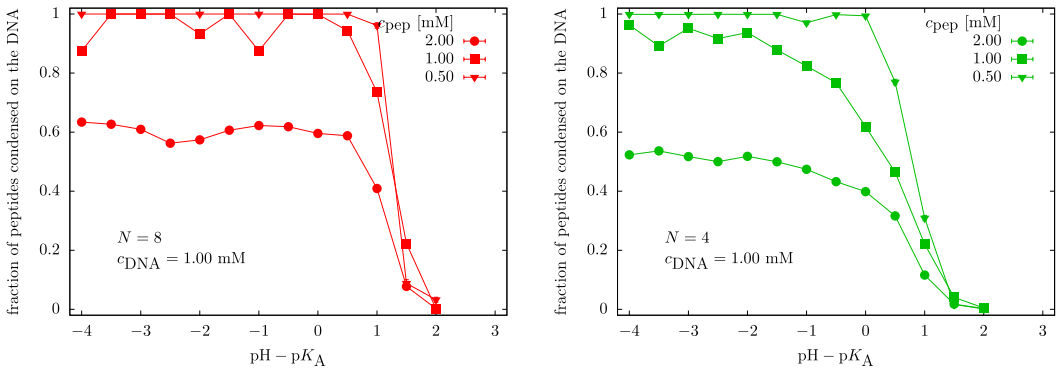

(a) $N = 8$ (b) $N = 4$

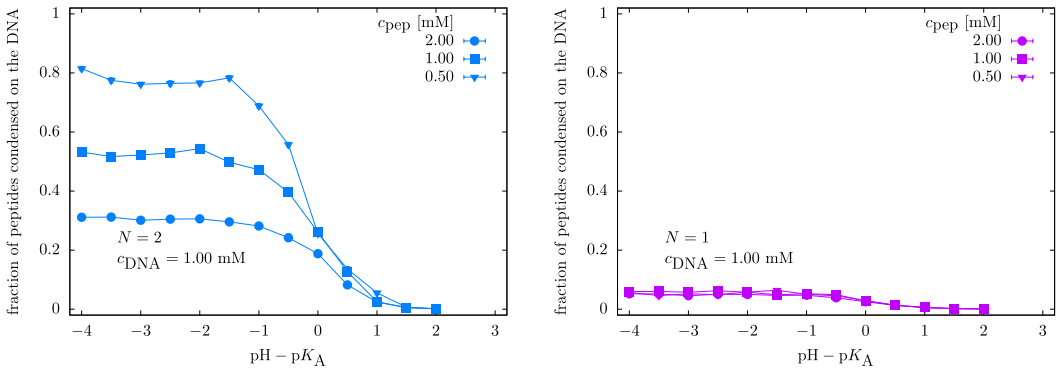

(c) $N = 2$ (d) $N = 1$

Figure 6.13: Fractions of peptides condensed on the DNA as a function of pH − pK_A at various charge ratios at fixed peptide length.

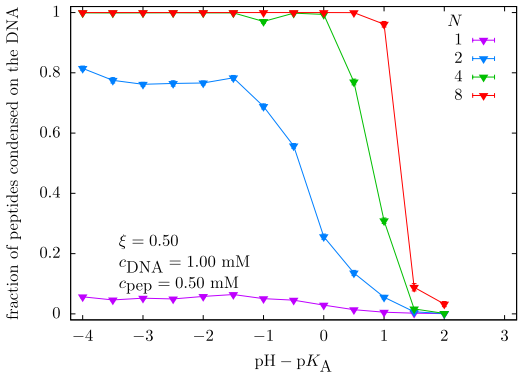

(a) $\xi = 0.50$

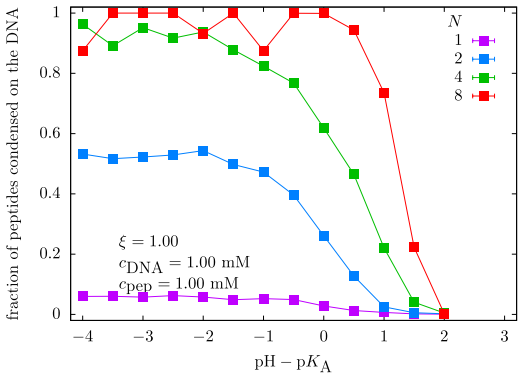

(b) $\xi = 1.00$

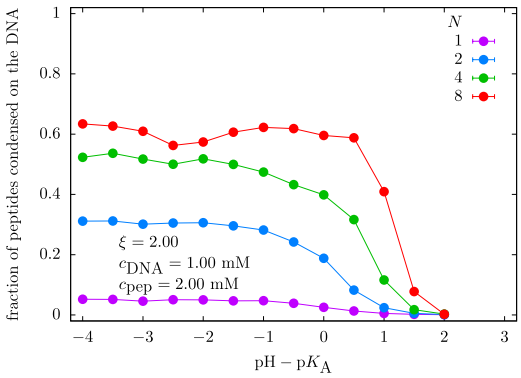

(c) $\xi = 2.00$

Figure 6.14: Fractions of peptides condensed on the DNA as a function of pH − pK_A at fixed charge ratio and various peptide lengths.

6.4 Electrostatically cross-linked reversible gels controlled by pH

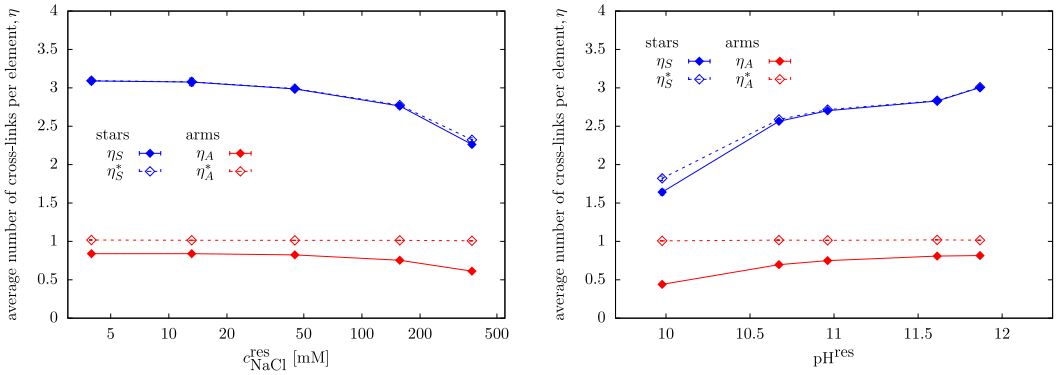

(a) Quenched anions; number of cross-links (b) Annealed anions; number of cross-links

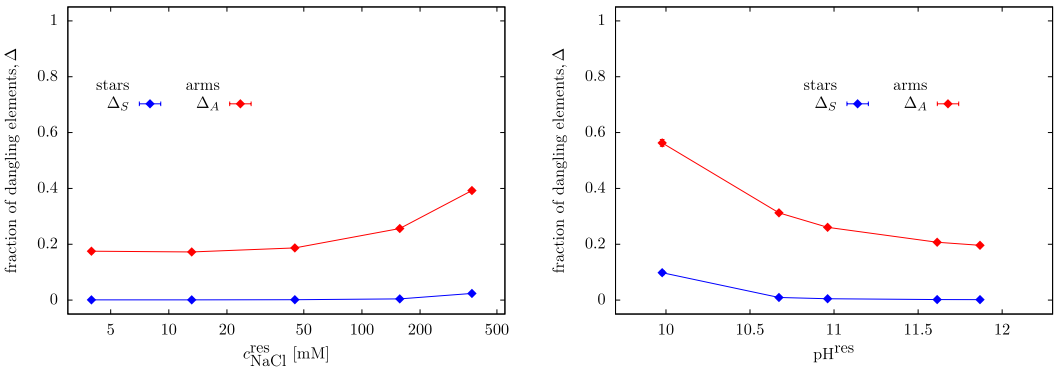

(c) Quenched anions; dangling elements (d) Annealed anions; dangling elements

Figure 6.15: Average numbers of star-star contacts per star and arm-arm contacts per arm compared as a function of $c_{\mathrm{NaCl}}^{\mathrm{res}}$ for quenched anions (Figure 6.15a) and as a function of $\mathrm{pH}^{\mathrm{res}}$ for annealed anions (Figure 6.15b). Fractions of dangling arms (Δ_A) and dangling stars (Δ_S) compared as a function of $c_{\mathrm{NaCl}}^{\mathrm{res}}$ for quenched anions (Figure 6.15c) and as a function of $\mathrm{pH}^{\mathrm{res}}$ for annealed anions (Figure 6.15d). Solid lines present averages calculated over the whole ensemble of stars (η_S) or arms (η_A), while dashed lines present averages calculated over ensemble of stars (η_S^*) or arms (η_A^*) excluding dangling stars or arms respectively.

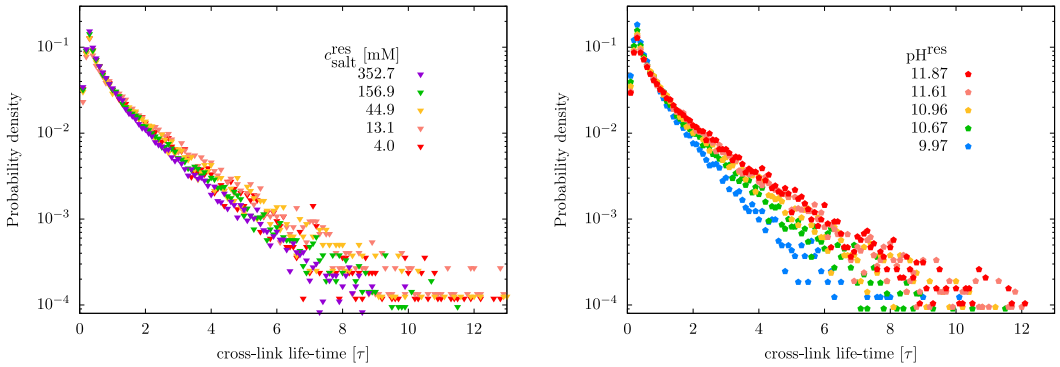

(a) Quenched anions (b) Annealed anions

Figure 6.16: Probability distribution of life-times of cross-links between arms as a function of c^{res}_{NaCl} for quenched anions, and as a function of pH^{res} for annealed anions.

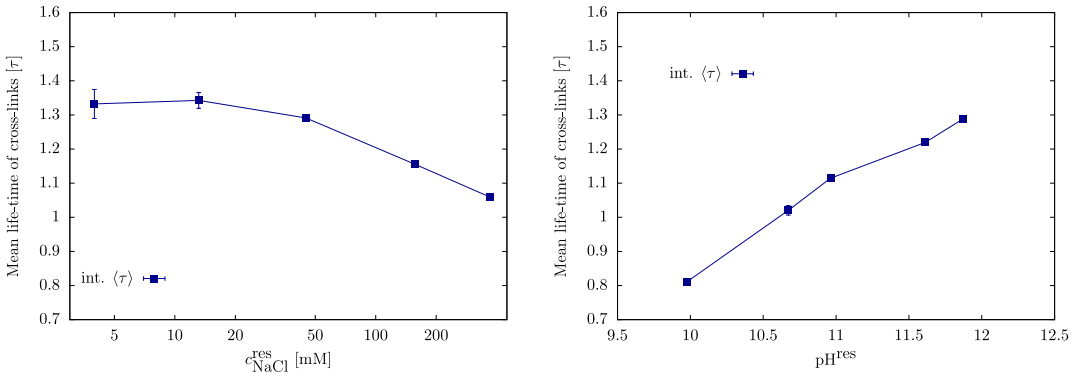

(a) Quenched anions (b) Annealed anions

Figure 6.17: Mean life-time of cross-links between arms compared as a function of c^{res}_{NaCl} for quenched anions, and as a function of pH^{res} for annealed anions.

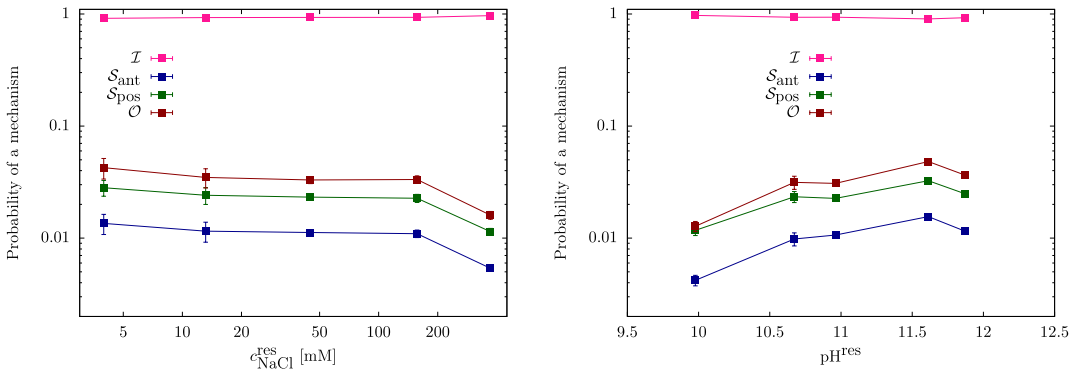

(a) Quenched anions (b) Annealed anions

Figure 6.18: Relative contribution of mechanisms from Figure 4.31 on the reconstruction of the gel compared as a function of c^{res}_{NaCl} for quenched anions, and as a function of pH^{res}.

Bibliography

[AdBLS12] E. A. Appel, J. del Barrio, X. J. Loh, and O. A. Scherman. Supramolecular polymeric hydrogels. *Chem. Soc. Rev.*, 41, 2012.

[AFN03] J. Anwar, D. Frenkel, and M. G. Noro. Calculation of the melting point of NaCl by molecular simulation. *J. Chem. Phys*, 118(2), 2003.

[AMVL+13] L. Albertazzi, F. J. Martinez-Veracoechea, C. M. A. Leenders, I. K. Voets, D. Frenkel, and E. W. Meijer. Spatiotemporal control and superselectivity in supramolecular polymers using multivalency. *Proc. Natl. Acad. Sci. U.S.A.*, 110(30), 2013.

[APD+18] M. Andreev, V. M. Prabhu, J. F. Douglas, M. Tirrell, and J. J. de Pablo. Complex Coacervation in Polyelectrolytes from a Coarse-Grained Model. *Macromolecules*, 51(17), 2018.

[Arn57] R. Arnold. The titration of polymeric acids. *J. Phys. Condens. Matter*, 12, 1957.

[AZG+19] P. Anees, Y. Zhao, A. A. Greschner, T. R. Congdon, H. W. de Haan, N. Cottenye, and M. A. Gauthier. Evidence, Manipulation, and Termination of pH 'Nanobuffering' for Quantitative Homogenous Scavenging of Monoclonal Antibodies. *ACS Nano*, 13(2), 2019.

[BD09] T. Bereau and M. Deserno. Generic coarse-grained model for protein folding and aggregation. *J. Chem. Phys.*, 130(23), 2009.

[BJ96] J.-L. Barrat and J.-F. Joanny. *Theory of Polyelectrolyte Solutions*. Number 2. John Wiley & Sons, Ltd, 1996.

[BMvS+94] T. C. Beutler, A. E. Mark, R. C. van Schaik, P. R. Gerber, and V. F. van Gunsteren. Avoiding singularities and numerical instabilities in free energy calculations based on molecular simulations. *Chem. Phys. Lett.*, 222(6), 1994.

[BPP+14] K. A. Black, D. Priftis, S. L. Perry, J. Yip, W. Y. Byun, and M. Tirrell. Protein Encapsulation via Polypeptide Complex Coacervation. *ACS Macro. Lett.*, 3(10), 2014.

[Bra13] C. P. Brangwynne. Phase transitions and size scaling of membraneless organelles. *J. Cell Biol.*, 203(6), 2013.

[Bro05] L. R. Brown. Commercial challenges of protein drug delivery. *Exp. Opin. Drug Delivery*, 2(1), 2005.

[BSHSK+17] S. Bazban-Shotorbani, M. M. Hasani-Sadrabadi, A. Karkhaneh, V. Serpooshan, K. Jacob, A. Moshaverinia, and M. Mahmoudi. Revisiting structure-property relationship of pH-responsive polymers for drug delivery applications. *J. Control. Release*, 253, 2017.

[BZL+11] O. V. Borisov, E. B. Zhulina, F. A. M. Leermakers, M. Ballauff, and A. H. E. Mueller. Conformations and Solution Properties of Star-Branched Polyelectrolytes. In *Self Organized Nanostructures Of Amphiphilic Block Copolymers I*, volume 241 of *Adv. Polym. Sci.* Springer Berlin Heidelberg, 2011.

[CBD+13] R. Chollakup, J. B. Beck, K. Dirnberger, M. Tirrell, and C. D. Eisenbach. Polyelectrolyte Molecular Weight and Salt Effects on the Phase Behavior and Coacervation of Aqueous Solutions of Poly(acrylic acid) Sodium Salt and Poly(allylamine) Hydrochloride. *Macromolecules*, 46(6), 2013.

[CD16] A. Chremos and J. F. Douglas. Influence of higher valent ions on flexible polyelectrolyte stiffness and counter-ion distribution. *J. Chem. Phys.*, 144(16), 2016.

[CJ01] M. Castelnovo and J.-F. Joanny. Complexation between oppositely charged polyelectrolytes: Beyond the Random Phase Approximation. *Eur. Phys. J. E*, 6(1), 2001.

[CLR+17] L. Chang, T. K. Lytle, M. Radhakrishna, J. J. Madinya, , J. Vélez, C. E. Sing, and S. L. Perry. Sequence and entropy-based control of complex coacervates. *Nat. Commun.*, 8(1273), 2017.

[CS11] F. Carnal and S. Stoll. Chain stiffness, salt valency, and concentration influences on titration curves of polyelectrolytes: Monte Carlo simulations. *J. Chem. Phys.*, 134(4), 2011.

[CSET10] R. Chollakup, W. Smitthipong, C. D. Eisenbach, and M. Tirrell. Phase Behavior and Coacervation of Aqueous Poly(acrylic acid)-Poly(allylamine) Solutions. *Macromolecules*, 43(5), 2010.

[CSHVdK05] M. A. Cohen Stuart, B. Hofs, I. K. Voets, and A. de Keizer. Assembly of polyelectrolyte-containing block copolymers in aqueous media. *Curr. Opin. Colloid Interface Sci.*, 10(1), 2005.

[CUS10] F. Carnal, S. Ulrich, and S. Stoll. Influence of explicit ions on titration curves and conformations of flexible polyelectrolytes: A Monte Carlo study. *Macromolecules*, 43(5), 2010.

[DBK+15] M. A. Dyakonova, A. V. Berezkin, K. Kyriakos, S. Gkermpoura, M. T. Popescu, S. K. Filippov, P. Štěpánek, Z. Di, C. Tsitsilianis, and C. M. Papadakis. Salt-Induced Changes in Triblock Polyampholyte Hydrogels: Computer Simulations and Rheological, Structural, and Dynamic Characterization. *Macromolecules*, 48(22), 2015.

[DDHS14] X. Du, P. L. Dubin, D. A. Hoagland, and L. Sun. Protein-Selective Coacervation with Hyaluronic Acid. *Biomacromolecules*, 15(3), 2014.

[DDKK11] D. Díaz Díaz, D. Kühbeck, and R. J. Koopmans. Stimuli-responsive gels as reaction vessels and reusable catalysts. *Chem. Soc. Rev.*, 40, 2011.

[DH98] M. Deserno and C. Holm. How to mesh up Ewald sums. I. A theoretical and numerical comparison of various particle mesh routines. *J. Chem. Phys.*, 109(18), 1998.

[DHM00] M. Deserno, C. Holm, and S. May. Fraction of Condensed Counterions around a Charged Rod: Comparison of Poisson-Boltzmann Theory and Computer Simulations. *Macromolecules*, 33, 2000.

[DKJR87] S. Duane, A. D. Kennedy, Pendleton B. J., and D. Roweth. Hybrid monte-carlo. *Phys. Lett. B*, 195(2), 1987.

[Dob08] A. V. Dobrynin. Theory and simulations of charged polymers: From solution properties to polymeric nanomaterials. *Curr. Opin. Colloid Interface Sci.*, 13(6), 2008.

[Don24] F. G. Donnan. The Theory of Membrane Equilibria. *Chem. Rev.*, 1(1), 1924.

[DR05] A. V. Dobrynin and M. Rubinstein. Theory of polyelectrolytes in solutions and at surfaces. *Prog. Polym. Sci.*, 30(11), 2005.

[DSP+14] M. A. Dyakonova, N. Stavrouli, M. T. Popescu, K. Kyriakos, I. Grillo, M. Philipp, S. Jaksch, C. Tsitsilianis, and C. M. Papadakis. Physical Hydrogels via Charge Driven Self-Organization of a Triblock Polyampholyte – Rheological and Structural Investigations. *Macromolecules*, 47(21), 2014.

[ELO+94] M. B. Ewing, T. H. Lilley, G. M. Olofsson, M. T. Ratzsch, and G. Somsen. Standard quantities in chemical thermodynamics. Fugacities, activities and equilibrium constants for pure and mixed phases (IUPAC Recommendations 1994). *Pure Appl. Chem.*, 66(3), 1994.

[Ewa21] P. P. Ewald. Die Berechnung optischer und elektrostatischer Gitterpotentiale. *Ann. Chim. Phys.*, 369(3), 1921.

[FA18] M. M. Fay and P. J. Anderson. The role of rna in biological phase separations. *J. Mol. Biol.*, 430(23), 2018.

[FAU+12] K. Fujii, H. Asai, T. Ueki, T. Sakai, S. Imaizumi, U. Chung, M. Watanabe, and M. Shibayama. High-performance ion gel with tetra-PEG network. *Soft Matter*, 8, 2012.

[FHSH15] F. Fahrenberger, O. A. Hickey, J. Smiatek, and C. Holm. Importance of Varying Permittivity on the Conductivity of Polyelectrolyte Solutions. *Phys. Rev. Lett.*, 115, 2015.

[FKL51] R. M. Fuoss, A. Katchalsky, and S. Lifson. The Potential of an Infinite Rod-Like Molecule and the Distribution of the Counter Ions. *Proc. Natl. Acad. Sci. U. S. A.*, 37, 1951.

[FOR] FOR2811: Adaptive Polymer Gels with Model-Network Structure. `https://www.for2811.uni-mainz.de`. Accessed: 2020-03-25.

[FR43] P. J. Flory and J. Rehner. Statistical Mechanics of Cross-Linked Polymer Networks II. Swelling. *J. Chem. Phys*, 11(11), 1943.

[FS02] D. Frenkel and B. Smit. *Understanding molecular simulations: from algorithms to applications*. Academic Press, 2002.

[FS16] J. Fu and J. B. Schlenoff. Driving Forces for Oppositely Charged Polyion Association in Aqueous Solutions: Enthalpic, Entropic, but Not Electrostatic. *J. Am. Chem. Soc.*, 138(3), 2016.

[FTTO14] Y. Fan, S. Tang, E. L. Thomas, and B. D. Olsen. Responsive Block Copolymer Photonics Triggered by Protein–Polyelectrolyte Coacervation. *ACS Nano*, 8(11), 2014.

[GK86] G. S. Grest and K. Kremer. Molecular dynamics simulation for polymers in the presence of a heat bath. *Phys. Rev. A*, 33, 1986.

[HE89] R. W. Hockney and J. W. Eastwood. *Computer Simulation Using Particles*. CRC Press, 1989.

[HFL+11] J. N. Hunt, K. E. Feldman, N. A. Lynd, J. Deek, L. M. Campos, J. M. Spruell, B. M. Hernandez, E. J. Kramer, and C. J. Hawker. Tunable, High Modulus Hydrogels Driven by Ionic Coacervation. *Adv. Mater.*, 23(20), 2011.

[HJK+04] C. Holm, J. F. Joanny, K. Kremer, R. R. Netz, P. Reineker, C. Seidel, T. A. Vilgis, and R. G. Winkler. Polyelectrolyte theory. In *Polyelectrolytes with defined molecular architecture II*, volume 166 of *Adv. Polym. Sci.* Springer, 2004.

[HKDL01] C. Holm, K. Kremer, M. Deserno, and H. J. Limbach. Computer Modeling of Charged Polymers. *NIC Symposium*, 9, 2001.

[HKW10] J. Höpfner, C. Klein, and M. Wilhelm. A Novel Approach for the Desalination of Seawater by Means of Reusable Poly(acrylic acid) Hydrogels and Mechanical Force. *Macromol. Rapid Commun.*, 31(15), 2010.

[HPL+15] K. Q. Hoffmann, S. L. Perry, L. Leon, D. Priftis, M. Tirrell, and J. J. de Pablo. A molecular view of the role of chirality in charge-driven polypeptide complexation. *Soft Matter*, 11, 2015.

[HTB01] F. Horkay, I. Tasaki, and P. J. Basser. Effect of Monovalent-Divalent Cation Exchange on the Swelling of Polyacrylate Hydrogels in Physiological Salt Solutions. *Biomacromolecules*, 2(1), 2001.

[IGPSS19] S. N. Innes-Gold, P. A. Pincus, M. J. Stevens, and O. A. Saleh. Polyelectrolyte Conformation Controlled by a Trivalent-Rich Ion Jacket. *Phys. Rev. Lett.*, 123, 2019.

[Irb94] A. Irbäck. Hybrid monte carlo simulation of polymer chains. *J. Chem. Phys.*, 101(2), 1994.

[IUP97] IUPAC. *Compendium of Chemical Terminology, 2nd ed. (the "Gold Book").* Blackwell Scientific Publications, 1997.

[JBB13] A. Jusufi, O. Borisov, and M. Ballauff. Structure formation in polyelectrolytes induced by multivalent ions. *Polymer*, 54(8), 2013.

[JBLK97] B. Jeong, Y. H. Bae, D. S. Lee, and S. W. Kim. Biodegradable block copolymers as injectable drug-delivery systems. *Nature*, 338(6645), 1997.

[JG10] J. Jagur-Grodzinski. Polymeric gels and hydrogels for biomedical and pharmaceutical applications. *Polym. Adv. Technol.*, 21(1), 2010.

[JK09] X. Jia and K. L. Kiick. Hybrid multicomponent hydrogels for tissue engineering. *Macromol. Biosci.*, 9(2), 2009.

[JL09] A. Jusufi and C. N. Likos. *Colloquium* : Star-branched polyelectrolytes: The physics of their conformations and interactions. *Rev. Mod. Phys*, 81, 2009.

[JPG94] J. K. Johnson, A. Z. Panagiotopoulos, and K. E. Gubbins. Reactive canonical Monte Carlo. *Mol. Phys.*, 81(3), 1994.

[KACD13] S. Kumar, R. Acharya, U. Chatterji, and P. De. Side-Chain Amino-Acid-Based pH-Responsive Self-Assembled Block Copolymers for Drug Delivery and Gene Transfer. *Langmuir*, 29(49), 2013.

[KG49] A. Katchalsky and J. Gillis. Theory of thr potentiometric titration of polymeric acids. *Recl. Trav. Chim. Pays-Bas*, 68(11), 1949.

[Kir35] J. G. Kirkwood. Statistical Mechanics of Fluid Mixtures. *J. Chem. Phys*, 3(300), 1935.

[KKK48] W. Kuhn, O. Kunzle, and A. Katchalsky. Verhalten Polyvalenter Fadenmolekelionen in Lösung. *Helv. Chim. Acta*, 31(7), 1948.

[KKRD19] M. Kanduč, W. K. Kim, R. Roa, and J. Dzubiella. Transfer Free Energies and Partitioning of Small Molecules in Collapsed PNIPAM Polymers. *J. Phys. Chem. B*, 123(3), 2019.

[KLC+13] D. V. Krogstad, N. A. Lynd, S.-H. Choi, J. M. Spruell, C. J. Hawker, E. J. Kramer, and M. V. Tirrell. Effects of Polymer and Salt Concentration on the Structure and Properties of Triblock Copolymer Coacervate Hydrogels. *Macromolecules*, 46(4), 2013.

[KM55] A. Katchalsky and I. Michaeli. Polyelectrolyte gels in salt solutions. *J. Polym. Sci.*, 15(79), 1955.

[KRH15] P. Košovan, T. Richter, and C. Holm. Modeling of Polyelectrolyte Gels in Equilibrium with Salt Solutions. *Macromolecules*, 48(20), 2015.

[KS47] A. Katchalsky and P. Spitnik. Potentiometric titrations of polymethacrylic acid. *J. Polym. Sci.*, 2(4), 1947.

[KWLF+99] J. Klein Wolterink, F. A. M. Leermakers, G. J. Fleer, L. K. Koopal, E. B. Zhulina, and O. V. Borisov. Screening in Solutions of Star-Branched Polyelectrolytes. *Macromolecules*, 32(7), 1999.

[Lan20] J. Landsgesell. Simulation and Modeling of Polyelectrolyte Gels, 2020. Institute for Computational Physics, University of Stuttgart, Dissertation thesis.

[LAO12] A. Levy, D. Andelman, and H. Orland. Dielectric Constant of Ionic Solutions: A Field-Theory Approach. *Phys. Rev. Lett.*, 108, 2012.

[LC16] S. Lindhoud and M. M. A. E. Claessens. Accumulation of small protein molecules in a macroscopic complex coacervate. *Soft Matter*, 12, 2016.

[LCM+19] T. K. Lytle, L.-W. Chang, N. Markiewicz, S. L. Perry, and C. E. Sing. Designing Electrostatic Interactions via Polyelectrolyte Monomer Sequence. *ACS Cent. Sci.*, 5(4), 2019.

[LdVS+09] S. Lindhoud, R. de Vries, R. Schweins, M. A. Cohen Stuart, and W. Norde. Salt-induced release of lipase from polyelectrolyte complex micelles. *Soft Matter*, 5, 2009.

[Lea01] A. R. Leach. *Molecular modelling principles and applications.* Pearson, 2001.

[LHR+20] J. Landsgesell, P. Hebbeker, O. Rud, R. Lunkad, P. Košovan, and C. Holm. Grand-Reaction Method for Simulations of Ionization Equilibria Coupled to Ion Partitioning. *Macromolecules*, 53(8), 2020.

[LHS17] J. Landsgesell, C. Holm, and J. Smiatek. Simulation of weak polyelectrolytes: a comparison between the constant pH and the reaction ensemble method. *Eur. Phys. J. Spec. Top.*, 226(4), 2017.

[LMH+] R. Lunkad, A. Murmiliuk, P. Hebbeker, M. Boublík, Z. Tošner, M. Štěpánek, and P. Košovan. Quantitative prediction of charge regulation in oligopeptides. In preparation.

[LNR+19] J. Landsgesell, L. Nová, O. Rud, F. Uhlík, D. Sean, P. Hebbeker, C. Holm, and P. Košovan. Simulations of ionization equilibria in weak polyelectrolyte solutions and gels. *Soft Matter*, 15(6), 2019.

[LOdlCS11] G. S. Longo, M Olvera de la Cruz, and I. Szleifer. Molecular Theory of Weak Polyelectrolyte Gels: The Role of pH and Salt Concentration. *Macromolecules*, 44(1), 2011.

[LRS16] T. K. Lytle, M. Radhakrishna, and C. E. Sing. High Charge Density Coacervate Assembly via Hybrid Monte Carlo Single Chain in Mean Field Theory. *Macromolecules*, 49(24), 2016.

[LS17] T. K. Lytle and C. E. Sing. Transfer matrix theory of polymer complex coacervation. *Soft Matter*, 13, 2017.

[LSA+18] L. Li, S. Srivastava, M. Andreev, A. B. Marciel, J. J. de Pablo, and M. V. Tirrell. Phase Behavior and Salt Partitioning in Polyelectrolyte Complex Coacervates. *Macromolecules*, 51(8), 2018.

[LSK+19] J. Landsgesell, D. Sean, P. Kreissl, K. Szuttor, and C. Holm. Modeling Gel Swelling Equilibrium in the Mean Field: From Explicit to Poisson-Boltzmann Models. *Phys. Rev. Lett.*, 122, 2019.

[LSV+10] M. Lemmers, J. Sprakel, I. K. Voets, J. van der Gucht, and M. A. Cohen Stuart. Multiresponsive Reversible Gels Based on Charge-Driven Assembly. *Angew. Chem.*, 49(4), 2010.

[Lyt19] T. K. Lytle. The effect of physical molecular features on complex coacervation phase separation, 2019. University of Illinois at Urbana-Champaign, Dissertation thesis.

[Man69] G. S. Manning. Limiting Laws and Counterion Condensation in Polyelectrolyte Solutions I. Colligative Properties. *J. Chem. Phys.*, 51(3), 1969.

[Man08] J. F. Mano. Stimuli-Responsive Polymeric Systems for Biomedical Applications. *Adv. Eng. Mater.*, 10(6), 2008.

[McQ73] D. A. McQuarrie. *Statistical Mechanics*. Harper & Row, 1973.

[Mez89] M. Mezei. Direct Calculation of the Excess Free Energy of the Dense Lennard-Jones Fluid. *Mol. Simulat.*, 2, 1989.

[MHBJ08] Y. Mei, M. Hoffmann, M. Ballauff, and A. Jusufi. Spherical polyelectrolyte brushes in the presence of multivalent counterions: The effect of fluctuations and correlations as determined by molecular dynamics simulations. *Phys. Rev. E*, 77(3), 2008.

[MHK05] B. A. Mann, C. Holm, and K. Kremer. Swelling of polyelectrolyte networks. *J. Chem. Phys*, 122(15), 2005.

[MKH06] B. A. Mann, K. Kremer, and C. Holm. The Swelling Behavior of Charged Hydrogels. *Macromol. Symp.*, 237(1), 2006.

[MKJ+18] A. Murmiliuk, P. Košovan, M. Janata, K. Procházka, F. Uhlík, and M. Štěpánek. Local pH and Effective pK of a Polyelectrolyte Chain: Two Names for One Quantity? *ACS Macro Lett.*, 7(10), 2018.

[MKK+20] J. B. Max, K. Kowalczuk, M. Köhler, C. Neumann, F. Pielenz, L. V. Sigolaeva, D. V. Pergushov, A. Turchanin, F. Langenhorst, and F. H. Schacher. Polyampholytic Poly(dehydroalanine) Graft Copolymers as Smart Templates for pH-Controlled Formation of Alloy Nanoparticles. *Macromolecules*, 53(11), 2020.

[MLH+06] Y. Mei, K. Lauterbach, M. Hoffmann, O. V. Borisov, M. Ballauff, and A. Jusufi. Collapse of spherical polyelectrolyte brushes in the presence of multivalent counterions. *Phys. Rev. Lett.*, 97(15), 2006.

[MMTS20] J. B. Max, P. J. Mons, J. C. Tom, and F. H. Schacher. Double Hydrophilic Poly(ethylene oxide)-block-Poly(dehydroalanine) Block Copolymers: Comparison of Two Different Synthetic Routes. *Macromol. Chem. Phys*, 221(1), 2020.

[MNW15] A. Melnyk, J. Namieśnik, and L. Wolska. Theory and recent applications of coacervate-based extraction techniques. *Trends Analyt. Chem.*, 71, 2015.

[MOV57] I. Michaeli, J. Th. G. Overbeek, and M. J. Voorn. Phase separation of polyelectrolyte solutions. *J. Polym. Sci.*, 23(103), 1957.

[MRR+53] N. Metropolis, A. W. Rosenbluth, M. N. Rosenbluth, A. H. Teller, and E. Teller. Equation of State Calculations by Fast Computing Machines. *The Journal of Chemical Physics*, 21(6), 1953.

[Mun92] P. Munk. *Introduction to Macromolecular Science*. John Wiley & Sons, Ltd, 1992.

[Mut17] M. Muthukumar. 50th Anniversary Perspective: A Perspective on Polyelectrolyte Solutions. *Macromolecules*, 50(24), 2017.

[NBP+02] A. P. Nowak, V. Breedveld, L. Pakstis, B. Ozbas, D. J. Pine, D. Pochan, and T. J. Deming. Rapidly recovering hydrogel scaffolds from self-assembling diblock copolypeptide amphiphiles. *Nature*, 417(6887), 2002.

[NKFP13] A. Naji, M. Kanduč, J. Forsman, and R. Podgornik. Perspective: Coulomb fluids—Weak coupling, strong coupling, in between and beyond. *J. Chem. Phys.*, 139(15), 2013.

[NKK02] I. Nezbeda, J. Kolafa, and M. Kotrla. *Úvod do molekulárních simulací: metody Monte Carlo a molekulární dynamiky*. Karolinum, 2002.

[NMV+09] A. E. Nel, L. Mädler, D. Velegol, T. Xia, E M. V. Hoek, P. Somasundaran, F. Klaessig, V. Castranova, and M. Thompson. Understanding biophysicochemical interactions at the nano–bio interface. *Nat. Mater.*, 8(7), 2009.

[NN06] A. Naji and R. R. Netz. Scaling and universality in the counterion-condensation transition at charged cylinders. *Phys. Rev. E*, 73(5), 2006.

[NPS18] R. J. Nap, S. H. Park, and I. Szleifer. Competitive calcium ion binding to end-tethered weak polyelectrolytes. *Soft Matter*, 14(12), 2018.

[NUK17] L. Nová, F. Uhlík, and P. Košovan. Local pH and effective pK_A of weak polyelectrolytes – insights from computer simulations. *Phys. Chem. Chem. Phys.*, 19(22), 2017.

[NXKD20] R. Nikam, X. Xu, M. Kanduč, and J. Dzubiella. Competitive sorption of monovalent and divalent ions by highly charged globular macromolecules. *J. Chem. Phys.*, 153(4), 2020.

[OdlCBD+95] M. Olvera de la Cruz, L. Belloni, M. Delsanti, J. P. Dalbiez, O. Spalla, and M. Drifford. Precipitation of highly charged polyelectrolyte solutions in the presence of multivalent salts. *J. Chem. Phys.*, 103(13), 1995.

[OFMM14] K. Oshima, T. Fujimoto, E. Minami, and Y. Mitsukami. Model Polyelectrolyte Gels Synthesized by End-Linking of Tetra-Arm Polymers with Click Chemistry: Synthesis and Mechanical Properties. *Macromolecules*, 47(21), 2014.

[OKP03] G. Orkoulas, S. K. Kumar, and A. Z. Panagiotopoulos. Monte Carlo Study of Coulombic Criticality in Polyelectrolytes. *Phys. Rev. Lett.*, 90, 2003.

[OM06] Z. Ou and M. Muthukumar. Entropy and enthalpy of polyelectrolyte complexation: Langevin dynamics simulations. *J. Chem. Phys.*, 124(15), 2006.

[OMGG16] K. Opwis, T. Mayer-Gall, and J. S. Gutmann. Recovery of Noble Metals by the Use of Functional Adsorber Textiles. *Tekstil*, 65, 2016.

[Oos57] F. Oosawa. A simple theory of thermodynamic properties of polyelectrolyte solutions. *J. Polym. Sci.*, 23(103), 1957.

[OV57] J. T. G. Overbeek and M. J. Voorn. Phase separation in polyelectrolyte solutions. Theory of complex coacervation. *J. Cell. Physiol.*, 49(S1), 1957.

[Pan09] A. Z. Panagiotopoulos. Charge correlation effects on ionization of weak polyelectrolytes. *J. Phys. Condens. Matter*, 21(42), 2009.

[Pat20] C. S. Patrickios. Thirty Years of Amphiphilic Polymer Conetworks. In *Amphiphilic Polymer Co-networks: Synthesis, Properties, Modelling and Applications*. The Royal Society of Chemistry, 2020.

[PBL+05] F. A. Plamper, H. Becker, M. Lanzendorfer, M. Patel, A. Wittemann, M. Ballauff, and A. H. E. Müller. Synthesis, characterization and behavior in aqueous solution of star-shaped poly(acrylic acid). *Macromol. Chem. Phys.*, 206(18), 2005.

[PD04] C. S. Peyratout and L. Dahne. Tailor-made polyelectrolyte microcapsules: From multilayers to smart containers. *Angew. Chem.*, 43(29), 2004.

[PG03] C. S. Patrickios and T. K. Georgiou. Covalent amphiphilic polymer networks. *Curr. Opin. Colloid Interface Sci.*, 8(1), 2003.

[PLH+15] S. L. Perry, L. Leon, K. Q. Hoffmann, M. J. Kade, D. Priftis, K. A. Black, D. Wong, R. A. Klein, C. F. Pierce, K. O. Margossian, J. K. Whitmer, J. Qin, J. J. de Pablo, and M. Tirrell. Chirality-selected phase behaviour in ionic polypeptide complexes. *Nat. Commun.*, 6(1), 2015.

[PLP+14] S. L. Perry, Y. Li, D. Priftis, L. Leon, and M. Tirrell. The Effect of Salt on the Complex Coacervation of Vinyl Polyelectrolytes. *Polymers*, 6(6), 2014.

[PLW+16] Y. Pan, Z. Liu, W. Wang, C. Peng, K. Shi, and X. Ji. Highly efficient macroporous adsorbents for toxic metal ions in water systems based on polyvinyl alcohol–formaldehyde sponges. *J. Mater. Chem. A*, 4(7), 2016.

[Pou08] J. Pouchlý. *Fyzikální chemie makromolekulárních a koloidních soustav*. Vysoká škola chemicko-technologická v Praze, 2008.

[PS15] S. L. Perry and C. E. Sing. PRISM-Based Theory of Complex Coacervation: Excluded Volume versus Chain Correlation. *Macromolecules*, 48(14), 2015.

[PS20] S. L. Perry and C. E. Sing. 100th Anniversary of Macromolecular Science Viewpoint: Opportunities in the Physics of Sequence-Defined Polymers. *ACS Macro. Lett.*, 9(2), 2020.

[PT12] D. Priftis and M. Tirrell. Phase behaviour and complex coacervation of aqueous polypeptide solutions. *Soft Matter*, 8, 2012.

[PWMB07] F. A. Plamper, A. Walther, A. H. E. Müller, and M. Ballauff. Nanoblossoms: Light-induced conformational changes of cationic polyelectrolyte stars in the presence of multivalent counterions. *Nano Lett.*, 7(1), 2007.

[QJWZ17] C. Qu, B. Jing, S. Wang, and Y. Zhu. Distinct Effects of Multivalent Macroion and Simple Ion on the Structure and Local Electric Environment of a Weak Polyelectrolyte in Aqueous Solution. *J. Phys. Chem. B*, 121(37), 2017.

[QP01] Y. Qiu and K. Park. Environment-sensitive hydrogels for drug delivery. *Adv. Drug Deliv. Rev.*, 53(3), 2001.

[RBL+17] M. Radhakrishna, K. Basu, Y. Liu, R. Shamsi, S. L. Perry, and C. E. Sing. Molecular Connectivity and Correlation Effects on Polymer Coacervation. *Macromolecules*, 50(7), 2017.

[RC03] M. Rubinstein and R. H. Colby. *Polymer Physics*. Oxford University Press, 2003.

[RdCL00] E. Raspaud, M. da Conceiçao, and F. Livolant. Do Free DNA Counterions Control the Osmotic Pressure? *Phys. Rev. Lett.*, 84, 2000.

[RR92] C. E. Reed and W. F. Reed. Monte Carlo study of titration of linear polyelectrolytes. *J. Chem. Phys*, 96(2), 1992.

[RRB+17] O. Rud, T. Richter, O. Borisov, C. Holm, and P. Košovan. A self-consistent mean-field model for polyelectrolyte gels. *Soft Matter*, 13, 2017.

[RSSW17] V. S. Rathee, H. Sidky, B. J. Sikora, and J. K. Whitmer. Explicit Ion Effects on the Charge and Conformation of Weak Polyelectrolytes. *Polymers*, 11(1), 2017.

[RSSW18] V. S. Rathee, H. Sidky, B. J. Sikora, and J. K. Whitmer. Role of Associative Charging in the Entropy–Energy Balance of Polyelectrolyte Complexes. *J. Am. Chem. Soc.*, 140(45), 2018.

[RZS+18] V. S. Rathee, A. J. Zervoudakis, H. Sidky, B. J. Sikora, and J. K. Whitmer. Weak polyelectrolyte complexation driven by associative charging. *J. Chem. Phys.*, 148(11), 2018.

[SAL+17] S. Srivastava, M. Andreev, A. E. Levi, D. J. Goldfeld, J. Mao, W. T. Heller, V. M. Prabhu, J. J. de Pablo, and M. V. Tirrell. Gel phase formation in dilute triblock copolyelectrolyte complexes. *Nat. Commun.*, 8(1), 2017.

[SGKOdlC20] A. Shakya, M. Girard, J. T. King, and M. Olvera de la Cruz. Role of Chain Flexibility in Asymmetric Polyelectrolyte Complexation in Salt Solutions. *Macromolecules*, 53(4), 2020.

[Sin17] C. E. Sing. Development of the modern theory of polymeric complex coacervation. *Adv. Colloid Interface Sci.*, 239, 2017.

[SLS19] M. Shibayama, X. Li, and T. Sakai. Precision polymer network science with tetra-PEG gels—a decade history and future. *Colloid Polym. Sci.*, 297(1), 2019.

[SMC07] T. Steinbrecher, D. L. Mobley, and D. A. Case. Nonlinear scaling schemes for Lennard-Jones interactions in free energy calculations. *J. Chem. Phys*, 127(21), 2007.

[Smi20] J. Smiatek. Theoretical and Computational Insight into Solvent and Specific Ion Effects for Polyelectrolytes: The Importance of Local Molecular Interactions. *Molecules*, 25(7), 2020.

[SMVV17] V. Schubertová, F. J. Martinez-Veracoechea, and R. Vácha. Design of Multivalent Inhibitors for Preventing Cellular Uptake. *Sci. Rep.*, 7(11689), 2017.

[SMY+08] T. Sakai, T. Matsunaga, Y. Yamamoto, C. Ito, R. Yoshida, S. Suzuki, N. Sasaki, M. Shibayama, and U. Chung. Design and Fabrication of a High-Strength Hydrogel with Ideally Homogeneous Network Structure from Tetrahedron-like Macromonomers. *Macromolecules*, 41(14), 2008.

[SNUK20] R. Staňo, L. Nová, F. Uhlík, and P. Košovan. Multivalent counterions accumulate in star-like polyelectrolytes and collapse the polymer in spite of increasing its ionization. *Soft Matter*, 16(4), 2020.

[SOdlC00] F. J. Solis and M. Olvera de la Cruz. Collapse of flexible polyelectrolytes in multivalent salt solutions. *J. Chem. Phys.*, 112(4), 2000.

[SP20] C. E. Sing and S. L. Perry. Recent progress in the science of complex coacervation. *Soft Matter*, 16, 2020.

[SS89] M. Sastre and J. A. Santaballa. A note on the meaning of the electroneutrality condition for solutions. *J. Chem. Educ.*, 66(5), 1989.

[ST94] W. R. Smith and B. Tříska. The reaction ensemble method for the computer simulation of chemical and phase equilibria. I. Theory and basic examples. *J. Chem. Phys.*, 100(4), 1994.

[ST11] C. Schmitt and S. L. Turgeon. Protein/polysaccharide complexes and coacervates in food systems. *Adv. Colloid Interface Sci.*, 167(1873), 2011.

[Sta18] R. Staňo. Interakce slabých polyelektrolytů s multivalentními ionty., 2018. Faculty of Science, Charles University, Bachelor's thesis.

[Str07] G. Strobl. *The Physics of Polymers: Concepts for Understanding Their Structures and Behavior*. Springer, 2007.

[STUC20] C. Sun, T. Tang, H. Uludag, and J. E. Cuervo. Molecular dynamics simulations of dna/pei complexes: Effect of pei branching and protonation state. *Biophys. J.*, 100, 2020.

[SWB+10] E. Spruijt, A. H. Westphal, J. W. Borst, M. A. Cohen Stuart, and J. van der Gucht. Binodal Compositions of Polyelectrolyte Complexes. *Macromolecules*, 43(15), 2010.

[SYDW19] J. B. Schlenoff, M. Yang, Z. A. Digby, and Q. Wang. Ion Content of Polyelectrolyte Complex Coacervates and the Donnan Equilibrium. *Macromolecules*, 52(23), 2019.

[TBL+08] C. Turner, J. K. Brennan, M. Lísal, W. R. Smith, J. K. Johnson, and K. E. Gubbins. Simulation of chemical reaction equilibria by the reaction ensemble Monte Carlo method: a review. *Mol. Simul.*, 34(2), 2008.

[TIM20] A. Tagliabue, L. Izzo, and M. Mella. Interface Counterion Localization Induces a Switch between Tight and Loose Configurations of Knotted Weak Polyacid Rings despite Intermonomer Coulomb Repulsions. *J. Phys. Chem. B*, 124(14), 2020.

[TLMH] A. Tagliabue, J. Landsgesell, M. Mella, and C. Holm. Oppositely charged star polyelectrolytes: do they cross-link forming gels? In preparation.

[Tru68] A. H. Truesdell. Activity Coefficients of Aqueous Sodium Chloride from 15 °C to 50 °C Measured with a Glass Electrode. *Science*, 161, 1968.

[TS12] M. Tagliazucchi and I. Szleifer. Stimuli-responsive polymers grafted to nanopores and other nano-curved surfaces: structure, chemical equilibrium and transport. *Soft Matter*, 8, 2012.

[Tuc10] M. E. Tuckerman. *Statistical Mechanics: Theory and Molecular Simulation*. Oxford University Press, 2010.

[UKL+14] F. Uhlík, P. Košovan, Z. Limpouchová, K. Procházka, O. V. Borisov, and F. A. M. Leermakers. Modeling of ionization and conformations of starlike weak polyelectrolytes. *Macromolecules*, 47(12), 2014.

[UKZB16] F. Uhlík, P. Košovan, E. B. Zhulina, and O. V. Borisov. Charge-controlled nano-structuring in partially collapsed star-shaped macromolecules. *Soft Matter*, 12(21), 2016.

[VBvSH06] T. Vermonden, N. A. M. Besseling, M. J. van Steenbergen, and W. E. Hennink. Rheological Studies of Thermosensitive Triblock Copolymer Hydrogels. *Langmuir*, 22(24), 2006.

[vdGSLCS11] J. van der Gucht, E. Spruijt, M. Lemmers, and M. A. Cohen Stuart. Polyelectrolyte complexes: Bulk phases and colloidal systems. *J. Colloid Interface Sci.*, 361(2), 2011.

[VdKCS09] I. K. Voets, A. de Keizer, and M. A. Cohen Stuart. Complex coacervate core micelles. *Adv. Colloid Interface Sci.*, 147-148(300), 2009.

[vdM08] J. R. C. van der Maarel. *Introduction to Biopolymer Physics*. World Scientific Publishing Company, 2008.

[VH16] L. Voorhaar and R. Hoogenboom. Supramolecular polymer networks: hydrogels and bulk materials. *Chem. Soc. Rev.*, 45, 2016.

[VJFZ19] B. Valley, B. Jing, M. Ferreira, and Y. Zhu. Rapid and Efficient Coacervate Extraction of Cathionic Industrial Dyes from Wastewater. *ACS Appl. Mater. Interfaces*, 11(7), 2019.

[vLCL19] J. van Lente, M. M. A. E. Claessens, and S. Lindhoud. Charge-Based Separation of Proteins Using Polyelectrolyte Complexes as Models for Membraneless Organelles. *Biomacromolecules*, 20(10), 2019.

[Voh86] J. Vohlídal. *Makromolekulární chemie*. Státní pedagogické nakladatelství, 1986.

[Was10] T. Wasilewski. Coacervates as a Modern Delivery System of Hand Dishwashing Liquids. *J. Surfactants Deterg.*, 13(4), 2010.

[Wid63] B. Widom. Some Topics in the Theory of Fluids. *J. Chem. Phys*, 39(11), 1963.

[WJD+19] A. V. Walter, L. N. Jimenez, J. Dinic, V. Sharma, and K. A. Erk. Effect of salt valency and concentration on shear and extensional rheology of aqueous polyelectrolyte solutions for enhanced oil recovery. *Rheol. Acta*, 58(3-4), 2019.

[WMY+10] Q. Wang, J. L. Mynar, M. Yoshida, E. Lee, M. Lee, K. Okuro, K. Kinbara, and T. Aida. High-water-content mouldable hydrogels by mixing clay and a dendritic molecular binder. *Nature*, 463(7279), 2010.

[WRHDF20] X. Wang, S. Ramírez-Hinestrosa, J. Dobnikar, and D. Frenkel. The Lennard-Jones potential: when (not) to use it. *Phys. Chem. Chem. Phys.*, 22, 2020.

[WS14] Q. Wang and J. B. Schlenoff. The Polyelectrolyte Complex/Coacervate Continuum. *Macromolecules*, 47(9), 2014.

[WWS+19] F. Weik, R. Weeber, K. Szuttor, K. Breitsprecher, J. de Graaf, M. Kuron, J. Landsgesell, H. Menke, D. Sean, and C. Holm. ESPResSo 4.0 – an extensible software package for simulating soft matter systems. *Eur. Phys. J. Spec. Top.*, 227(1789), 2019.

[YDF+14] H. Yoon, E. J. Dell, J. L. Freyer, L. M. Campos, and W.-D. Jang. Polymeric supramolecular assemblies based on multivalent ionic interactions for biomedical applications. *Polymer*, 55(2), 2014.

[YHDdP08] D.-W. Yin, F. Horkay, J. F. Douglas, and J. J. de Pablo. Molecular simulation of the swelling of polyelectrolyte gels by monovalent and divalent counterions. *J. Chem. Phys*, 129(15), 2008.

[YJX+18] J. Yu, N. E. Jackson, X. Xu, Y. Morgenstern, Y. Kaufman, M. Ruths, J. J. de Pablo, and M. Tirrell. Multivalent counterions diminish the lubricity of polyelectrolyte brushes. *Science*, 360(6396), 2018.

[YMY+16] J. Yu, J. Mao, G. Yuan, S. Satija, Z. Jiang, W. Chen, and M. Tirrell. Structure of Polyelectrolyte Brushes in the Presence of Multivalent Counterions. *Macromolecules*, 49(15), 2016.

[ZAWW18] P. Zhang, N. M. Alsaifi, J. Wu, and Z.-G. Wang. Polyelectrolyte complex coacervation: Effects of concentration asymmetry. *J. Chem. Phys.*, 149(16), 2018.

[ZSAW18] P. Zhang, K. Shen, N. M. Alsaifi, and Z. G. Wang. Salt Partitioning in Complex Coacervation of Symmetric Polyelectrolytes. *Macromolecules*, 51(15), 2018.

[ZW10a] J. Ziebarth and Y. Wang. Coarse-Grained Molecular Dynamics Simulations of DNA Condensation by Block Copolymer and Formation of Core - Corona Structures. *J. Phys. Chem. B*, 114(19), 2010.

[ZW10b] J. D. Ziebarth and Y. Wang. Understanding the protonation behavior of linear polyethylenimine in solutions through Monte Carlo simulations. *Biomacromolecules*, 11(1), 2010.

[ZZ18] M. Zhao and N. S. Zacharia. Protein encapsulation via polyelectrolyte complex coacervation: Protection against protein denaturation. *J. Chem. Phys*, 149(16), 2018.